University of Nevada, Reno

Contributions to the Neotectonics of the central and northern Walker Lane

A Dissertation submitted in partial fulfillment of the requirements for the degree of Doctor of Philosophy in Geology

by

Stephen J Angster

Dr. Steven G. Wesnousky/Dissertation Advisor

May, 2018

THE GRADUATE SCHOOL

We recommend that the dissertation
prepared under our supervision by

STEPHEN ANGSTER

Entitled

Contributions To The Neotectonics Of The Central And Northern Walker Lane

be accepted in partial fulfillment of the
requirements for the degree of

DOCTOR OF PHILOSOPHY

Dr. Steven G. Wesnousky, Advisor

Dr. Keneth Adams, Committee Member

Dr. William Hammond, Committee Member

Dr. Graham Kent, Committee Member

Dr. Raj Siddarthan, Graduate School Representative

David W. Zeh, Ph. D., Dean, Graduate School
May, 2018

ABSTRACT

The Walker Lane is a well-known intraplate shear zone located east of the Sierra Nevada that accommodates a significant portion of the North American – Pacific Plate relative transform motion. It its defined by a broad zone of discontinuous active strike-slip and normal faulting that sit within a zone geodetically characterized by transtensional dextral shear. Strain in the Walker Lane is driven by the northwest translation of the Sierra Nevada and long-term geologic constraints on the distribution and partitioning of slip amongst the active faults are limited, thus our understanding of how these faults interact and behave as a system remains understudied. These limitations are consequences of the slow-slip rate environments, making geomorphic preservation and observation of offset more difficult. Similarly, at the northern end of the Sierra Nevada, regional north-south oriented contraction is geodetically observed and has been attributed to the interaction of the northwest translating Sierra Nevada with the overriding plate of the southern Cascadia Subduction Zone. Accommodation of this strain remains geologically unaccounted for, thus it is unknown how the contraction is accommodated. The purpose of this dissertation is to place new and more robust constraints on the rates of slip for multiple Walker Lane faults and to identify and characterize potentially active faults within the northern Sierra and southern Cascadia transition zone. Much of this work is motivated by seismic hazard, but scientifically serves to provide a better understanding of how strain is released bordering the Sierra Nevada Mountains.

This dissertation consists of 3 chapters. The first study explores a new application of a ground surface modeling technique for the purpose of placing better constraints on the rate of slip for the Pyramid Lake fault, a major strike-slip fault in the northern portion of the Walker Lane. This study is herein presented as published in the *Bulletin of the Seismological Society of America* (Vol. 106, No. 2, 2016). Chapter 2 builds on this method and incorporates multiple Quaternary dating techniques that place constraints on horizontal slip-rates in a network of strike-slip faults that comprise the central Walker Lane. The observations and new rates obtained in this study provide insight into how slip is accommodated on a variety of spatiotemporal scales. Finally, chapter 3 presents the results from a combination of geophysical, geologic, and geomorphic observations made within the northern Sacramento Valley that show the presence of Quaternary contractional deformation associated with a series of previously identified structures optimally oriented to accommodate north-south contraction. These findings show for the first time, how geodetically observed strain is accommodated within the northern Sierra and southern Cascadia transition zone.

DEDICATION

I dedicate this work to wife and life partner, Jade.

Thank you so much for loving me and always providing a sense of stability, support, and never-ending outlets of adventurous escapes that allowed me to refocus and enjoy the best parts of life.

ACKNOWLEDGEMENTS

There are many who deserve my thanks for providing support and encouragement during these past 5 years. I will undoubtedly fall short of naming everyone who has contributed to these studies or has had an impact on my development as a PhD student, and for that I give a heartfelt thanks to everyone who I have shared time with.

First and foremost, it has been a pleasure to work under the guidance of my advisor, Steven Wesnousky. I am forever grateful for the opportunities and freedoms he provided that allowed me to pursue and build on his ideas as well as those of my own. Steve creates an environment that allows science to progress and education to flourish. There is never a question on whether something needs to be visited in the field, “go” is the advice he’ll provide. I am truly grateful for the funding and guidance you shared these past 5 years. I also thank the rest of my committee, Ken Adams, Bill Hammond, Graham Kent, and Raj Siddarthan for their help and encouragement through this process.

Visiting students, Wei-liang Huang and Xinnan Li, provided amazing companionship and support in the field. Wei-liang was vital to developing methodologies in the field for drone photography. I’ve had countless intriguing and ‘arm waving’ discussions with my lab mates Ian Pierce, Tabor Reedy, and Rachel Hatch who have no doubt helped with the thought process and sparked ideas for these studies. Additional conversations with Jayne Bormann, Pat

Cashman, Jim Trexler, and Chad Carlson have also significantly help with my understanding of the Walker Lane. I also need to thank Tom Sawyer who came up with the original idea for the faults and folds in the northern Sacramento Valley. Tom introduced me to the field area and enabled a fruitful kayak trip down the Sacramento River that led to the collection of several radiocarbon samples used in the study. Thank you to my coauthors and friends at the University of Cincinnati where I spent several months invading and processing sediment in the cosmogenic laboratories. In particular, thank you Lewis Owen and Paula Figueiredo for your hard work and guidance on these studies.

Financial support was generously provide by the Center for Neotectonic Studies, Seismologic Laboratory of Nevada, the Department of Geological Sciences, a GSA Graduate Student Research Grant, and a grant from the California Federation of Mineralogical Societies.

Thank you to my parents, Susan and John, who have always encouraged me to follow my passion. Thanks to my wonderful sisters who also provided much needed encouragement at times and understanding of my sometimes brotherly absence these past five years.

TABLE OF CONTENTS

LIST OF TABLES

LIST OF FIGURES

CHAPTER 1

CHAPTER 2

CHAPTER 3

CHAPTER 1

Application of UAV Photography to Refining the Slip Rate on the Pyramid Lake Fault Zone, Nevada

Stephen Angster, Steven Wesnousky, Wei-liang Huang, Graham Kent, Takashi Nakata, and Hideaki Goto

Abstract

The Pyramid Lake fault zone is a 50 km-long, active northwest trending right-lateral fault in the northern Walker Lane, located ~30 km east of Reno, NV. Previous paleoearthquake and slip rate studies report that the Pyramid Lake fault has produced four surface rupturing paleoearthquakes since 15,475 ± 720 cal. yr B.P., three of which occurred after 8,980 ± 260 cal yr B.P., and has an average minimum slip rate of 2.6 ± 0.3 mm/yr since the late Pleistocene. These observations imply that coseismic offset for each paleoearthquake averaged 7 – 9 m, larger than expected from empirical scaling relationships for a strike-slip fault of its length. To reconcile this discrepancy, we used a small camera-mounted UAV to develop high-resolution digital elevation models and interpret previously unreported right-laterally offset geomorphic features along the northern section of the Pyramid Lake fault zone. Offset measurements at seven sites range from 8 – 21 meters. The ages of displaced features are interpreted from previous lake level and mapping studies of Lake Lahontan. From these observations, slip rate estimates at the sites range between 0.5 – 1.6 mm/yr. These lower values of slip rate require that coseismic displacements associated with previously reported paleoearthquakes average only 3 – 5 meters, within the range that would be predicted from empirical scaling relationships of rupture length and coseismic displacement.

Introduction

High-density geospatial point datasets provide opportunities to observe, measure, and document geologic surface processes at higher resolution than alternative approaches, particularly in subtle or obscured landscapes that pose interpretive challenges in the field (Arrowsmith and Zielke, 2009; Gold et al., 2013; Johnson et al., 2014; Zielke et al., 2015). The recent and rapid advancement in acquisition techniques provides quick, accurate, and very cost effective methods for scientists to utilize high-resolution digital elevation data for geologic analysis (Bemis et al., 2014; Johnson et al. 2014). These advances provide the opportunity to reevaluate prior studies where inconsistencies or controversies persist.

The Pyramid Lake fault zone (PLFZ) is a 50 km-long, active northwest trending right-lateral fault in the northern Walker Lane (Figure 1). Previous paleoearthquake and slip rate studies indicate that the Pyramid Lake fault has produced four surface-rupturing paleoearthquakes since 15,475 ± 720 cal. yr B.P., three of which occurred after 8,980 ± 260 cal yr B.P., and has an average minimum slip rate of 2.6 ± 0.3 mm/yr since the late Pleistocene (Anderson and Hawkins, 1984; Briggs and Wesnousky, 2004). Reconciling these observations with expected per-event displacements for a fault of its length is challenging. Specifically, coseismic offsets of 7 – 9 m during the latest three paleoearthquakes are required to satisfy the fault slip rate, significantly larger than would generally be expected from empirical scaling relationships for a

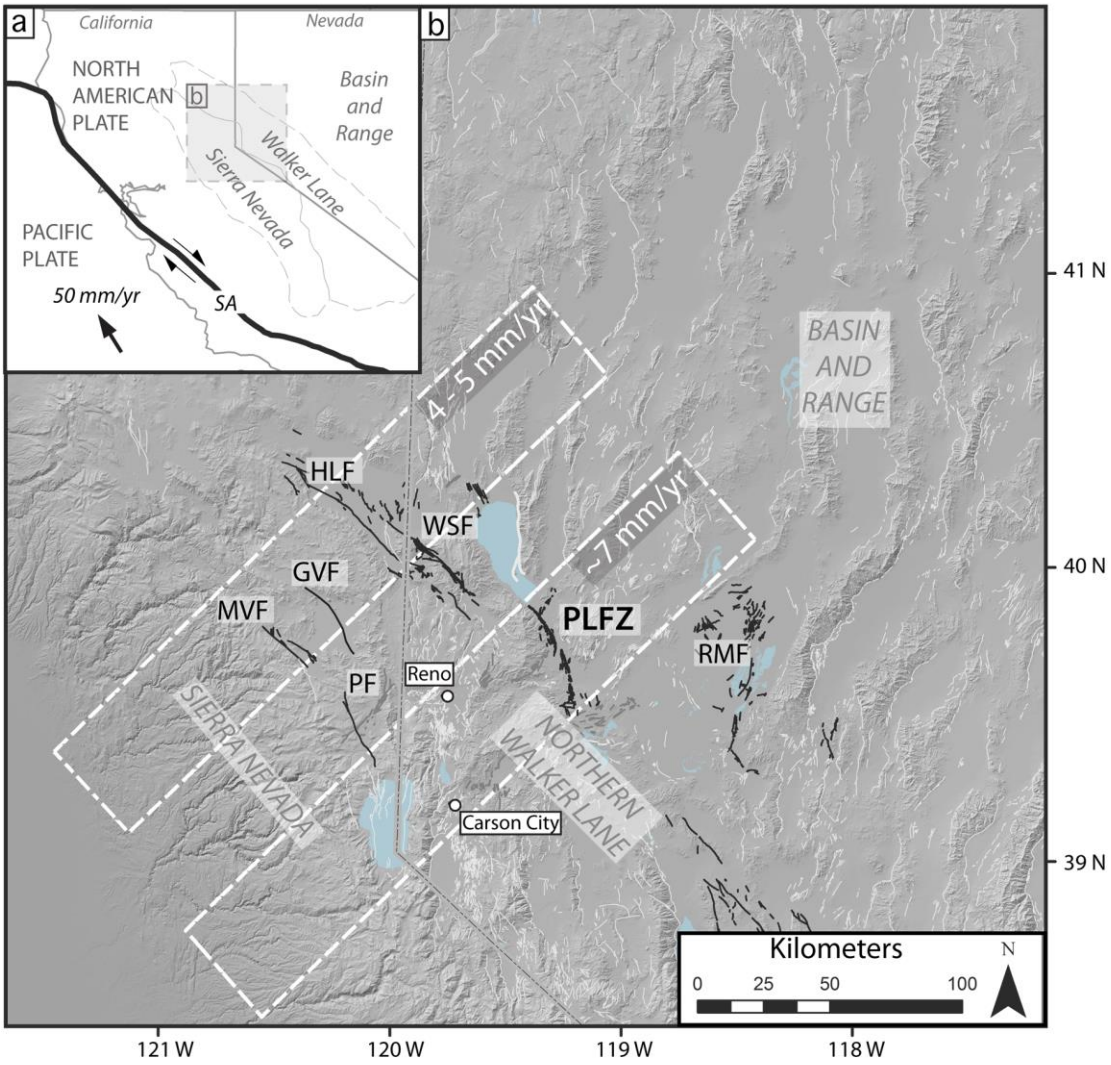

Figure 1. (A) Regional tectonic setting of the study area and its relation to the San Andreas (SA) fault system. (B) Regional hillshade and fault map of study area. Northwest trending right lateral strike slip faults accommodating Walker Lane right-lateral shear are shown as solid black lines (PLFZ – Pyramid Lake fault zone; PF –Polaris Fault, MVF – Mohawk Valley Fault, GVF – Grizzly Valley Fault, HLF–Honey Lake Fault, WSF – Warm Springs Fault, RMF – Rainbow Mountain Fault). Normal faults are shown in light gray. All faults modified from the U.S. Geological Survey Quaternary fault and fold database (2006). White dashed boxes show geodetic transects from Bormann (2013) used to constrain strain rates for the northern Walker Lane.

strike-slip fault of its 50 km length (Wells and Coppersmith, 1994; Wesnousky, 2008).

In this paper, we present new observations of tectonically displaced geomorphic features along the PLFZ acquired from high-resolution (< 20 cm) digital elevation models (DEMs) developed from structure from motion (SfM) processing of aerial photography obtained from a multirotor unmanned aerial vehicle (UAV). The observations suggest a lower slip rate for the PLFZ and help resolve inconsistencies between per-event displacements predicted from previously slip rate estimates and potential rupture length of the PLFZ.

Geologic Framework

Pyramid Lake Fault Zone Surface Trace and Offset Potential

The PLFZ is expressed as a relatively narrow (< 2.5 km wide) fault zone that continues for ~45 km from Fernley, NV to the southern edge of Pyramid Lake as a northwest trending right lateral strike-slip fault (Figure 2). Recent marine shallow seismic reflection interpretations of Eisses et al. (2015) show west dipping strata focused at the southern end of Pyramid Lake, suggesting that PLFZ may extend for another 5 km as an east dipping oblique fault along west-shore of lake, characterized with more vertical displacement than to the south. This extends the length of the PLFZ to ~50 km. Further north, the character of regional faulting changes to NNW trending normal faults (Figure 1), and is

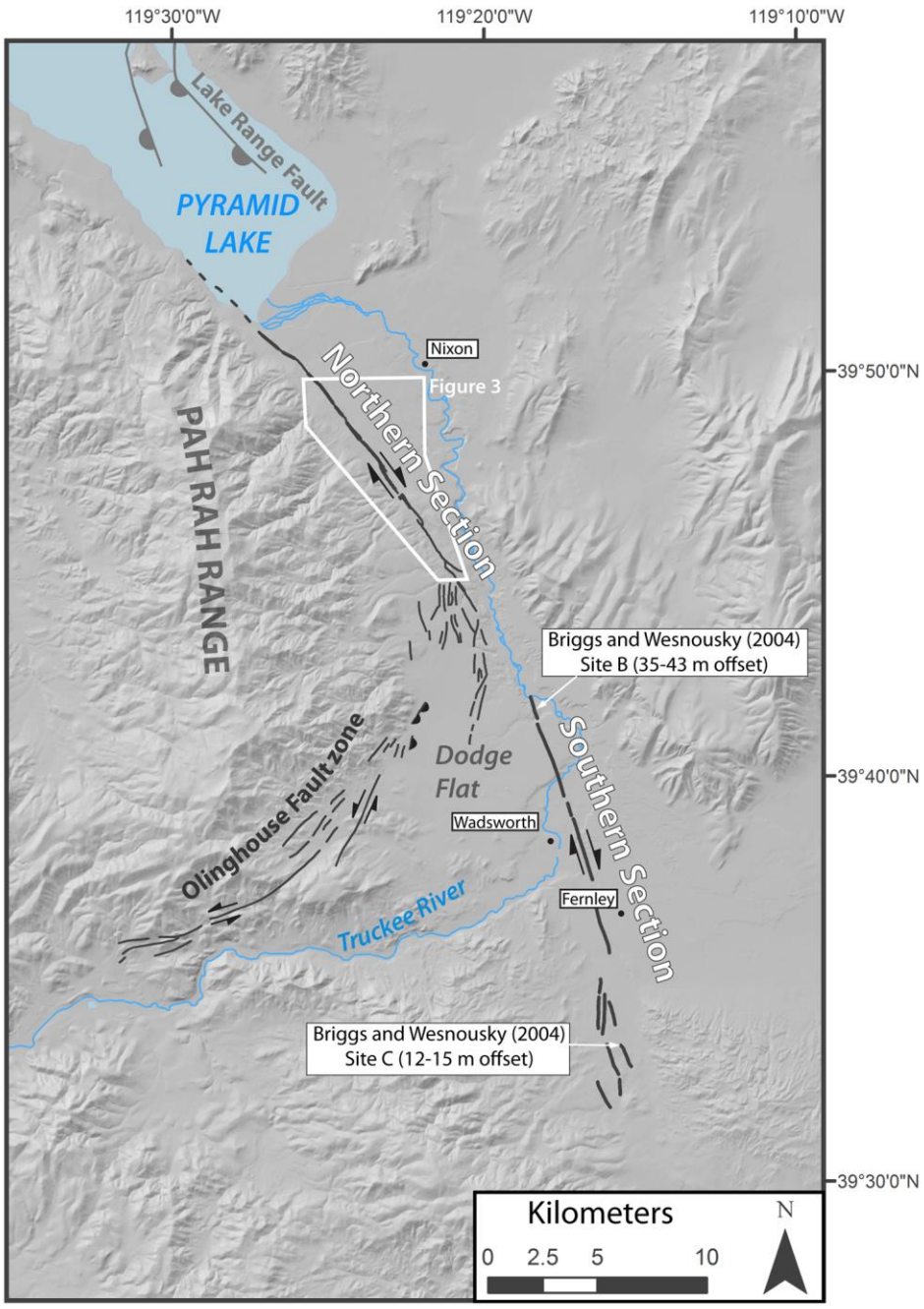

Figure 2. Map of PLFZ trace. Quaternary-active surface traces of the PLFZ are shown as thick black solid line and dashed where concealed. The normal Lake Range fault and left-lateral Olinghouse fault are shown as thin black lines. Half circles on fault lines show down dropped sides of normal faults. Location of Briggs and Wesnousky (2004) study sites referred to in text is labeled.

dominantly express by the Lake Range fault that bounds the east side of the lake and dips to the west (Figures 1 and 2).

The emergent portion of the PLFZ has previously been divided into two sections based on geomorphic and structural observations (Anderson and Hawkins, 1984; Bell and Slemmons, 1979; Bell et al., 2005; Briggs and Wesnousky, 2004). The southern section of the PLFZ begins south of Fernley, NV and crosses Dodge Flat to where it parallels and is obscured by the steep bank of the Truckee River (Figure 2). The southern section of the fault zone is expressed as multiple aligned, discontinuous linear traces manifested as vegetation lineaments, scarps, and linear depressions within the middle of the valley. The northern limit of the southern section corresponds with the occurrence of distributed faulting and local extensional features near the intersection with the conjugate left-lateral Olinghouse fault (Briggs and Wesnousky, 2005; Sanders and Slemmons, 1996; Figure 2).

The PLFZ is best defined in the northern section and displays a nearly continuous linear fault trace manifested as vegetation lineaments, uphill-facing scarps, bedrock and alluvial ridges, elongate depressions, and springs (Figures 2 and 3). We targeted this portion of the fault because it crosses numerous gullies, drainage channels, and ridges, providing higher potential for preservation of displaced geomorphic features.

Geomorphic Units and Geochronologic Constraints

The PLFZ sits within the Pyramid Lake basin, which was once part of Lake Lahontan, a pluvial lake that reached its maximum highstand (Sehoo highstand) of ~1338 m at 15,475 ± 720 cal. Yr B.P. (15.5 ka) before rapidly desiccating to modern-day Pyramid Lake level (Adams et al., 1999; Benson and Thompson, 1987; Briggs et al., 2005). Remnant shoreline features such as shoreline scarps, spits, tufa deposits, and modified fan surfaces are prevalent within Pyramid Lake basin and provide excellent late Pleistocene and Holocene geomarkers of lake level (Reheis et al., 2014). Study of such features has generated detailed Lahontan lake-level curves (Adams, 2012; Adams et al., 1999; Benson and Thompson, 1987; Briggs et al., 2005) that show the Sehoo highstand (~15.5 ka) to be abrupt, characterized by a rapid transgression that reached a maximum elevation of ~1337 m and followed by a rapid regression (Adams and Wesnousky, 1998; Benson and Thompson, 1987; Benson et al. 1995; Thompson et al, 1986). Later, minor transgressions occurred during the late Pleistocene (10,820 ± 35 14C yr B.P.) and the late Holocene (3,595 ± 35 14C yr B.P.), reaching elevations of ~1230 m and ~1199 m, respectively (Briggs and Wesnousky, 2005; Figure 3). Previous mapping by Briggs and Wesnousky (2004) show the distribution of late Pleistocene and Holocene shorelines and deposits along the northern section of the PLFZ (Figure 3), and is utilized in this study to constrain the age of offset.

The trace of the PLFZ, from which we document seven offsets, lies almost entirely below the Lahontan Sehoo (~15.5 ka) highstand (Figure 3). Further north,

and closer to the modern shoreline, the trace of the fault is absent within the historic deposits of Pyramid Lake (Figure 2). To constrain the age of offset, we assume the ages of offset lacustrine features, such as constructional shoreline features, are bound by the corresponding highstand above and below, such that lacustrine features between elevations 1337 m and 1230 m have a maximum age of 15.5 ka and minimum age of 10.8 ka, and lacustrine deposits below 1230 m have a maximum age of 10.8 ka. Due to the brevity of the Sehoo highstand (15.5 ka) and rapid nature of the bounding transgression and following regression, we further assume that the age of offset deposits near the Sehoo highstand, whether they are transgressional or regressional in origin, to be very close in age to the highstand value of 15.5 ka. We therefore do not provide a minimum bound on deposits that sit within 15 meters of the Sehoo highstand. Offset erosional geomorphic features, such as incised drainage channels, are assumed to form sometime after the occupation of the lake, and are bound solely by the age of the Sehoo highstand (15.5 ka), providing a maximum age.

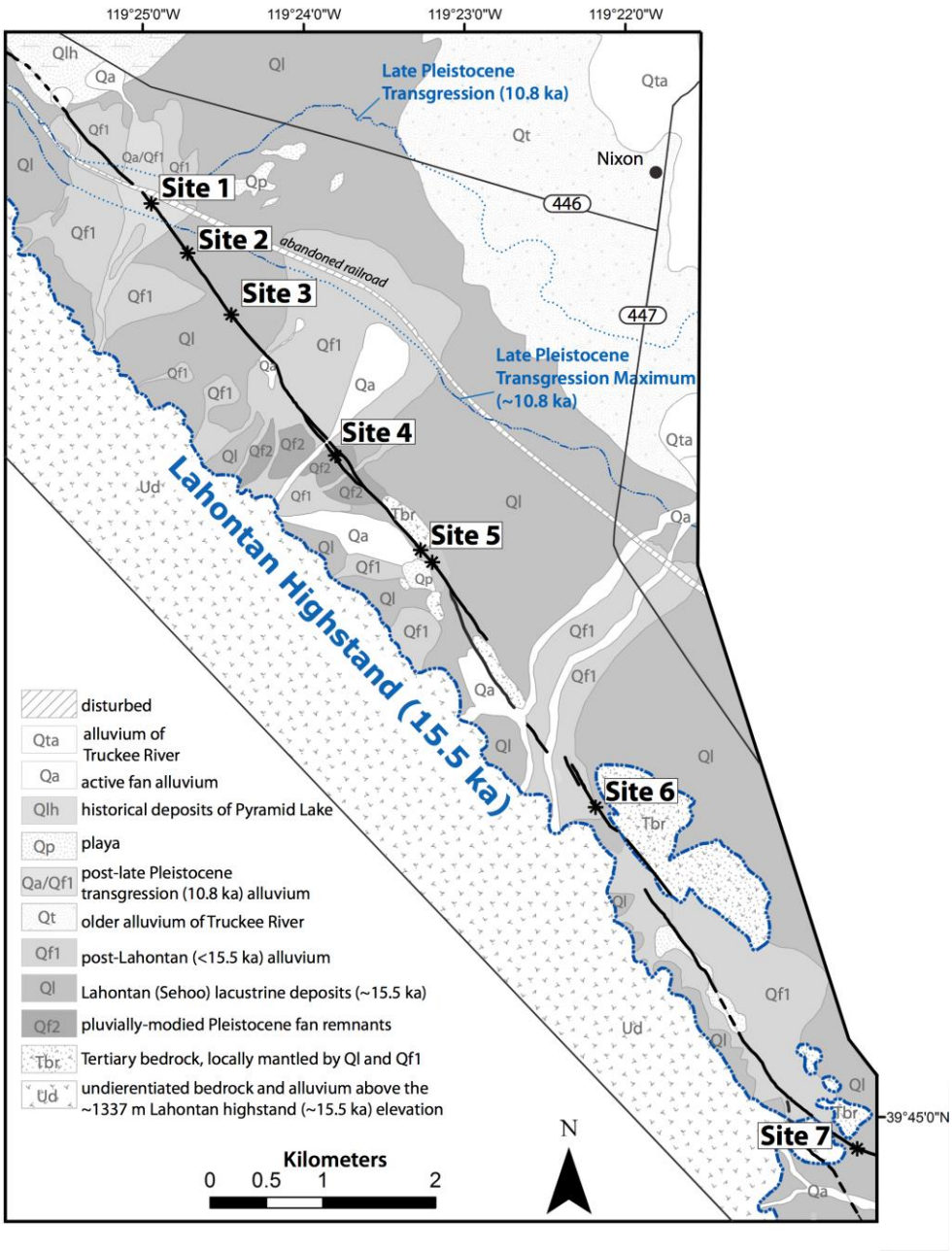

Figure 3. Surficial geologic map along the northern section of the PLFZ (modified from Briggs and Wesnousky, 2004). Fault trace shown as thick black line, dashed where concealed. Study sites 1 to 7 (asterisks) are shown along PLFZ. Contour of the Lahontan Sehoo highstand (15.5 ka) is shown by the thick dotted-dashed line. Contours of the late Pleistocene transgressions are shown with dotted-dashed lines and dotted line where concealed (continued along elevation contour of associated extent).

Methods

To produce high-resolution digital elevation models, we applied SfM to low altitude aerial photography obtained from a low flying remote-controlled multirotor hobby copter. Because this is a relatively new technique, especially within the field of geomorphology and neotectonics, we first provide a general summary of SfM followed by the methods we used.

Structure from Motion

Sprouting from stereo-photogrammetry, SfM developed during the late 1970's (Ullman, 1977, 1979), and has since rapidly progressed into simple automated workflows that, in combination with Multi-view Stereo (MVS) (Pollefeys et al., 2004), produce highly accurate 3-D point data comparable to standard light detection and ranging (LiDAR) (Harwin and Lucieer, 2012; Westoby et al., 2012). Recent applications of SfM include 3-D modeling of iconic solitary structures (Snavely et al., 2008), geologic outcrops (Westoby et al., 2012), various geomorphic landscapes (Fonstad et al., 2013; Johnson et al., 2014), and paleoseismic trench exposures (Bemis et al., 2014; Reitman et al., 2015).

SfM uses photogrammetric triangulation of common features from a series of overlapping photographs from different and multiple perspectives in order to determine the camera position of each photograph, producing a camera model. MVS then uses the camera model to construct the 3-D point model of the scene

photographed, where enhanced feature recognition algorithms allow for multi-scaled photographs to have large changes in camera perspectives, allowing for detailed scene geometry (Pollefeys et al., 2004). Feature color is also carried through the SfM/MVS process, providing red-green-blue values for each generated point. Recent applications and testing of SfM for topographic modeling show high levels of accuracies that are often comparable and sometimes better than standard LiDAR models (Fonstad et al., 2013; Harwin and Lucieer, 2012; Johnson et al., 2014; Westoby et al., 2012). Unlike LiDAR, SfM does not have the potential to acquire ground points through dense vegetation canopies.

High-Resolution Topographic Models

We developed SfM topographic models of offset geomorphic features at seven individual sites along the trace of the PLFZ using aerial photographs obtained from a UAV. Sites were selected for the highest potential to record fault offset of geomorphic features. Low altitude (< 30 m) aerial photographs were acquired at each site using a DJI Phantom 1 multi-rotor hobby copter mounted with a Ricoh GR 8.3 megapixel digital camera, with a 5.9 mm lens. Photo acquisition was focused along the trace of the fault, which allowed for the most photo overlap and highest ground resolution along the fault (Table 1). During flight, images were captured every 5 seconds producing ~100 – 950 photographs at each site, dependent on the size of the site (Table 1). Poor quality photos

such as those that were blurred, contained obstructions, or very low altitude photographs were discarded from the modeling process.

Ground Control Points (GCPs) were deployed before photo acquisition and incorporated in the modeling process to constrain scale. These consisted of 30 cm diameter orange disks set up ~50 m apart in rows of three perpendicular to the fault and spaced ~50 m apart. The center of each GCP disk was geospatially located using a Trimble R10 RTK GPS, providing 2 – 5 cm accuracy.

We followed a similar processing workflow procedures of (Johnson et al., 2014) using Agisoft Photoscan Pro software©. Dense point clouds of each site were produced in Photoscan using suggested default settings. The DEMs were developed within Photoscan using the dense point cloud and creating a triangulated irregular surface (aka. TIN). Suggested default settings were used in the TIN to maximize the face count, producing DEMs with 3 – 9 cm pixels (see Table 1). Our model accuracies, reported as root mean square (RMS) values, range from 7 – 50 cm (Table 1). Hillshade, slope, and contour maps were produced in ArcGIS from the exported DEMs, and further processed in ArcGIS for analysis and displacement estimates.

Vegetation filters were not used in our modeling process for the purpose of preserving the true landscape topography and due to the limited obstruction from local sagebrush. As a result, local sagebrush appears as irregular oval speckles within our hillshade models, and causes irregular contour lines to be rough and irregular, sometimes only encircling a single sagebrush. To minimize

these effects in our contour maps, we first applied a smoothing tool ('focal statistics' in ArcGIS) to our DEMs, which averages the value of each gridded cell over a defined area, 0.5 – 2 m in this case. We then removed contours encircling individual sagebrush using the contour line length as a filter, such that only long (> 15 m) continuous contour lines remain. Our hillshade images are not smoothed for the purpose of showing the landscape at highest resolution.

Table 1. Structure from motion modeling parameters and results.

Site	Model Area (m^2)	Number of images	GCPs	Point Density ($points/m^2$)	Ground Resolution ($m/pixel$)	RMS (m)
1 and 2	189,278	971	43	130	0.04	0.07
3	101,181	326	11	238	0.06	0.09
4	78,432	88	18	1159	0.03	0.2
5	445,386	558	10	121	0.09	0.26
6	131,812	381	14	206	0.07	0.11
7	122,681	338	7	167	0.08	0.5

Observations

We utilize our high-resolution hillshade, contour, and slope maps to define and estimate the amount of displacement and related uncertainties of linear geomorphic features (Figures 4 though 10). Linear geomorphic features such as ridge crests, shoreline scarp inflections, drainage thalwegs, and channel margins serve as piercing points that are used to reconstruct fault displacement. At some sites, extrapolation of these linear features to the fault is required and often results in asymmetric uncertainties.

As described earlier, the age of offset is determined by the age of the surface of which the offset geomorphic deposit or feature is manifested in (Figure 3). The offset age is further used to estimate a slip rate by dividing the displacement estimates by the age of the offset features. We provide minimum and maximum slip rates where the offset age is bound by Lahontan highstands, and for those offset features not bound, such as incised drainage channels, we provide only a minimum rate.

Site 1

Site 1 is located in the northern end of the PLFZ, ~4 km south of the modern-day shoreline (Figure 3). An uphill-facing fault scarp (Figure 4a) cuts across a Qa/Qf1 fan that postdates the ~10,820 ± 35 B.P. late Pleistocene transgression of Lake Lahontan. The fan at this location is characterized by relatively higher older incised surfaces that sit within the interfluves of slightly lower younger surfaces (Figure 4a). The lower younger surfaces have a slightly smaller fault scarp and do not show offset within the incised drainages. Within a relatively older portion of the fan, a beheaded drainage channel is observed on the northeast side of the fault (Figure 4). We interpret the thalweg of the correlative channel to be offset right-laterally 17 ± 2 m on the southwest side of the fault (Figure 4b). The qualitative uncertainty of the estimate reflects the poorly defined nature of the channel thalweg near the fault and on the southwest side of the fault (Figure 4b). Assuming the displacement is tectonic and has accrued

since the deposition of the alluvial fan unit (Qa/Qf1), the observations indicate a minimum slip-rate of 1.6 ± 0.2 mm/yr.

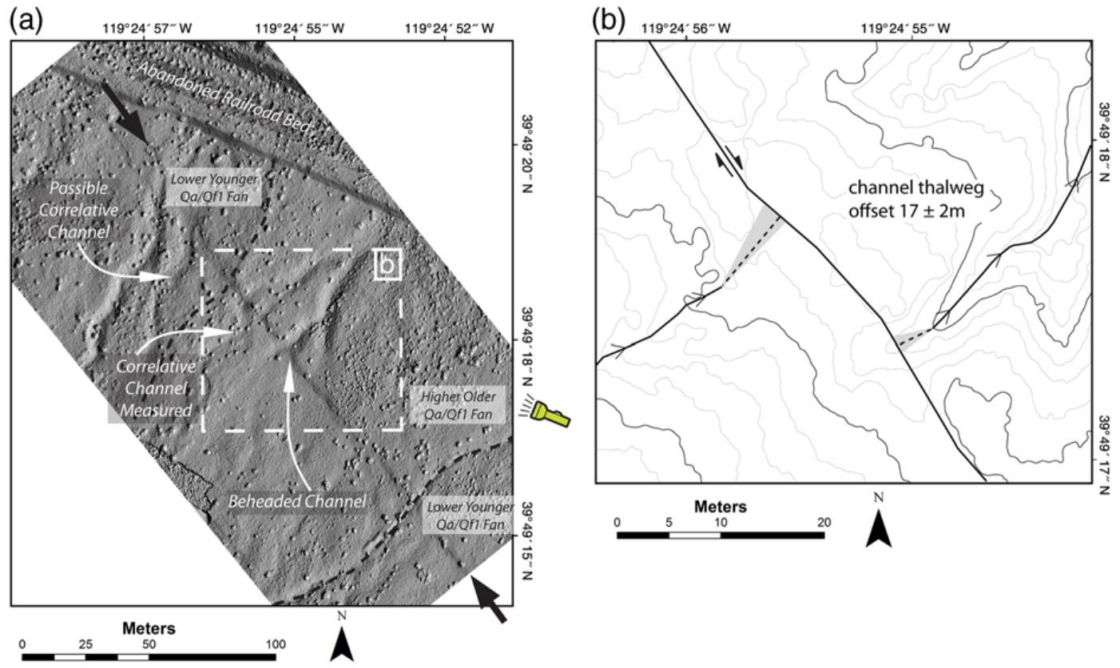

Figure 4. Site 1. a) Hillshade map of fault trace and right-laterally displaced beheaded channel. b) Contour map showing offset thalweg (solid and dotted thin black line). Contour interval is 25 cm, thicker contours every 1-meter. Uncertainty within the projection of the offset thalweg to the fault trace is indicated by shaded area.

We acknowledge another potential correlative channel on the southwest side of the fault, further north, that might be correlated to the beheaded channel (each labeled in Figure 4a), and leads to an apparent right-lateral offset measurement of ~60 m. Because the correlative drainage sits within a relatively younger portion of the fan and the magnitude of this offset is very large given the youthful age of the surface of which the offset is manifested in (less than ~10.8

ka), we disregard the offset as it is unlikely tectonic. The offset would indicate a minimum slip rate of 5.5 mm/yr, well above prior findings (Briggs and Wesnousky, 2004) and others from this study, and limits placed by contemporary geodesy (Bormann, 2013; Hammond et al., 2011).

Site 2

The fault at Site 2 is expressed as a single linear uphill-facing scarp (up to ~1.5 m high) within Ql lacustrine deposits (Figures 3 and 5). An abandoned channel intersects the fault at high angle (Figure 5a) and is right-laterally offset (Figure 5b). The channel morphology is broad and muted, particularly on the southwest side of the fault, and introduces a moderate amount of uncertainty. Additionally, a secondary drainage, flowing north along the uphill facing scarp, disrupts the morphology of the offset channel near the fault, and adds to the uncertainty. We estimate 14 ± 6 m of right-lateral displacement of the thalweg across the fault (Figure 5b). This channel incised into Ql lacustrine deposits sometime after the regression from the Sehoo highstand (~15.5 ka), the offset post-dates ~15.5 ka and results in a minimum slip rate estimate of 0.9 ± 0.4 mm/yr.

Site 3

Site 3 is located ~0.75 km southeast of Site 2 where the fault is also expressed within Ql lacustrine deposits (Figures 3 and 6). A broad constructional shoreline ridge intersects the trace of the Pyramid Lake fault at a highly oblique

angle (Figure 6a) and its crest is offset 15 ± 10 m (Figure 6b). The broad nature of the ridge and its oblique intersection with the fault leads us to assign a relatively high uncertainty to the offset estimate. The offset Ql deposit here sits between the 15.5 ka Sehoo highstand and the 10.8 ka transgressional maximum, and so the offset measurement places a minimum bound on the fault slip rate of about 1.0 ± 0.6 mm/yr and a maximum rate of 1.4 ± 0.9 mm/yr.

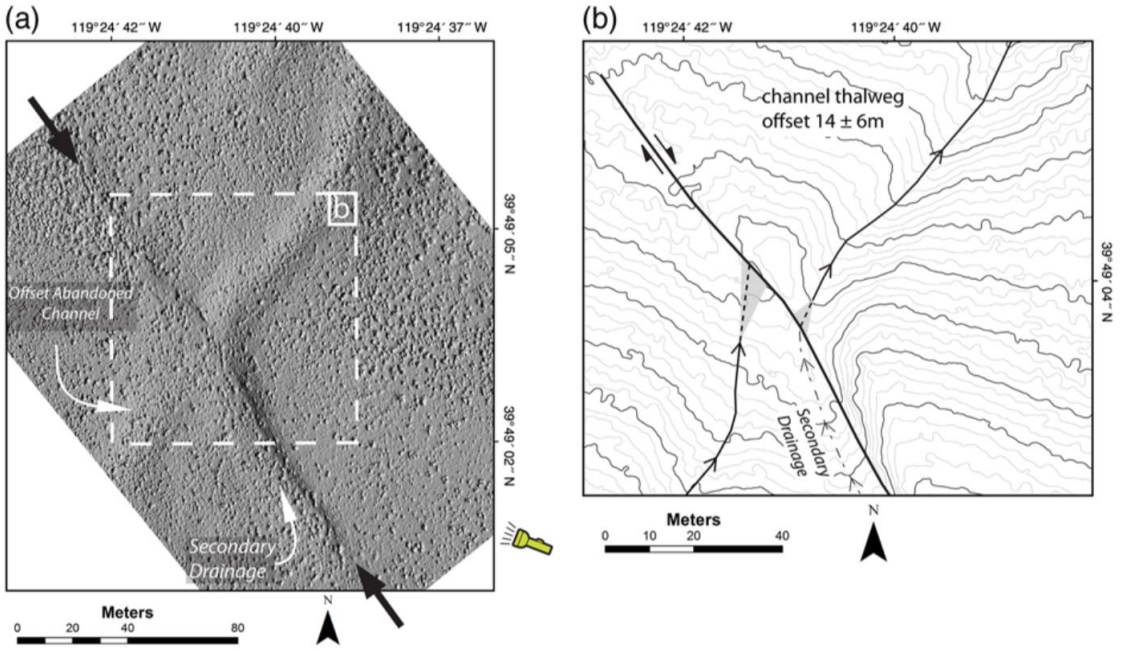

Figure 5. Site 2. a) Hillshade map showing fault trace and right-laterally offset channel. b) Contour map showing offset thalweg (black solid and dotted line). Contour interval is 25 cm, thicker contours every 1-meter. Uncertainty in projection of offset thalweg to trace indicated by shaded area. Uncertainty within the projection of the offset thalweg to the fault trace is indicated by shaded area.

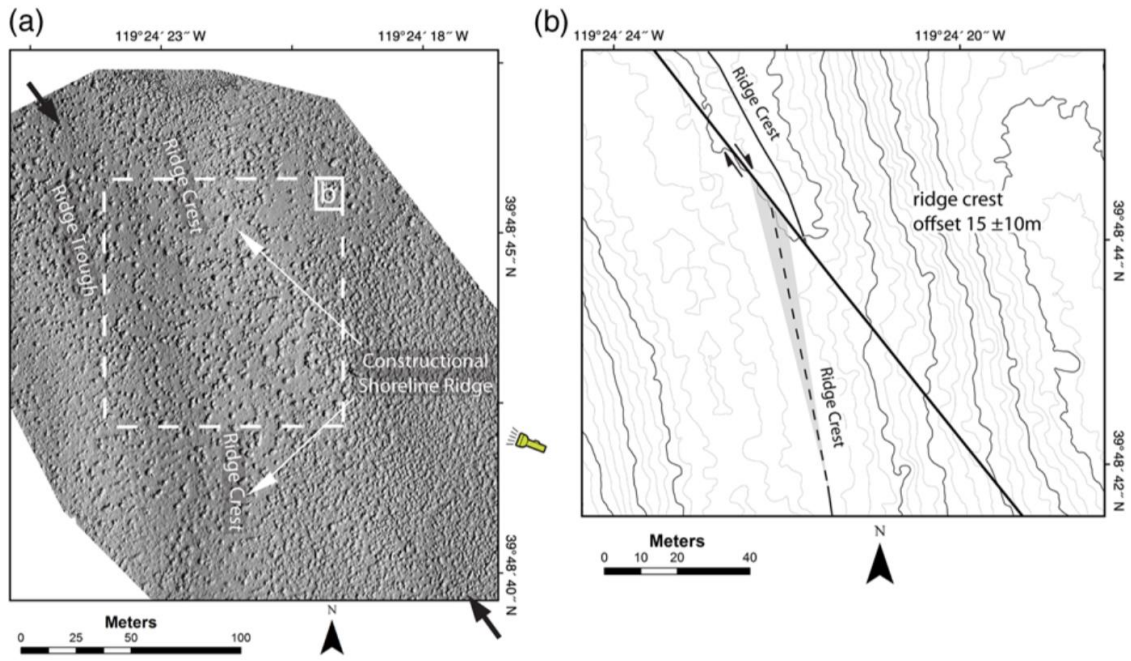

Figure 6. Site 3. a) Hillshade map showing subtle fault trace and constructional shoreline feature. b) Contour map showing offset ridge crest (black dashed line). Contour interval is 25 cm, thicker contours every 1-meter. Uncertainty within the projection of the offset ridge crest to the fault trace is indicated by shaded area.

Site 4

The fault at Site 4 is composed of two fault strands and forms a graben structure across Qf2 (Figures 3 and 7). An abandoned drainage channel crosses both fault strands (Figure 7a). The broad nature of the channel reduces our ability to constrain the thalweg using the contours (Figure 7c). Instead, we use sharp slope breaks, determined on the generated slope map (Figure 7b), of the upper channel margin walls as piercing points (small arrows in Figure 7b). The northern channel wall is the most well-defined, and best records offset of the

channel where it crosses the northeastern fault strand. We estimate 14 ± 2 m of right-lateral offset, similar to the offset estimate of 12 – 15 m at this site previously reported by Briggs and Wesnousky (2004). The sharpness of the slope break and its continuous nature to where it intersects the fault scarp allows us to assign a minimal uncertainty to the offset estimate. The southern margin of the channel is partly eroded and has a more muted slope break associated with the top of the southern channel margin wall. This is especially apparent east of the northeastern fault strand, and does not provide a sufficient piercing point to measure.

Additional offset is recorded on the southwestern strand of the fault. The slope breaks at the top of both channel margin walls are well-defined, particularly along the southern channel margin. We estimate that both the northern and southern channel margins are similarly offset 3 ± 1 m. This offset was not observed by Briggs and Wesnousky (2004) and increases the total offset across the two fault strands to 17 ± 3 m. The accumulated offset of the drainage channel post-dates the Lahontan highstand (15.5 ka), and yields a minimum slip rate estimate of 1.1 ± 0.2 mm/yr.

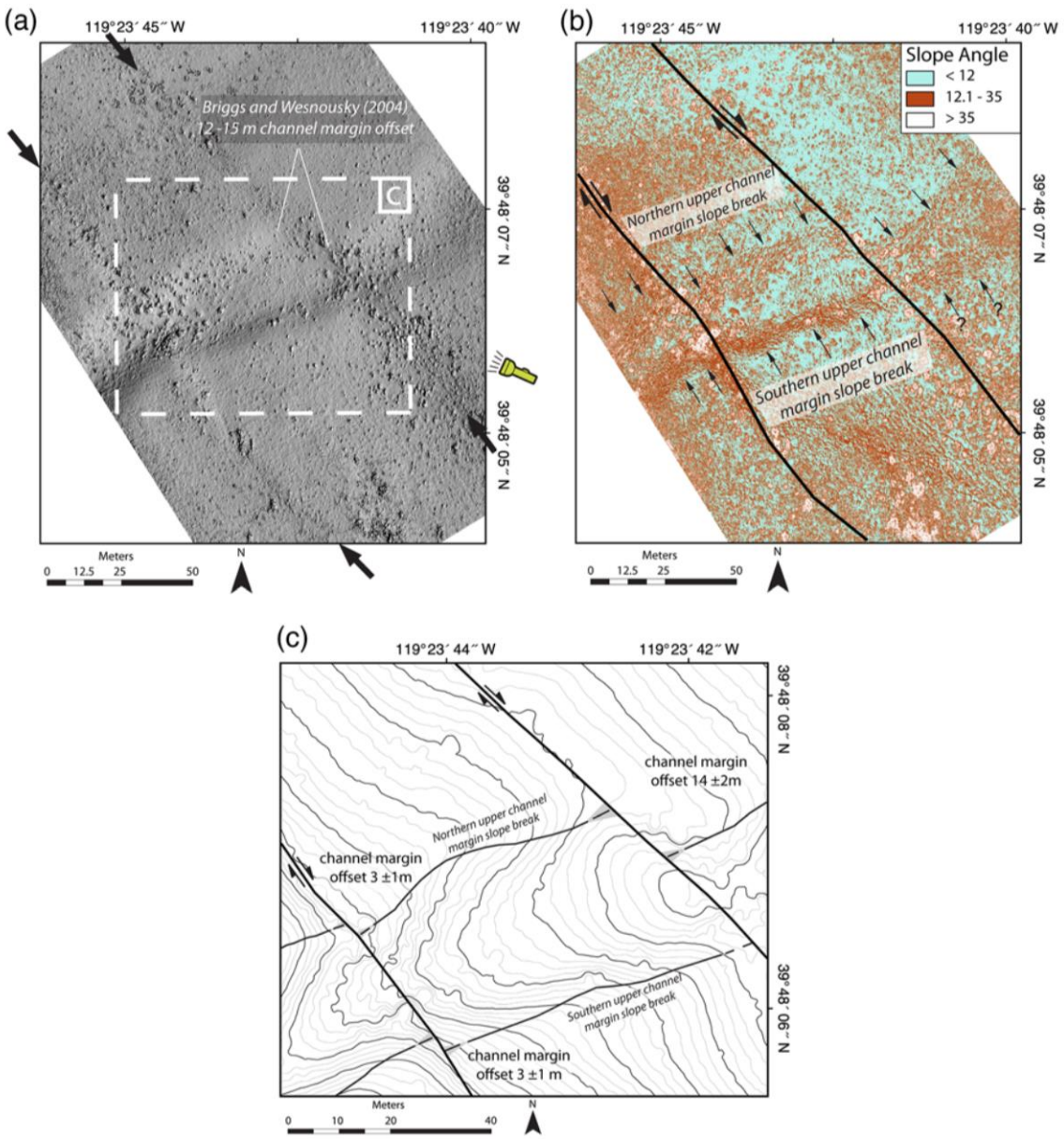

Figure 7. Site 4. a) Hillshade map showing offset drainage and two strands of the PLFZ. b) Slope map highlighting the top of channel margin walls (arrows) determined from sharp break in slope. c) Contour map showing offset channel margins (solid and dashed black lines) on each fault strand (solid black lines). Contour interval is 25 cm, thicker contours every 1-meter. Uncertainty within the projection of the break in slope that defines the channel margins to the fault strands is indicated by shaded areas.

Site 5

Site 5 is located at the southern end of a long (~1 km) linear NW-trending wave-washed bedrock-cored ridge (Figures 3 and 8a). The PLFZ intersects and displaces two broad but distinct shoreline ridges deposited on the bedrock-cored ridge (Figure 8a). The crest of the northwestern ridge is right laterally offset 21 ± 8 m (Figure 8b), while the better-defined southeastern ridgeline is offset 20 ± 5 m (Figure 8c). Using the age of the Sehoo highstand (15.5 ka) as a maximum bound on the age of the displaced shoreline ridges, and using the larger measured offset (21 ± 8 m) we estimate a minimum fault slip rate of 1.4 ± 0.5 mm/yr. This site also sits well above the 10.8 ka transgressional maximum, providing a minimum bound on the age of offset and provides a maximum slip rate estimate of 1.9 ± 0.7 mm/yr.

Site 6

At Site 6, arcuate constructional shoreline ridges, that lie just below the Sehoo highstand (~1337 m), intersect the ~1 m-high uphill-facing fault scarp at high angle (Figures 3 and 9a). The break in slope on the northwest face of this shoreline ridge (Figure 9b) is right-laterally offset 19 ± 9 meters (Figure 9c). The offset has accrued, at least, since the Lahontan highstand (15.5 ka), yielding a minimum slip rate estimate of 1.2 ± 0.6 mm/yr. Because of the proximity (< 15 m) to the highstand, we assume this shoreline feature is very close in age to the Sehoo highstand (15.5 ka), and therefore we do not provide a minimum age of offset.

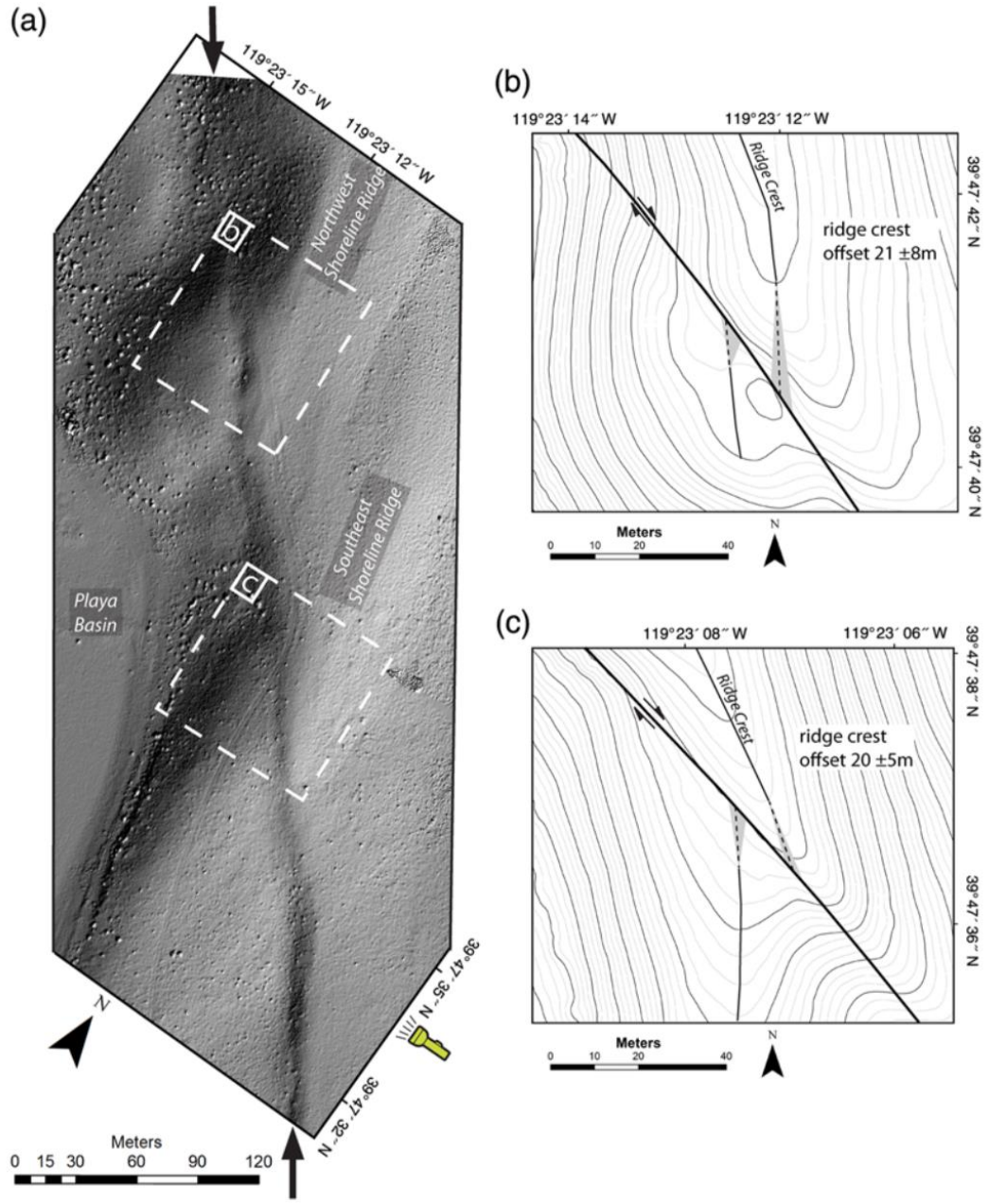

Figure 8. Site 5. a) Hillshade map showing fault trace and offset shoreline features. b) and c) contour maps of northwestern (b) and southeastern (c) offset shoreline ridges. Solid and dotted black lines show trace of ridge crests. Contour interval is 25 cm, thicker contours every 1-meter. Uncertainty within the projection of the slope break to the fault trace is indicated by shaded area.

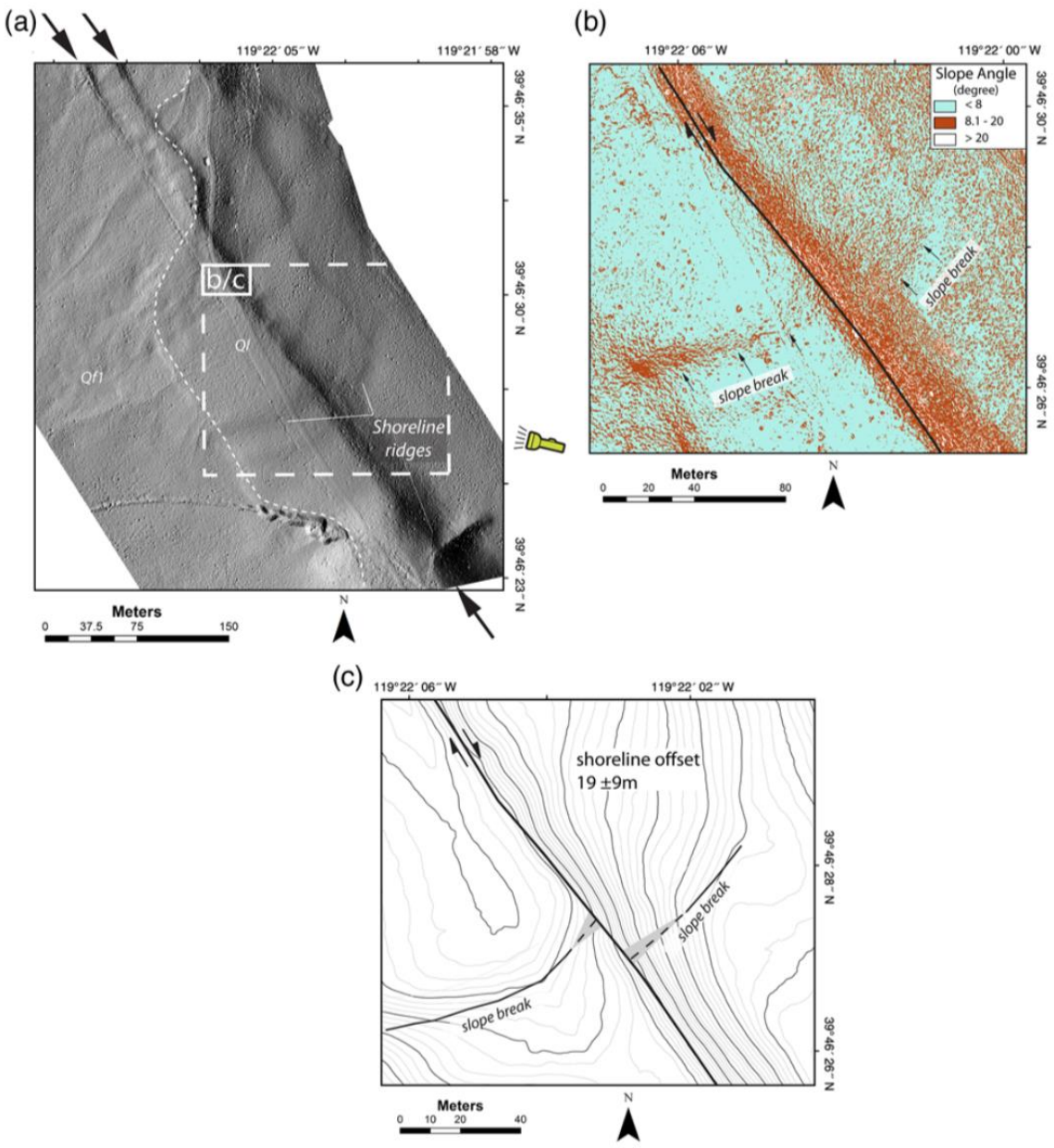

Figure 9. Site 6. a) Hillshade map showing uphill facing scarp and offset shoreline ridges. b) Slope map defining slope break (arrows) on northwest face of the shoreline ridge. c) Contour map showing projection of slope break into the fault (solid and dotted black lines). Contour interval is 25 cm, thicker contours every 1-meter. Uncertainty within projection of the slope break to the fault trace is indicated by shaded area.

Site 7

Site 7 is located at the southern end of a linear bedrock-cored ridge (Figure 3). Here, shoreline escarpments that sit just below the Sehoo highstand wrap around the southern tip of the ridge (Figures 3 and 10a). The fault trace is subtle and is better manifested by the offset of the shoreline (Figure 10). The trend of the shoreline feature is best defined by the slope break at the top of the southeast-facing shoreline escarpment (Figure 10b), which is offset 8 ± 3 m across the fault zone (Figure 10c). The observed displacement has occurred since the formation of the shorelines, which must be very near to 15.5 ka in age since it lies just below the Sehoo highstand. We estimate a slip rate of 0.5 ± 0.2 mm/yr. Multiple fault traces exist at the latitude of this site (Figures 2 and 3). Our slip rate estimate here is for only one fault strand and is unlikely to have captured the entire near-field fault offset. Accordingly, the slip rate estimated here is relatively less than our other six sites.

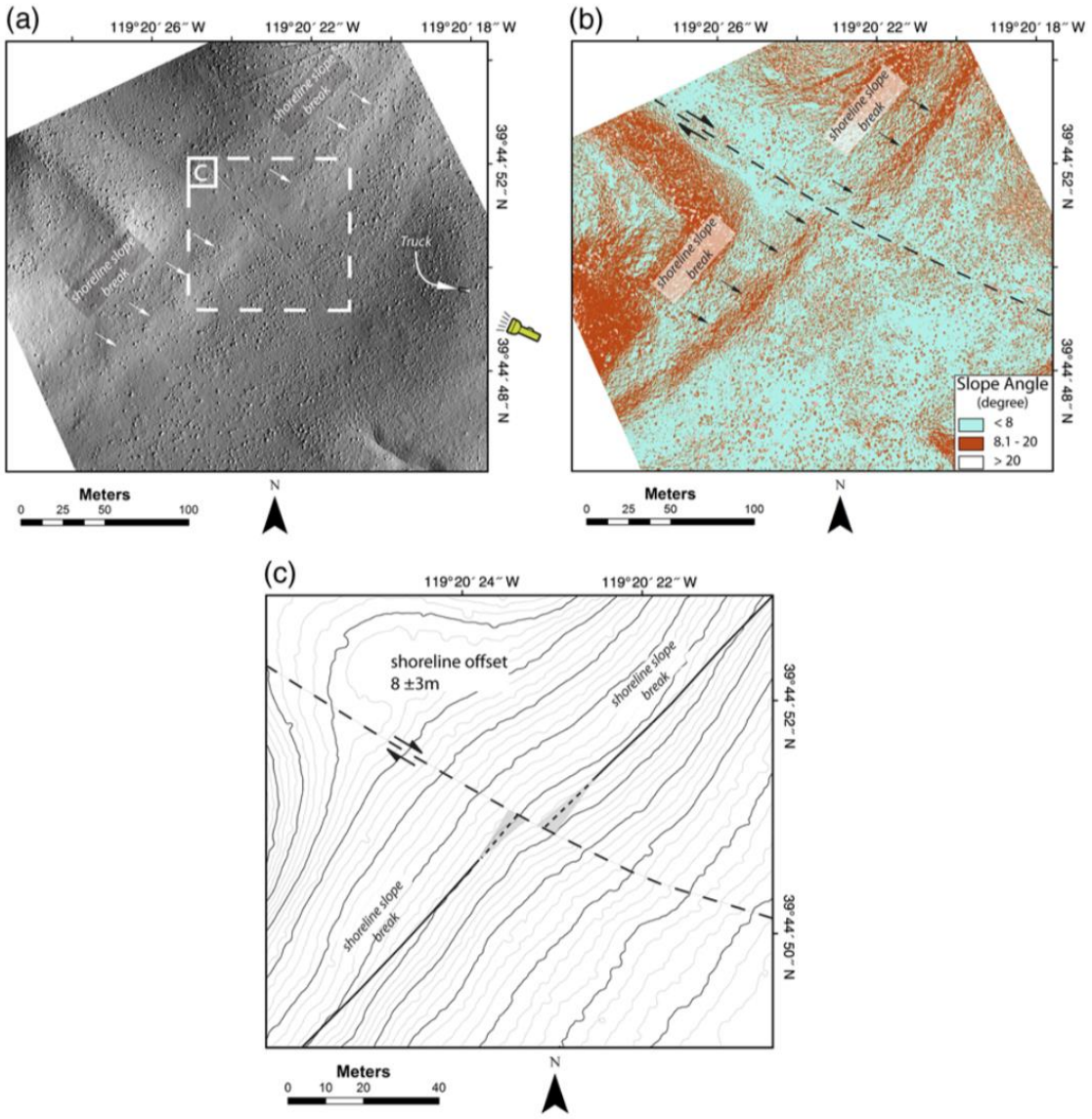

Figure 10. Site 7. a) Hillshade map showing offset shoreline ridge. b) Slope map defining slope break (arrows) on south face of the shoreline ridge. c) Contour map showing displacement measurement of shorelines (traced with solid and dotted black lines). Contour interval is 25 cm, thicker contours every 1-meter. Uncertainty within the projection of the slope break to the fault trace is indicated by shaded area.

Discussion and Conclusion

Our efforts provide a useful example of the application of small, low-cost UAV photography in neotectonic analysis. In this case, development of high-resolution digital elevation models has resulted in the addition of seven measurable fault offsets along the PLFZ, more than a doubling the previous amount of offset measurements from prior study along the entire fault that used 1:10k scale low-sun-angle photography (Briggs and Wesnousky, 2004). In turn, these measurements provided us the ability to further evaluate the latest Pleistocene to Holocene slip rate of the PLFZ and its role in accommodating strain within the Walker Lane.

Reconciling Slip Rates on the Pyramid Lake Fault Zone

The offsets we observe at the seven sites range from 8 to 21 m, and yield slip rates ranging from 0.5 to 1.9 mm/yr (Figure 11). The uncertainties we place on all are qualitative, in some cases quite large, and little weight might be given to any individual estimate. Together, minimum and maximum estimated slip rates from this study provide an average slip rate of 1.3 ± 0.4 mm/yr, and amongst all of the slip rates determined along the entire PLFZ, including prior studies, all but two (site 7 and site B of Briggs and Wesnousky, 2004) fall within this average slip rate (Figure 11). Site 7 from this study was expected to be less as it is located where multiple fault traces exist, and is likely not capturing all the slip. A principal observation, excluding site 7, is that our slip rate estimates are broadly consistent among the six sites along the 17 km-long portion of the PLFZ

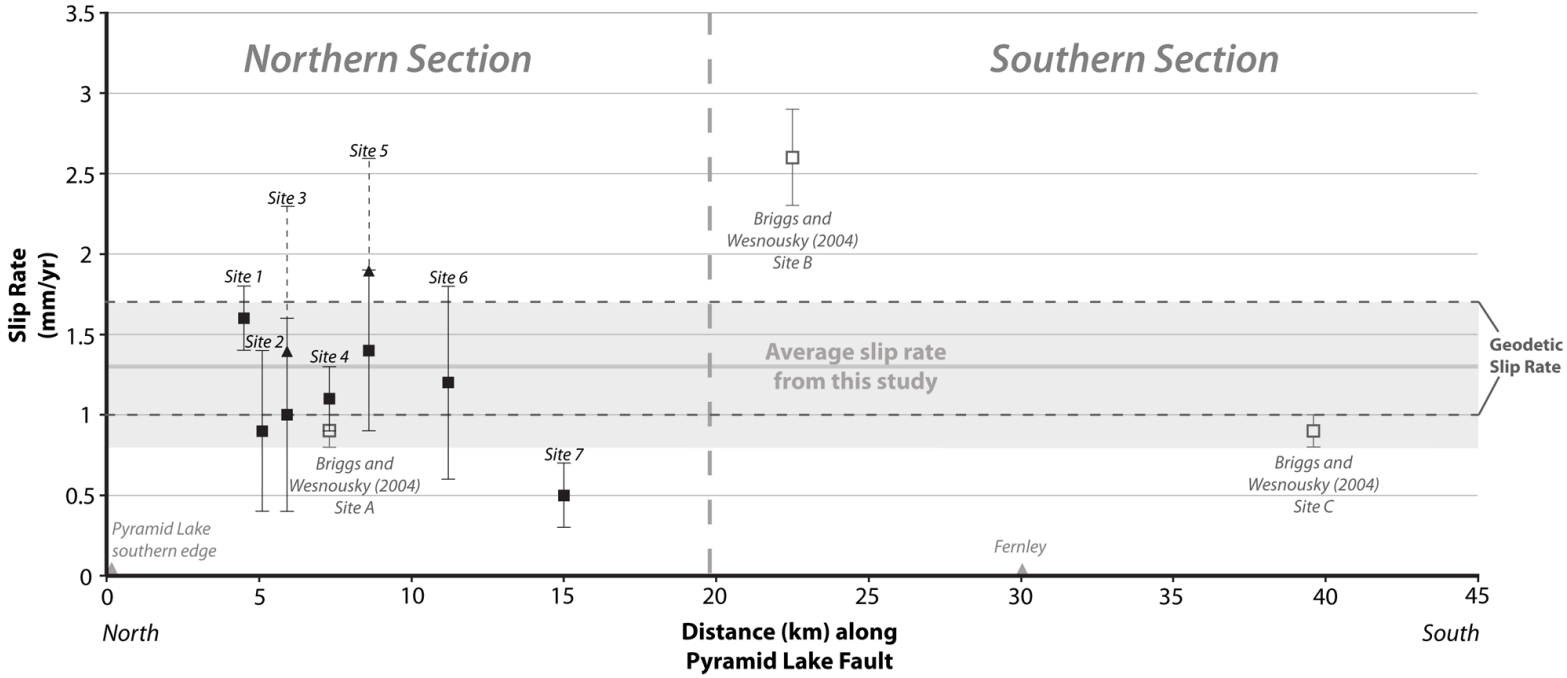

Figure 11. Summary of slip rate estimates along the PLFZ. Solid black boxes are minimum slip rates obtained from this study with associated uncertainties shown by extending solid black lines. Black triangles show the maximum slip rates obtained in this study and associated uncertainty shown as extending dotted lines. Grey shaded region and thick solid grey line display average slip rate range obtained from this study. Slip rates and associated uncertainties from Briggs and Wesnousky (2004) shown as hollow dark grey boxes. The dashed lines bound the limit of slip rates estimated for the PLFZ from block modeling of contemporary geodetic data (Bormann, 2013; Hammond et al., 2011). Thick vertical dashed line show approximate location between the northern section and southern section of the PLFZ

that we have studied and are invariably less than 2 mm/yr (Figure 11). The values of our estimates are also less than the previously reported slip rate for the PLFZ, which was based on offset drainages at a single site, along the Truckee River, about 7 km to the south of our most southern site (Figures 2 and 11; Briggs and Wesnousky, 2004). There, drainages are interpreted to have incised into lacustrine deposits after the Sehoo highstand (post-15.5 ka), similar to most of the sites of offset reported in this study, and are reported to be offset 35 – 43 m. Such an offset yields a latest Pleistocene to Holocene slip rate of 2.6 ± 0.3 mm/yr, which is ~200–500% higher than the slip rates we document 7 – 20 km to the north.

Importantly, all of the measured offsets here and in Briggs and Wesnousky (2004) provide a minimum slip rate. This means that slip rate calculations, other than at Site 1, assume that the age of the Sehoo highstand (15.5 ka) marks the time at which offset features begin recording displacement. Some disparity in rates might arise because some of the offset drainages did not develop immediately upon desiccation of the lake. Yet, several of the sites we measure (sites 6 and 7) are shoreline depositional features, which developed very close in time to the Sehoo highstand and would be expected to record all of the displacement since the highstand. Additionally, our largest measurement of offset (site 5) is also of displaced lacustrine depositional features that post-dates the Sehoo highstand and predates the late Pleistocene transgression (10.8 ka). It

is unlikely that the observed variation in slip rate along fault strike from our measurements have not captured the majority of slip since the highstand.

Our estimates of offset and slip rate are located along the northern section of the PLFZ, whereas the higher slip rate reported by Briggs and Wesnousky (2004) was determined along the southern section of the fault (Figure 2 and 11). The two sections of the fault are separated by the junction of the conjugate left-lateral Olinghouse fault (Figure 2), which forms a kinematically and structurally complex zone near the intersection. It might be suggested that the southern section of the fault is indeed slipping faster than the northern section as slip from the southern section is being transferred in part to the Olinghouse fault. This would kinematically require a component of reverse slip on the Olinghouse fault. However, the trace of the Olinghouse fault exhibits extensional features near its intersection with the PLFZ (Bell et al., 2005; Briggs and Wesnousky, 2005) and thus, this idea does not support the disparate slip rates for the southern and northern fault sections.

It could also be suggested that the large offset of Briggs and Wesnousky (2004) is the result of the central location of the offset site along the entire fault, where highest amounts of slip are to be expected (e.g. Bürgmann et al., 1994; Jónsson et al., 2002). Our observations do not refute this idea since they are all located to the north and are of lesser value. The large offset of Briggs and Wesnousky (2004) is located only 7 km south of our smallest measured offset (8

± 3 m), and would suggest a significant decay in slip amount within a short distance.

Two observations support the notion that a lesser value of slip rate than the previously reported 2.6 mm/yr is a better representation of the Pyramid Lake fault slip rate. First, the range of the best estimated slip rates (0.5 – 1.6 mm/yr) reported in this paper is consistent with recent geodetically estimated slip rates for the Pyramid Lake fault, which range from 1.0 – 1.7 mm/yr (Figure 11; Bormann, 2013; Hammond et al., 2011). Second, the displacements measured in this study yields greater consistency with the paleoearthquake history of displacement that has been reported along the fault.

Previous paleoseismic trenching along the northern section of the Pyramid Lake fault has shown evidence for at least four, possibly five, seismic events since the 15.5 ka Lahontan Sehoo highstand (Anderson and Hawkins, 1984; Briggs and Wesnousky, 2004). The latest three are determined to have occurred after 8980 ± 260 cal yr B.P., constraining the reoccurrence interval to ~2910 – 3080 years (Briggs and Wesnousky, 2004). Together these observations suggest that the higher number of earthquakes (five) satisfies the reoccurrence interval. If these five events are responsible for the latest Pleistocene displacement along the fault, the 35 – 42 m of offset reported in Briggs and Wesnousky (2004) requires that individual coseismic displacements have averaged 7 – 9 m, significantly larger than would generally be expected from empirical scaling relationships for a strike-slip fault of its 45 km length (Wells and

Coppersmith, 1994; Wesnousky, 2008). The range of offsets reported here is significantly less, ranging from 14 to 21 m. These offsets require that coseismic offsets average only between 3 – 5 m, more in line with the magnitude of displacements predicted by regressional relations derived from historical earthquakes (e.g. Wells and Coppersmith, 1994; Wesnousky, 2008).

The absence of a paleoearthquake record on the southern section of the PLFZ allows for the possibility of the southern section to rupture independently, and possibly contain more events, which would allow for the higher amount of observed slip. This would require many more events on the southern section than the northern, and expression of this is lacking within the geomorphology along the southern section of the fault.

In the end, our observations don't directly disprove the higher slip rate reported in Briggs and Wesnousky (2004). However, they do permit the suggestion that the part of the offset on which their high slip rate estimate was based, may record some component of stream deflection as well as offset, and thus overestimates the true offset along the fault.

Implications to Northern Walker Lane Kinematics

Mismatch between geodetic strain rates and geologic slip rates persist within the Walker Lane. This issue has been exemplified in the northern Walker Lane (Gold et al., 2013; Wesnousky et al., 2012), where the total geologic slip rate of 1.4 – 3.3 mm/yr, summed across the Mohawk Valley fault, Grizzly Valley

fault, Honey Lake fault, and the Warm Springs fault (Figure 1), fails to match the most recent geodetically determined rate of ~5 mm/yr (Bormann, 2013; Hammond et al., 2011).

This mismatch also exists further south (Wesnousky et al., 2012), at the latitude of the PLFZ, and is exacerbated by the new slower rates presented in this study (Figure 11). Here, recent geodetic rates estimate ~7 mm/yr of contemporary strain (Figure 1; Bormann, 2013). Summing the geologically determined slip rates of known active right-lateral strike-slip faults across this transect, which only includes 0.3 – 0.4 mm/yr on the Polaris fault (Hunter et al., 2011) and the < 2 mm/yr rate on the PLFZ from this study, yields a maximum slip rate of ~2.4 mm/yr. This yields a minimum deficit of ~4.2 mm/yr. It may be inferred from the deficit that 1) there is unidentified oblique slip on mapped normal faults, 2) there are unidentified active strike slip faults within the geodetic transect, 3) strike slip motion is being accommodated by some other means, such as block rotation (Wesnousky et al., 2012), 4) significant off-fault deformation occurs coseismically and cannot be observed by paleoseismology or near-field neotectonic studies such as this (Gold et al, 2015), or 5) unknown combinations of these possible explanations contribute to this deficit.

Implications to Seismic Hazard

If one accepts that the relatively lesser geologic slip rate we find for the PLFZ as compared to prior estimates from geology is correct, the consequence to seismic hazard in the nearby Reno area is twofold and in some

sense counteracting. Prior earthquake studies provide the best measures of the expected repeat time of earthquakes along the PLFZ and the reduction in slip rate reduces the magnitude of coseismic slip in repeating earthquakes needed to explain the slip rate. This in effect reduces the seismic hazard imposed by the fault on the Reno area. When coupling the observation of reduced slip rate with current geodetic observations that indicate shear equivalent to 7 mm/yr is accruing at this latitude of the Walker Lane (Bormann, 2013) and that the PLFZ marks the eastern margin of the Walker Lane, the slip once attributed to the PLFZ must ultimately be accounted for by slip and thus earthquakes on a fault or faults further west, perhaps closer to Reno, which would increase the level of seismic hazard for Reno. The finding of a lower slip rate on the PLFZ thus exacerbates prior observations in the northern section of the Walker Lane that geologic rates of slip are insufficient to account for the slip budget indicated by contemporary geodesy (Wesnousky et al., 2012; Gold et al., 2013).

Data and Resources

Base map data for Figures 1 and 2 were acquired from the National Elevation Dataset (http://ned.usgs.gov/about.html, last accessed August 2014). All other data in this article were self-collected in January – August 2014 and have not been previously published.

Acknowledgements

This research was supported in part by USGS NEHRP grant G13AP00033. We are truly grateful towards the Pyramid Lake Paiute Tribe for granting us permission to conduct this study on tribal lands. In particular, we thank Beverly Harry for her participation and guidance throughout the duration of our fieldwork. We also thank several UNR graduate students; Kyle Basler-Reeder, Greg Dering, Ian Pierce, and Courtney Brailo who assisted in the collection of data in the field. Reviews from Scott Bennett, Michael Bund, and associate editor Brian Sherrod significantly improved the quality and clarity of this manuscript, and we are appreciative of their insightful comments and suggestions. Any use of trade, firm, or product names is for descriptive purposes only and does not imply endorsement. This is Center of Neotectonics contribution number 66.

References

Adams, K. D., 2012, Response of the Truckee River to lowering base level at Pyramid Lake, Nevada, based on historical air photos and LiDAR data: Geosphere, v. 8, no. 3, p. 607-627.

Adams, K. D., Wesnousky, S. G., and Bills, B. G., 1999, Isostatic rebound, active faulting, and potential geomorphic effects in the Lake Lahontan basin, Nevada and California: Geological Society of America Bulletin, v. 111, no. 12, p. 1739-1756.

Anderson, L. W., and Hawkins, F. F., 1984, Recurrent Holocene Strike-Slip Faulting, Pyramid Lake Fault Zone, Western Nevada: Geology, v. 12, no. 11, p. 681-684.

Arrowsmith, J. R., and Zielke, O., 2009, Tectonic geomorphology of the San Andreas Fault zone from high resolution topography: An example from the Cholame segment: Geomorphology, v. 113, no. 1-2, p. 70-81.

Bell, E. J., and Slemmons, D. B., 1979, Recent Crustal Movements in the Central Sierra Nevada Walker Lane Region of California-Nevada .2. Pyramid Lake Right-Slip Fault Zone Segment of the Walker Lane: Tectonophysics, v. 52, no. 1-4, p. 571-583.

Bell, J. W., House, K., and Briggs, R., 2005, Geologic Map of the Nixon Area, Washoe County, Nevada: Nevada Bureau of Mines and Geology.

Bemis, S. P., Micklethwaite, S., Turner, D., James, M. R., Akciz, S., Thiele, S. T., and Bangash, H. A., 2014, Ground-based and UAV-Based photogrammetry: A multi-scale, high-resolution mapping tool for structural geology and paleoseismology: Journal of Structural Geology, v. 69, p. 163-178.

Benson, L. V., and Thompson, R. S., 1987, Lake-Level Variation in the Lahontan Basin for the Past 50,000 Years: Quaternary Research, v. 28, no. 1, p. 69-85.

Bormann, J. M., 2013, New Insights into Strain Accumulation and Release in the Central and Northern Walker Lane, Pacific-North American Plate Boundary, California and Nevada, USA [Doctorate Dissertaion]: Univerist of Nevada, Reno, 150 p.

Briggs, R. W., and Wesnousky, S. G., 2004, Late Pleistocene fault slip rate, earthquake recurrence, and recency of slip along the Pyramid Lake fault zone, northern Walker Lane, United States: Journal of Geophysical Research-Solid Earth, v. 109, no. B8, p. 16.

Briggs, R. W. and Wesnousky S. G., 2005, Late Pleistocene and Holocene paleoearthquake activity of the Olinghouse fault zone, Nevada: Bulletin of the Seismological Society of America, v. 95, no. 4, p. 1301-1313.

Briggs, R. W., Wesnousky, S. G., and Adams, K. D., 2005, Late Pleistocene and late Holocene lake highstands in the Pyramid Lake subbasin of Lake Lahontan, Nevada, USA: Quaternary Research, v. 64, no. 2, p. 257-263.

Bürgmann, R., Pollard, D. D., and Martel, S. J., 1994, Slip distributions on faults: effects of stress gradients, inelastic deformation, heterogeneous host-rock stiffness, and fault interaction: Journal of Structural Geology, v. 16, no. 12, p. 1675-1690.

Eisses, A. K., Kell, A., Kent, G., Driscoll, N., Baskin, R., Smith, K., Karlin, R., Louie, J., and Pullammanappallil, S., 2011, Marine and Land Active-source Seismic Imaging of Mid-Miocene to Holocene-Aged Faulting near

Geothermal Prospects at Pyramid Lake, Nevada: Geothermal Resources Council, v. 35, p. 1643-1646.

Eisses, A. K., Kell, A., Kent, G. M., Driscoll, N. W., Baskin, R. L., Smith, K. D., Karlin, R. E., Louie, J. N., and Pullammanappallil, S. K., 2015, New constraints on fault architecture, slip rates, and strain partitioning beneath Pyramid Lake, Nevada: Geosphere, v. 11, no. 3, p. 683-704.

Fonstad, M. A., Dietrich, J. T., Courville, B. C., Jensen, J. L., and Carbonneau, P. E., 2013, Topographic structure from motion: a new development in photogrammetric measurement: Earth Surface Processes and Landforms, v. 38, no. 4, p. 421-430.

Gold, R. D., Stephenson, W. J., Odum, J. K., Briggs, R. W., Crone, A. J., and Angster, S. J., 2013, Concealed Quaternary strike-slip fault resolved with airborne lidar and seismic reflection: The Grizzly Valley fault system, northern Walker Lane, California: Journal of Geophysical Research-Solid Earth, v. 118, no. 7, p. 3753-3766.

Gold, R. D., Reitman, N. G., Briggs, R. W., Barnhart, W. D., Hayes, G. P., Wilson, E., 2015, On- and off-fault deformation associated with September 2013 Mw 7.7 Balochistan earthquake: Implications for geologic slip rate measurements: Tectonophysics, v. 660, p. 65-78.

Hammond, W. C., Blewitt, G., and Kreemer, C., 2011, Block modeling of crustal deformation of the northern Walker Lane and Basin and Range from GPS velocities: Journal of Geophysical Research-Solid Earth, v. 116, p. 28.

Harwin, S., and Lucieer, A., 2012, Assessing the Accuracy of Georeferenced Point Clouds Produced via Multi-View Stereopsis from Unmanned Aerial Vehicle (UAV) Imagery: Remote Sensing, v. 4, no. 6, p. 1573-1599.

Hunter, L. E., Howle, J. F., Rose, R. S., and Bawden, G. W., 2011, LiDAR-Assisted Identification of an Active Fault near Truckee, California: Bulletin of the Seismological Society of America, v. 101, no. 3, p. 1162-1181.

Johnson, K., Nissen, E., Saripalli, S., Arrowsmith, J. R., McGarey, P., Scharer, K., Williams, P., and Blisniuk, K., 2014, Rapid mapping of ultrafine fault zone topography with structure from motion: Geosphere.

Jónsson, S., Zebker, H., Segall, P., and Amelung, F., 2002, Fault slip distribution of the 1999 Mw 7.1 Hector Mine, California, earthquake, estimated from satellite radar and GPS measurements: Bulletin of the Seismological Society of America, v. 92, no. 4, p. 1377-1389.

Pollefeys, M., Gool, L. V., Vergauwen, M., Verbiest, F., Cornelis, K., Tops, J., and Koch, R., 2004, Visual modeling with a hand-held camera: International Journal of Computer Vision, v. 59, no. 3, p. 207-232.

Reheis, M. C., Adams, K. D., Oviatt, C. G., and Bacon, S. N., 2014, Pluvial lakes in the Great Basin of the western United States—a view from the outcrop: Quaternary Science Reviews, v. 97, p. 33-57.

Reitman, N. G., Bennett, S. E., Gold, R. D., Briggs, R. W., and DuRoss, C. B., 2015, High- Resolution Trench Photomosaics from Image- Based Modeling: Workflow and Error Analysis: Bulletin of the Seismological Society of America.

Sanders, C. O., and Slemmons, D. B., 1996, Geomorphic evidence for Holocene earthquakes in the Olinghouse fault zone, Western Nevada: Bulletin of the Seismological Society of America, v. 86, no. 6, p. 1784-1792.

Snavely, N., Seitz, S. M., and Szeliski, R., 2008, Modeling the world from Internet photo collections: International Journal of Computer Vision, v. 80, no. 2, p. 189-210.

Ullman, S., 1977, Structure From Motion: Journal of the Optical Society of America, v. 67, no. 10, p. 1400-1400.

Ullman, 1979, Interpretation of Structure From Motion: Proceedings of the Royal Society Series B-Biological Sciences, v. 203, no. 1153, p. 405-426.

Wells, D. L., and Coppersmith, K. J., 1994, New Empirical Relationships among Magnitude, Rupture Length, Rupture Width, Rupture Area, and Surface Displacement: Bulletin of the Seismological Society of America, v. 84, no. 4, p. 974-1002.

Wesnousky, S. G., 2008, Displacement and geometrical characteristics of earthquake surface ruptures: Issues and implications for seismic-hazard analysis and the process of earthquake rupture: Bulletin of the Seismological Society of America, v. 98, no. 4, p. 1609-1632.

Wesnousky, S. G., Bormann, J. M., Kreemer, C., Hammond, W. C., and Brune, J. N., 2012, Neotectonics, geodesy, and seismic hazard in the Northern Walker Lane of Western North America: Thirty kilometers of crustal shear and no strike-slip?: Earth and Planetary Science Letters, v. 329, p. 133-140.

Westoby, M. J., Brasington, J., Glasser, N. F., Hambrey, M. J., and Reynolds, J. M., 2012, 'Structure-from-Motion' photogrammetry: A low-cost, effective tool for geoscience applications: Geomorphology, v. 179, p. 300-314.

Zielke, O., Klinger, Y., and Arrowsmith, J. R., 2015, Fault slip and earthquake recurrence along strike-slip faults - Contributions of high-resolution geomorphic data: Tectonophysics, v. 638, p. 43-62.

CHAPTER 2

Late Quaternary Slip Rates for Faults of the Central Walker Lane: Spatiotemporal strain release in a strike-slip fault system

Stephen J. Angster, Steven G. Wesnousky, Paula Figueiredo,

Lewis A. Owen, Sarah Hammer

Abstract

The Walker Lane shear zone trends northwest along the eastern Sierra Nevada and accommodates a significant portion of North American-Pacific Plate relative transform motion. In the central portion of the Walker Lane, a network of Quaternary active strike-slip faults accommodates a significant portion of the geodetically determined ~8 mm/yr of northwest directed transtensional dextral shear measured across the region. Analysis of digital elevation models constructed from lidar and structure from motion modeling of unmanned aerial vehicle photography in conjunction with ^{10}Be and ^{36}Cl cosmogenic, and optically stimulated luminescence dating define preferred minimum late Pleistocene to Holocene strike-slip rates for the Benton Springs, Petrified Springs, Gumdrop Hills, and Indian Head faults in the central Walker Lane of 1.5 ± 0.2, 0.6 ± 0.1, 0.9 $^{+0.3}/_{-0.2}$, and 0.8 ± 0.1 mm/yr, respectively. These strike-slip rates amount to about half of the geodetic strain budget for the central Walker Lane along with seismotectonic scaling relations, reoccurrence intervals for surface rupturing events are expected to be on the order of ~5 ka for each fault. Additional observations from regional along-strike Quaternary mapping of further show that the southern Benton Springs and Indian Head faults have had multiple Holocene ruptures, while the northern Benton Springs, Agai Pah, Gumdrop Hills, and Petrified Springs faults have not, and were limited to surface rupture in the late Pleistocene. The absence of Holocene rupture on these faults suggests that Walker Lane shear strain is released on different spatial and temporal scales,

where slip occurs at different time periods on different faults and fault segments. Implication for this type of behavior lead to less predictable reoccurrence intervals on the individual faults.

Introduction

The Walker Lane is a broad intraplate shear zone that accommodates a significant portion of the relative motion between the North American and Pacific plates (Figure 1**;** Thatcher et al., 1999; Unruh, 2003; Faulds et al., 2005). The region lies between the stable northwest translating Sierra Nevada block and the normal fault bounded ranges of the Basin and Range (Figure 1), and is geodetically defined by northwest-directed transtensional dextral shear (Dokka and Travis, 1990; Thatcher et al., 1999; Hammond et al., 2011). This motion is accommodated by a broad zone of discontinuous faulting (Stewart, 1980) that trends along the eastern Sierra Nevada Mountain front (Figure 1). There are five major and subparallel active northwest trending strike-slip faults that define the northeastern boundary of the central Walker Lane: the Benton Springs (BSF), Petrified Springs (PSF), Gumdrop Hills (GHF), Agai Pah (AF), and Indian Head (IHF) faults (Figure 1). The Walker Lane at this latitude is ~125 km wide and to the west of these strike-slip faults lay a series of primarily normal faults (Figure 1). Together, this fault system is accommodating ~8 mm/yr of contemporary dextral transtensional shear (Hammond et al., 2011; Bormann et al., 2016). Long-term geologic estimates of fault slip rates, and thus the portion of total strain budget

being taken up by the strike-slip faults, is absent to limited (e.g., Wesnousky, 2005a).

In this study, we use digital elevation models (DEMs) constructed from lidar and structure from motion modeling of unmanned aerial vehicle (UAV) photography in conjunction with terrestrial cosmogenic nuclide (TCN) and optically stimulated luminescence (OSL) dating to place probabilistic bounds on the rates of slip for four of the major strike-slip faults. The purpose of this research is to enable comparison of geologic rates of deformation to those observed geodetically and examine the spatiotemporal relationship of slip rates within the strike-slip fault system.

Geologic Background

The Walker Lane is a well-recognized intraplate shear zone that extends from the eastern California shear zone (ECSZ; Figure 1) to the northern end of the Sierra Nevada. The region is composed of northwest trending dextral strike-slip, northeast trending sinistral, and north trending normal faults forming a broad zone of disrupted topography between the Sierra Nevada and Basin and Range (Figure 1). The Walker Lane has been considered to be an incipient plate boundary (Faulds et al., 2005) that is relatively structurally immature in comparison to the main plate boundary to the west comprised by the San Andreas fault system (SA in Figure 1) (Wesnousky, 2005b).

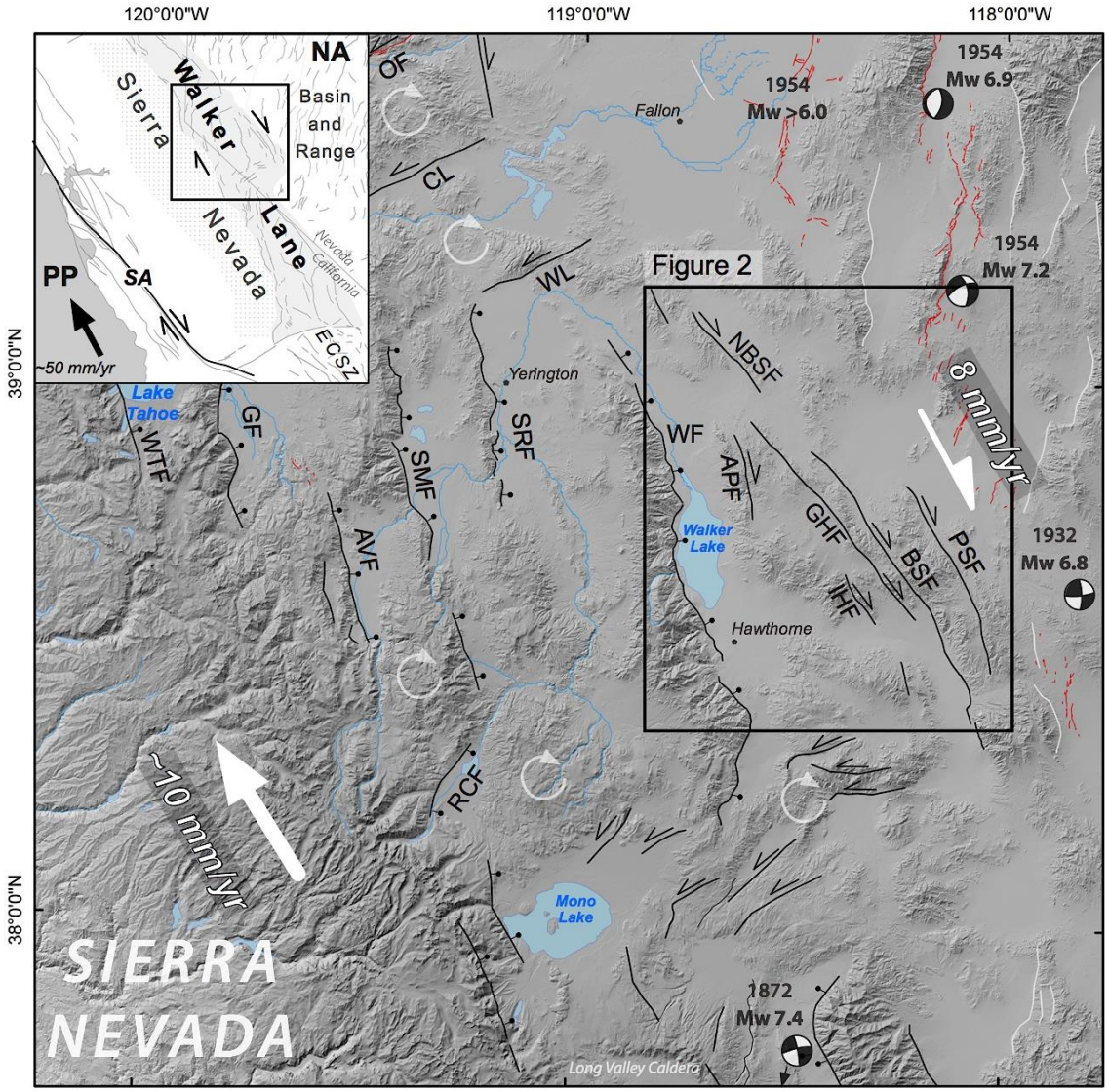

Figure 1. (inset) Regional location of the Walker Lane in relation to the boundary (SA-San Andreas fault) between the Pacific plate (PP) and North American plate (NA). (main) Hillshade image and fault map of the central portion of the Walker Lane. Right-lateral faults of the central Walker Lane and the focus of this study are APF – Agai Pah fault; IHF – Indian Head fault; GHF – Gumdrop Hills fault; (N)BSF – (North) Benton Springs fault; PSF – Petrified Springs fault. Other Quaternary active faults of the Walker Lane shown as black lines (WTF – West Tahoe fault; GF – Genoa fault; AVF – Antelope Valley fault; SMF – Smith Valley fault; WF – Wassuk fault; RCF – Robinson Creek fault; OF – Olinghouse fault; CL – Carson Lineament; WL – Wabuska lineament. Red lines are historic (<150 yr) fault rupture traces with associated focal mechanisms. Faults of the Basin and Range are in grey. Black arrows on faults show sense of motion for strike-slip faults and normal faults are represented by barbells on down dropped side. Transparent white circular arrows show regions undergoing rotation. Solid white arrows show relative motions and rates determined from geodetic studies.

Geodesy shows that the Walker Lane is a distinct zone characterized by elevated strain rates (Kreemer et al., 2012). Analysis of the GPS velocity field shows that the Sierra Nevada translates to the northwest as a rigid block at a rate of ~10 mm/yr with respect to stable North America (Argus and Gordon, 1991), and drives the deformation within the Walker Lane. Geodetic studies constrain the contemporary strain across the Walker Lane from 10 mm/yr in the south to 5-7 mm/yr at its very northern end (Bennett et al., 2003; Hammond et al., 2011). Focal mechanisms and rupture patterns of Historical earthquakes (Figure 1b) have led to the idea that the decrease in strain rate from south to north may be the result of the broadening of the strain field by the transfer of slip from the central portion of the Walker Lane to the Basin and Range (Wesnousky, 2005a).

At the latitude of the central portion of the Walker Lane, geodetic studies place ~8 mm/yr of contemporary northwest directed dextral shear deformation across this region (Figure 1; Bormann et al. 2016). The northwest trending faults of this study lie along the eastern boundary, and lay east of a series of left-stepping normal fault-bounded basins and several zones characterized by clockwise block rotations (Figure 1; Cashman and Fontaine, 2000; Wesnousky et al., 2012; Carlson et al., 2013) that are associated with northeast oriented left-lateral faulting (Figure 1; Wesnousky, 2005a; Li et al., 2017). Prior geologic studies (Wesnousky, 2005a) have provided qualitative geologic slip rate estimates for only the Benton Springs (~1 mm/yr) and Petrified Springs (1.1 to 1.65 mm/yr) faults, using soil chronosequences and standard field techniques.

Recent geodetic block modeling results of Bormann et al. (2016) place contemporary rates of horizontal slip on the faults of this region, that are slightly lower than the geologic rates for these faults. Constraining a long-term rate for each of the faults using modern methods will not only contribute our understanding of slip distribution across the central Walker Lane fault, but may provide additional information to help constrain expected slip budget for the normal faults to the west (Figure 1).

Methods

Quaternary Mapping

We construct a regional Quaternary surficial geologic and fault map to help discern the relative age of the surface faulting on each of the main active strike-slip faults in the central Walker Lane (Figure 2). Formation contacts and fault traces are primarily adapted from the geologic quadrangle maps of Carlson (2014), Ekren and Byers (1985a, 1985b; 1986a, and 1986b), Greene et al. (1991), Hardyman (1980a; 1980b), and from the Quaternary fault and unit maps of Wesnousky (2005a, his Figures 14, 19 and 24), which focus on the southern portions of these faults. We modified fault traces and unit contacts to a scale of ~1:5,000 using topographic based maps and images (e.g., contours, hillshade, and slope shade) derived from newly acquired NCALM airborne lidar datasets (1-meter resolution), acquired along the Benton Springs and Petrified Springs faults.

The extent of the lidar coverage is outlined by the white polygons in Figure 2. The lidar data are publically available from OpenTopography, which includes a report with details on data acquisition, processing, and quality assessment (www.opentopography.org). We rely on analysis of modern ESRI and Google Earth satellite imagery and field mapping when lidar data were not available.

Quaternary alluvial fan formations are correlated across the region and are limited to three units based on unit description in the quadrangle maps and variations in observed surficial characteristics, including: the degree of dissection, elevation above modern stream grade, and tonal and textural differences observed in the field and on imagery and lidar images. The basis for this approach is described by Bull (1991), which has since been applied to various studies in this region (Bell et al., 2004; Wesnousky, 2005a; Koehler and Wesnousky, 2011; Wesnousky and Caffee, 2011) and has been more recently adapted for lidar mapping of alluvial fan deposits (Frankel et al., 2007; Li et al., 2017). The oldest Quaternary alluvial fan deposits (Qfo) are considered to have formed in middle to late Pleistocene, based on the similar subdivision principle of landforms and soil development. These alluvial fans are characterized by deeply incised and well-developed drainage networks that have rounded interfluves that are generally >10 m above modern stream grade. Qfo alluvial fan surfaces commonly have a desert pavement, varnished cobbles composed of sub-rounded to subangular clasts, and have well-developed soils characterized by elevated rubification, a prominent Bt horizon, and approximately stage 3+

carbonate development. In general, these surfaces are predominantly preserved on the up-thrown side of the major faults. Alluvial fan surfaces interpreted to be of intermediate age (Qfi) rest <10 m above modern stream grade and exhibit lesser amounts of dissection. Interfluvial surfaces are more often characterized by relatively broad, smooth, and flat remnants that have moderate soil development, characterized by a B-horizon, some rubification, and stage 2 carbonate development. The youngest fan deposits (Qfy) include the lowest fan surfaces and active channels. These surfaces exhibit bar and swale topography and have minimal soil development, lack a B-horizon, and are considered to be Holocene.

A portion of the study region was once occupied by pluvial Lake Lahontan (e.g., Double Springs flat), which reached its maximum highstand of ~1332 m at ~15.5 ka (Benson and Thompson, 1987; Adams and Wesnousky, 1999) before rapidly desiccating to modern-day Walker Lake (Figure 2). The shoreline for a highstand in Gabbs Valley is not that of Lake Lahontan, but of an ephemeral lake that reached a highstand of 1262 m at about the same time as Lahontan in the late Pleistocene (Ekren and Byers, 1986b). Additional Quaternary units, include playa, distal alluvial fan, aeolian, and fluvial deposits. Bedrock is not shown on the 10-meter hillshade (Figure 2).

Fault traces are mapped based on their expression within the Quaternary deposits. Certain fault traces (solid lines) are those that have geomorphic expression (e.g. scarps or horizontal offsets) within the Quaternary formation that they are mapped (Figure 2). Concealed fault traces (dotted line; Figure 2) are

those covered by deposits that postdate the last surface rupture; thus there is no geomorphic expression of the fault. Inferred fault traces (dashed lines; Figure 2) are mapped where no surficial expression of the fault exists but prior mapping has suggested the location of the fault. Values of prior and newly observed measured horizontal offsets are presented along each fault (Figure 2) for context of rupture characteristics and history. The majority of these observations and measurements are from the figures and maps provided in the Wesnousky (2005a) study. Additional measures of offset along the Benton Springs fault come from Daniel and Langille (2016). New observations of offset from this study are represented by the hollow square boxes in Figure 2.

Detailed mapping of the lidar allows for enhanced assessment of fault activity on the Benton Springs and Petrified Springs faults. On these datasets, we further subdivided the Holocene age alluvial fan units (Qfy) into Qfy1 and Qfy2 to better illustrate Holocene activity (Figure 3). Qfy2 is composed of older elements of Holocene alluvial fans that are higher above the active channels and commonly offset by fault scarps, while Qfy1 are recently active alluvial fan segments that are mantled by the most recently active alluvium and do not have fault scarps traversing them because they have been deposited after the last surface rupturing event. The relative age of Qfy2 is different for each fault, as each fault has a different rupture history.

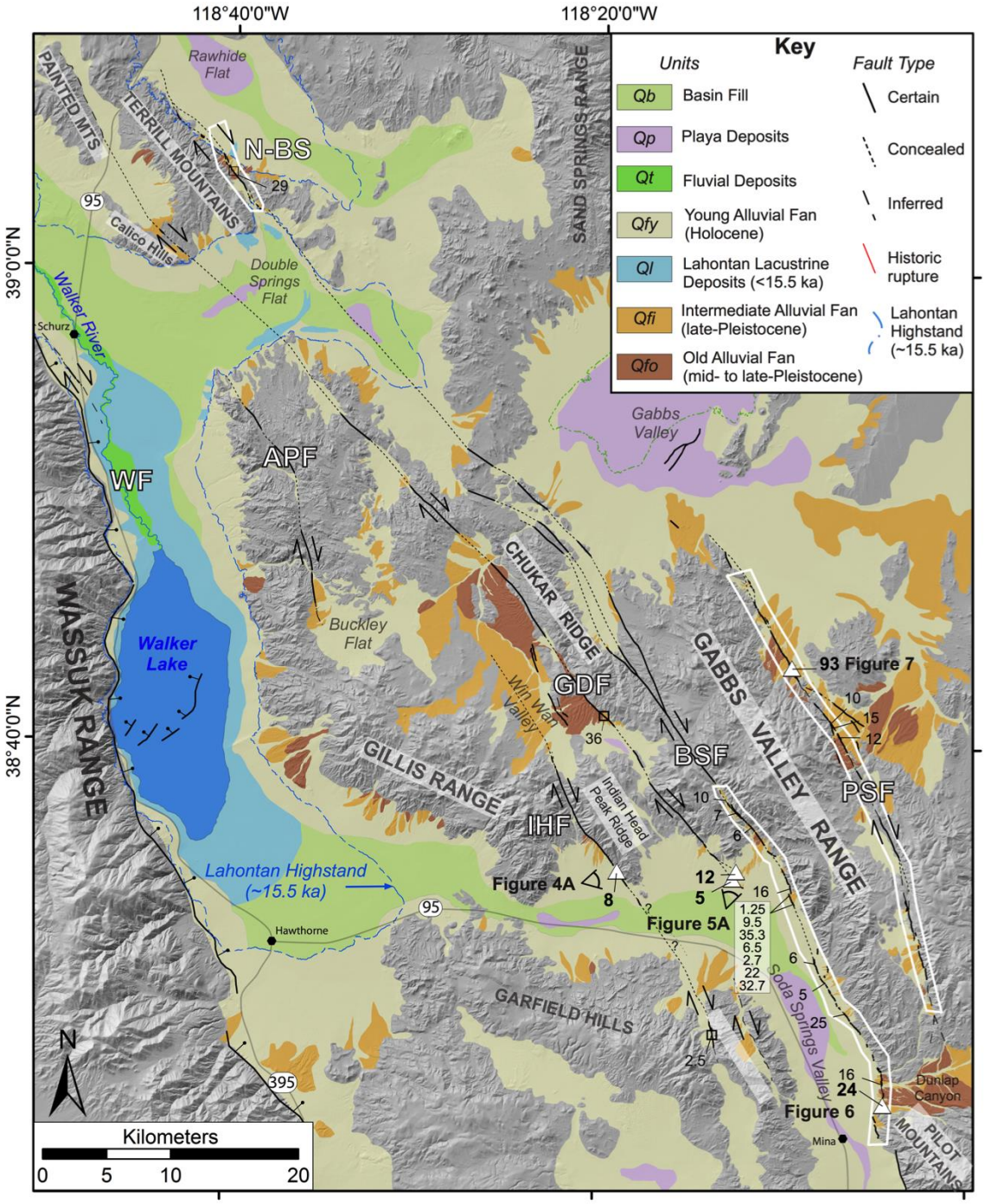

Figure 2. Quaternary unit and fault map of the central Walker Lane region. Quaternary units and fault trace types are shown in key. Bedrock units are transparent over hillshade image. Labeled faults are described in caption of Figure 1. Right-lateral offset values for slip rate site locations (white triangles), other observations (white squares), and those of Wesnousky (2005) are shown by black numbers with leader along each fault and values within white transparent box along BSF are those from Daniel (2016). Outlines of the airborne lidar datasets along the BSF and PSF faults are outlined by solid white line.

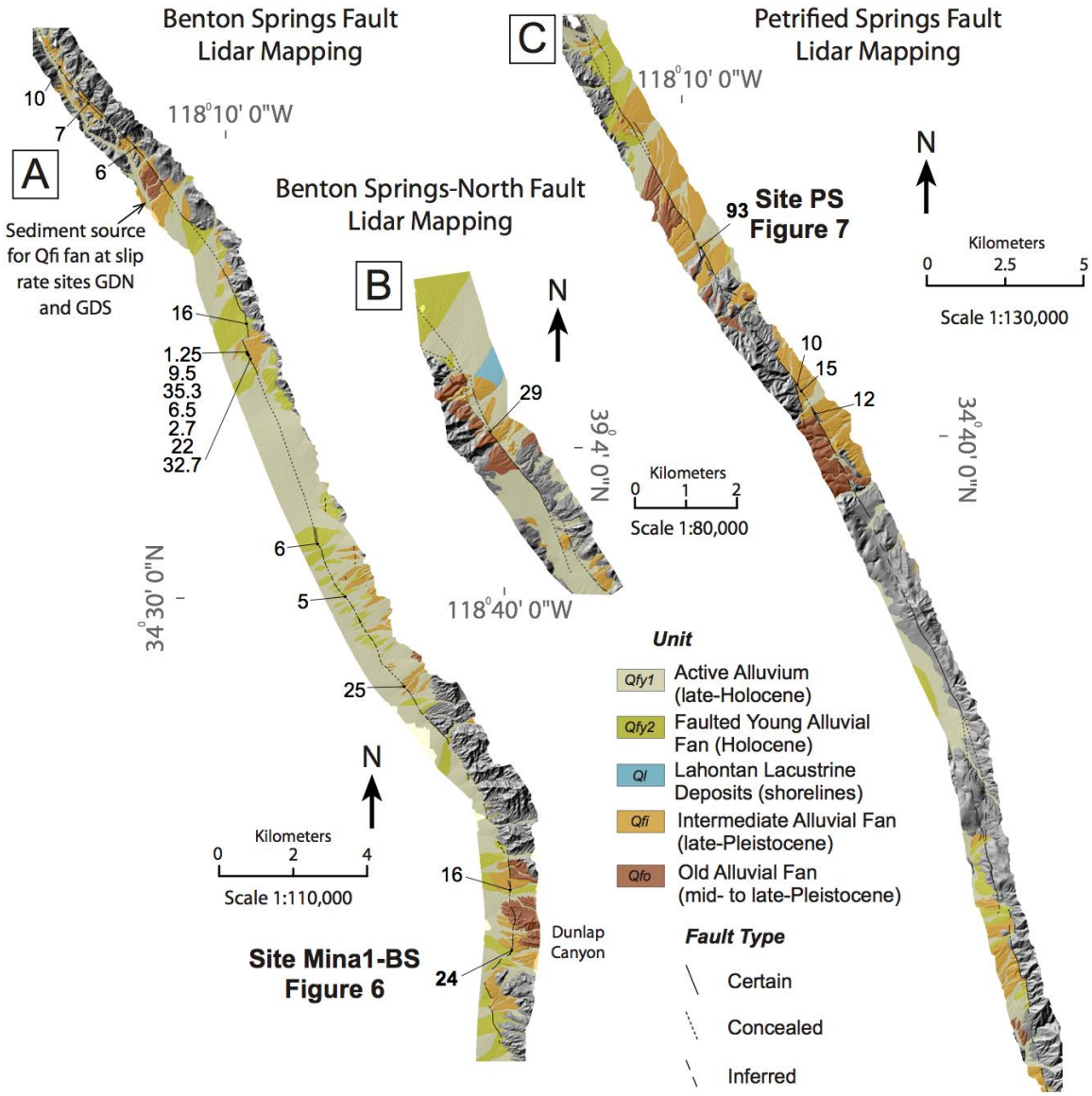

Figure 3. Detailed mapping of airborne lidar data along the Benton Springs and Petrified Springs faults. Unit labels and fault trace explanations are provided in figure and follow description in text.

Slip Rate Sites

We identified individual sites on each strike-slip fault that 1) provided a clear measurable geomorphic offset, 2) whose age could be constrained by dating, and 3) are the result from at least 2 earthquakes so that the slip-rate estimate covers multiple earthquake cycles. Our chosen sites include IH on the Indian Head fault, GDN and GDS on the Gumdrop Hills fault, Mina1-BS on the Benton Springs fault, and PS on the Petrified Springs fault (Figure 2).

The measured horizontal offsets were primarily preserved within alluvial fans deposits, and the risers to these fans serve as key piercing points for horizontal offset measurements. Using such features for offset measurements are inherently prone to higher levels of uncertainty due to variability of lateral erosion on either side of the fault (Cowgill, 2007; Gold et al., 2009). To reduce the amount of uncertainty within our horizontal measurement, we use the lidar datasets and self-produced surface models to obtain probability distribution functions (pdf) of displacement measurements obtained from back-slip reconstructions utilizing the most recent version of LaDiCaoz_v2.1 (Zielke et al., 2015; Haddon et al., 2016). Topographic profiles are drawn across the fan risers on either side of the fault and are back slipped in LaDiCaoz_v2.1 to provide a best-fit displacement. The alluvial fan riser crests, bases, and sometime slopes of the riser are primarily used for the reconstructions. The uncertainties assigned to each measurement are based on the shape of the pdf result from LaDiCaoz, feature distinctiveness, complexity of fault trace, relative obliquity of features,

degree of modification or erosion, quality of topographic dataset, and differences in values between the alluvial fan riser and base. They are subjectively equivalent to 2σ.

Self-produced surface models were developed for the IH, GDS, and GDN slip-rate sites. The models were derived from structure-from-motion (SfM) processing, using *Agisoft Photoscan* software, of aerial photographs obtained from an UAV platform (DJI Phantom 3 Vision+) following the procedures outlined in Johnson et al. (2014) and Angster et al. (2016). The models were georeferenced using the internal GPS of the UAV and then further rectified with measured ground control points using a Trimble R10 GPS receiver with <0.2-m accuracy. In general, the resolutions of the models are <0.5 cm/pix, equivalent to that of the lidar data. Similar to Angster et al. (2016), vegetation filters were not applied to these models due to the limited obstruction from local sagebrush and for the purpose of preserving the true landscaped topography. As a result, local sagebrush in these models appears as irregular oval speckles in the hillshade and slope-shade images. To produce smooth contours that disregard the sagebrush, a smoothing tool was applied to the modeled surface, which averages elevation points using a sliding window algorithm.

Dating Methods

We employ a variety of absolute and relative age dating techniques to constrain the age of the displaced alluvial fan surfaces, including TCN and OSL dating, and soil development.

^{10}Be and ^{36}Cl Dating

TCNs accumulate at a relatively well-known rate (Lal, 1987; Stone, 2000) as a result of the interaction of cosmic rays with certain minerals at the Earth's surface, allowing for the duration of surface exposure to be quantified (Gosse and Phillips, 2001). We used ^{10}Be and ^{36}Cl TCNs depth profiles to mitigate the uncertainty of inheritance (e.g. Gosse and Phillips, 2001) and surface samples.

All depth profile samples were collected within pits excavated within alluvial fan deposits proximal to the measured offsets on each fault (Figure 2). Depth profile pits are named after the slip-rate sites and include IH on the Indian Head fault, GDN and GDS on the Gumdrop Hills fault, Mina1-BS on the Benton Springs fault, and PS on the Petrified Springs fault. Pit locations were chosen carefully at sites where surface deflation appeared to be minimal and where the surfaces appeared most stable. Samples were collected at 30 cm intervals up a vertical profile from a depth of 180 cm to 30 cm. Sediment samples were carefully excavated from a freshly exposed wall within ~10 cm widths and sealed within plastic bags. Where possible, large surface boulders, showing the least evidence of weathering were sampled from the same surfaces as the pits. Approximately 250 g of rock was collected from the uppermost 5 cm of each boulder using a hammer and chisel.

Laboratory processing of sediment and rock samples was performed in the cosmogenic laboratories at the University of Cincinnati following the methods described in Dortch et al. (2009) and Orr et al. (2017) for ^{10}Be and (Stone et al.,

1996) for ^{36}Cl processing. Details of the lab processing and measurement preparation each are described in Appendix A. Processed samples were sent to PRIME Laboratory at Purdue University to be measured by an accelerator mass spectrometer (AMS).

The ^{10}Be profile concentrations were modeled using the calculator of Hidy et al. (2010), which is a depth profile simulator for ^{10}Be that performs Monte Carlo simulations to solve for age, erosion, and inheritance. A value of 1.00 was used for topographic shielding for all samples due to low horizons, sparse vegetation, and rare snow cover at all sites. We used a spallogenic production rate of 4.0 $g^{-1}a^{-1}$ (Lal, 1987; Stone, 2000), assumed an attenuation length of 160 ± 5 g/cm^2, and used an average density of 2.6 g/cm^3. For each ^{10}Be profile, we present concentration vs. depth plots showing the 100,000 profile model simulations and the best-fit profile output from the Hidy et al. (2010) calculator alongside with the probability distribution function graph outputs from the Hidy et al. (2010) calculator of the age, erosion, and inheritance. Parameters used for each depth profile simulation are provided in Table 1.

Cosmogenic ^{36}Cl profile concentrations were modeled using the most recent version of the online CRONUScalc calculator (Marrero et al., 2016), which also performs Monte Carlo simulations to solve for age, erosion, and inheritance. For these profiles we present the concentration vs. depth plots showing the 10,000 profile model simulations and the best-fit profile output from the calculator. Parameters used for each depth profile simulation are provided in Table 2.

Table 1. Summary of ^{10}Be Sample Data

Sample ID	Latitude (dd)	Longitude (dd)	Surface Elevation (m)	Depth (cm)	Grain Size Range (µm)	Quartz Mass (g)	Be Carrier Mass (g)	Corrected ^{10}Be/^{9}Be	^{10}Be Concentration (atoms g^{-1})	Uncertainty (atoms g^{-1})
Mina-30	38.417	-118.075	1485	25-35	250 - 2000	11.2161	0.3491	2.43E-13	5.08E+05	1.3E+04
Mina-60				55-65	250 - 2000	10.6043	0.3535	2.51E-13	5.60E+05	1.1E+04
Mina-90				85-95	250 - 2000	13.2901	0.348	2.67E-13	4.69E+05	9.3E+03
Mina-120				115-125	250 - 2000	14.7377	0.3495	2.73E-13	4.35E+05	9.9E+03
Mina-150				145-155	250 - 2000	10.9321	0.3538	1.91E-13	4.14E+05	1.1E+04
Mina-180				175-185	250 - 2000	7.3808	0.3512	1.15E-13	3.67E+05	1.4E+04
GDS-30	38.574	-118.211	1508	25-35	250 - 500	19.7087	0.3483	3.48E-16	9.43E+05	3.4E+04
GDS-60B				55-65	250 - 500	28.3056	0.3524	3.52E-16	7.09E+05	1.8E+04
GDS-90				85-95	250 - 500	20.6804	0.3502	3.50E-16	7.11E+05	3.1E+04
GDS-150B				145-155	250 - 500	28.3432	0.3517	3.52E-16	3.93E+05	9.6E+03
GDS-180B				175-185	250 - 500	25.6815	0.3527	3.53E-16	3.23E+05	2.1E+04
IH-30	38.579	-118.315	1492	25-35	250 - 500	16.9212	0.3537	3.54E-16	3.73E+05	1.8E+04
IH-60				55-65	250 - 500	19.2633	0.3536	3.54E-16	3.55E+05	1.5E+04
IH-90				85-95	250 - 500	18.5402	0.3506	3.51E-16	4.19E+05	1.5E+04
IH-120				115-125	250 - 500	17.8013	0.3498	3.50E-16	3.62E+05	2.2E+04
IH-150				145-155	250 - 500	18.625	0.3518	3.52E-16	3.97E+05	1.6E+04
IH-180				175-185	250 - 500	18.6489	0.3493	3.49E-16	3.90E+05	2.6E+04

All calculations include a shielding factor of 1

A Be carrier concentration of 1003.8 ppm was used for all

Table 2. Summary of ^{36}Cl sample data

Sample ID	Latitude (dd)	Longitude (dd)	Surface Elevation (m)	Depth (cm)	Grain Size Range (µm)	Leached Rock Mass (g)	Carrier Concentration (ppm)	Carrier Mass (g)	Attenuation Length (g/cm^2)	^{36}Cl Concentration (atoms g^{-1})	Uncertainty (atoms g^{-1})
PSB-1	38.7241	-118.1593	1555	0	125 -250	30.0788	0.971	1.0463	165	6.29E+06	1.68E+05
PSB-2	38.7244	-118.1586	1553	0	125 -250	30.4184	1.567	1.0295	165	6.96E+06	1.47E+05
PSB-3	38.7243	-118.1587	1553	0	125 -250	30.4015	1.567	1.0162	165	4.12E+06	1.08E+05
PSB-4	38.7242	-118.1592	1551	0	125 -250	30.1225	1.567	1.1204	165	9.71E+06	6.91E+05
PSP1-30	38.7241	-118.9593	1557	25-35	125 -250	30.4665	0.971	0.9827	156	1.81E+06	5.56E+04
PSP1-60				55-65	125 -250	30.1986	0.971	0.9844	156	2.43E+06	4.87E+04
PSP1-90				85-95	125 -250	30.1538	0.971	0.9998	156	1.02E+06	3.24E+04
PSP1-120				115-125	125 -250	30.4536	0.971	1.0135	156	9.65E+05	3.42E+04
PSP1-150				145-155	125 -250	30.5505	0.971	0.9689	156	7.25E+05	3.69E+04
PSP1-180				175-185	125 -250	30.3706	0.971	0.9638	156	5.60E+05	2.56E+04
GDS-30	38.5741	-118.2109	1508	25-35	125 -250	30.6848	1.157	30.6848	156	3.07E+06	5.50E+04
GDS-60				55-65	125 -250	31.3547	1.157	31.3547	156	2.70E+06	7.54E+04
GDS-90				85-95	125 -250	32.5048	1.157	32.5048	156	2.65E+06	1.14E+05
GDS-120				115-125	125 -250	30.8196	1.157	30.8196	156	1.86E+06	6.05E+04
GDS-150				145-155	125 -250	30.857	1.157	30.857	156	1.23E+06	6.01E+04
GDS-180				175-185	125 -250	32.0931	1.157	32.0931	156	8.88E+05	4.22E+04
GDN-30	38.5798	-118.2079	1536	25-35	125 -250	31.9789	1.567	31.9789	156	2.12E+06	5.61E+04
GDN-60				55-65	125 -250	30.6453	1.567	30.6453	156	2.15E+06	3.86E+04
GDN-90				85-95	125 -250	31.9098	1.567	31.9098	156	1.43E+06	2.50E+04
GDN-120				115-125	125 -250	30.5637	1.567	30.5637	156	1.20E+06	4.18E+04
GDN-150				145-155	125 -250	31.2176	1.567	31.2176	156	1.09E+06	2.81E+04
GDN-180				175-185	125 -250	30.5852	1.567	30.5852	156	7.69E+05	3.29E+04

All calculations include a shielding factor of 1

Table 2 cont.

SiO_2 (%)	TiO_2 (%)	Al_2O_3 (%)	Fe_2O_3 (%)	MnO (%)	MgO (%)	CaO (%)	Na_2O (%)	K_2O (%)	P_2O_5 (%)	Analytical Water (%)	CO_2 (%)	Cl ppm	B ppm	Sm ppm	Gd ppm	U ppm	Th ppm	Cr ppm	Li ppm
56.12	0.84	18.25	8.11	0.14	2.64	7.15	3.86	1.40	0.14	0.50	0.50	410.37	9.34	2.44	2.33	1.10	2.60	14.12	0.00
55.46	0.85	17.84	8.75	0.13	3.08	7.11	3.85	1.52	0.13	0.45	0.45	156.33	1.41	2.85	2.70	1.10	3.10	14.12	0.00
50.77	1.36	17.21	9.35	0.16	3.44	7.33	3.59	2.08	0.99	1.60	1.60	234.29	4.96	8.95	6.84	1.20	3.60	49.44	0.00
54.31	0.87	17.73	8.84	0.15	3.78	7.25	3.61	1.21	0.16	0.85	0.85	230.53	18.61	4.19	3.56	1.20	2.70	14.12	0.00
0.63	14.71	6.15	0.07	2.27	2.47	2.41	2.51	0.12	4.30	4.30	96.25	37.00	3.10	2.46	2.70	9.00	0.01	0.00	
61.23	0.63	14.15	5.80	0.09	1.61	4.68	2.99	2.48	0.21	2.95	2.95	182.41	30.00	3.55	2.85	3.70	8.20	0.01	0.00
62.64	0.61	14.44	5.46	0.06	1.13	4.20	3.20	2.57	0.06	2.70	2.70	83.10	28.00	2.25	1.78	2.30	6.80	0.00	0.00
63.38	0.56	14.52	4.82	0.06	1.07	3.56	3.00	2.64	0.07	3.05	3.05	89.56	30.00	2.45	2.03	2.70	7.40	0.00	0.00
62.38	0.74	15.20	6.69	0.10	1.46	3.49	3.33	2.47	0.06	1.90	1.90	95.73	25.00	2.46	2.28	2.10	7.00	0.00	0.00
58.50	0.75	12.87	7.09	0.07	1.29	5.94	2.91	2.19	0.04	4.05	4.05	71.69	20.00	2.20	1.71	1.80	5.50	0.01	0.00
72.72	0.25	13.59	2.07	0.02	0.29	0.61	2.43	4.64	0.03	1.60	1.60	147.25	40.00	2.51	1.94	4.00	11.20	0.00	0.00
72.98	0.26	13.39	2.07	0.01	0.28	0.56	2.41	4.57	0.04	1.65	1.65	153.65	46.00	2.43	1.91	3.90	10.30	0.00	0.00
73.95	0.17	13.21	1.54	0.01	0.17	0.63	2.56	5.28	0.02	1.15	1.15	242.79	42.00	1.63	1.44	2.60	11.10	0.00	0.00
68.51	0.24	12.63	1.85	0.01	0.30	2.99	2.41	4.21	0.03	3.35	3.35	164.94	33.00	2.12	1.68	3.10	10.00	0.00	0.00
72.88	0.32	13.30	2.27	0.01	0.32	0.57	2.26	3.97	0.05	1.90	1.90	101.04	51.00	2.41	1.95	3.70	9.60	0.00	0.00
0.35	13.30	2.18	0.01	0.27	0.54	2.29	3.72	0.05	2.00	2.00	89.67	42.00	2.38	1.86	3.80	11.20	0.00	0.00	
73.75	0.28	12.93	2.25	0.02	0.30	0.55	2.13	3.76	0.04	1.90	1.90	88.57	36.00	2.61	2.08	3.80	10.40	0.00	0.00
73.74	0.27	13.22	2.18	0.01	0.35	0.50	2.32	4.26	0.04	1.45	1.45	127.57	37.00	2.42	1.88	3.70	10.20	0.00	0.00
74.62	0.26	12.56	2.05	0.01	0.26	0.46	2.11	4.06	0.04	1.70	1.70	98.32	32.00	2.31	1.84	3.40	5.90	0.00	0.00
74.86	0.27	12.83	1.67	0.01	0.24	0.45	2.27	4.28	0.03	1.45	1.45	107.99	30.00	2.37	1.86	3.60	8.80	0.00	0.00
74.13	0.28	12.89	2.00	0.01	0.26	0.50	2.17	4.23	0.04	1.65	1.65	114.67	30.00	2.36	1.76	3.30	10.10	0.00	0.00
72.56	0.30	13.26	2.02	0.01	0.32	0.59	2.25	4.13	0.05	2.15	2.15	97.50	39.00	2.39	1.90	3.50	9.70	0.00	0.00

Bulk rock weight % uncertainties equal to 0.01%
Bulk rock ppm uncertainties equal to 0.10

Table 2 cont.

Target K_2O %	Target CaO %	Target TiO_2 %	Target Fe_2O_3 %	Target Cl ppm	Uncertainty Cl ppm
NaN	NaN	NaN	NaN	NaN	9.34
NaN	NaN	NaN	NaN	NaN	1.41
NaN	NaN	NaN	NaN	NaN	4.96
NaN	NaN	NaN	NaN	NaN	18.61
2.51	2.47	0.63	6.15	96.25	1.39
2.48	4.68	0.63	5.80	182.41	1.84
2.57	4.20	0.61	5.46	83.10	0.69
2.64	3.56	0.56	4.82	89.56	3.65
2.47	3.49	0.74	6.69	95.73	3.42
2.19	5.94	0.75	7.09	71.69	3.64
4.64	0.61	0.25	2.07	147.25	0.89
4.57	0.56	0.26	2.07	153.65	3.27
5.28	0.63	0.17	1.54	242.79	5.36
4.21	2.99	0.24	1.85	164.94	4.95
3.97	0.57	0.32	2.27	101.04	3.28
3.72	0.54	0.35	2.18	89.67	5.37
3.76	0.55	0.28	2.25	88.57	1.66
4.26	0.50	0.27	2.18	127.57	0.65
4.06	0.46	0.26	2.05	98.32	0.84
4.28	0.45	0.27	1.67	107.99	2.01
4.23	0.50	0.28	2.00	114.67	0.75
4.13	0.59	0.30	2.02	97.50	2.59

Target rock ppm uncertainties equal to 0.010

The ^{36}Cl exposure ages of the surface boulder samples are also calculated using the most recent online version of CRONUScalc (Marrero et al., 2016). Input parameters for CRONUScalc are provided in Table 2. We use the minimum and maximum age results for each boulder using the scaling schemes of Lifton-Sato (Lifton et al., 2014) and Lal-Stone (Lal, 1987; Stone, 2000) to represent the exposure ages of the boulders.

OSL sampling, processing, and dating

An OSL sample was collected where possible by hammering an opaque ~20cm long plastic tube into the center of a freshly cleaned face of a well-sorted sand lens. The tube was packed tight, taped, sealed, and later processed and measured in the Luminescence Dating Laboratory at the University of Cincinnati. OSL sample were prepared following the methods described in Counts et al. (2015) and in detail in Appendix A. An unbiased selection of the sample was sent to Actlab for chemical analysis of U, Th, and K concentrations following the procedure described in Snyder and Duval (2003) for dose rate determinations. An automated Risø TL-DA-20 OSL reader was used for the OSL measurements and irradiation. Thirty-two aliquots were measured for equivalent doses on an automated Risø TL-DA-20 OSL reader using the single aliquot regeneration (SAR) method of Murray and Wintle (2000). RadialPlotter of Verneesch (2009) was used to help determine statistically significant peaks within the dose equivalent measurements.

Soil Development

We describe the soils exposed in each cosmogenic profile pit following the techniques and terminology described by Birkeland (1984) and Soil Survey Division of Staff (1993), and sampled each soil horizon for texture analysis. Texture samples were sent to A&L Great Lakes Laboratory for particle size analysis.

Details of Study Sites

Details of Quaternary fault expression are described here from north to south along each fault (Figures 2 and 3). Each is followed by a site description of the slip rate site and measures of offset.

Agai Pah Fault

The Quaternary trace of the Agai Pah fault (APF; Figure 2) extends for ~20 km and begins within the eastern portion of Buckley Flat. Here the fault trace is expressed as a faint linear scarp within late Pleistocene (Qfi) alluvial fans and is completely concealed by Holocene alluvial fan deposits (Qfy) (Figure 2). Further to the northwest, the fault is predominantly mapped within the bedrock units of the Gillis Range (Hardyman, 1980a). The fault remains concealed by the Holocene units within Double Springs Flat and may terminate somewhere to the northwest. The absence of expression of the fault within Holocene units suggests that there has not been a surface-rupturing event on this fault during the

Holocene. Due to the limited expression of this fault, we were unable to find a suitable slip-rate site.

Indian Head Fault

The trace of the Indian Head fault follows the western base of Indian Head Peak ridge, on the northern side of Soda Springs Valley (Figure 2). The fault bounds the contact between bedrock and the steep active alluvial fans emanating from the canyons and the fault is absent within the most recently active alluvium, but occasionally forms southwest facing fault scarps within remnants of older Holocene alluvial fans elements (Figure 2). Older (Qfi and Qfo) alluvial fan elements are limited to the northern portion of this stretch of fault where the trace does not form scarps within Qfo and Qfi alluvial fan units. To the northwest, the fault trace is confined to bedrock in the Gillis Range (Ekren and Byers, 1985d) and continues northward into Win Wan Valley (Figure 2) where the fault trace is concealed by Holocene alluvial fans. Further to the northwest, expression of the fault is absent within a large incised Qfi alluvial fan within the Win Wan Valley (Figure 2), suggesting that the fault either ends before it reaches the Qfi alluvial fan or has not ruptured since the deposition of that fan.

South of Highway 95 (Figure 2) and along strike of the Indian Head fault, an active fault trace trends along the western flank of the Black Dyke Mountains (Figure 2**)**. The fault is mostly confined along the linear base of the mountain front and occasionally forms subtle (<0.5 meter) west facing fault scarps within older elements of Qfy. At one of the canyon outlets, a channel riser is right

laterally offset by 2.5 m (Figure 2). An exposure of the southern channel wall reveals a poorly developed soil within Qfy2, characterized by a very thin Av cap over a very weak to absent Bw horizon (IH-south in Table A1), with the upper 10 cm of a poorly sorted angular pebble–cobble conglomerate. The weak soil development suggests that Qfy2 formed during the Holocene. Whether the offset is the result of single or multiple earthquakes during the Holocene is unclear. The expression of this southern fault strand is similar to the observed strand along Indian Head Peak ridge. No fault trace is evident in Soda Springs Valley between Black Dyke Mountain and Indian Head Peak Ridge. The fault is likely continuous but is concealed beneath the active alluvium and basin deposits within Soda Springs Valley. In summary, the Indian Head fault trace exhibits Holocene rupture that produced measurable geomorphic offsets within Holocene alluvial fan and the southern extent of the fault may continue farther southward beyond where previously mapped, extending to a total length of ~40 km.

Slip Rate Site

At the southern end of Indian Head Peak a Qfy2 fan is preserved near the outlet of a small steep canyon (Figure 4a). The fan surface sits ~1.5 m above the active drainage and is characterized by muted bar and swale topography that is mantled by angular metasedimentary gravel and scattered small angular boulders. The fault forms a ~1 m-high southwest facing fault scarp near the bedrock contact and right-laterally offsets the southern riser of the alluvial fan, which is mapped on either side of the fault (Figure 4b). The riser crest and base

are offset 7.6 and 8.3 m, respectively (Figure 4b and c). These values are similar in magnitude and suggest that the offset accumulated sometime after the deposition and incision of Qfy2 and provide an average lateral displacement of 8 ± 0.4 m.

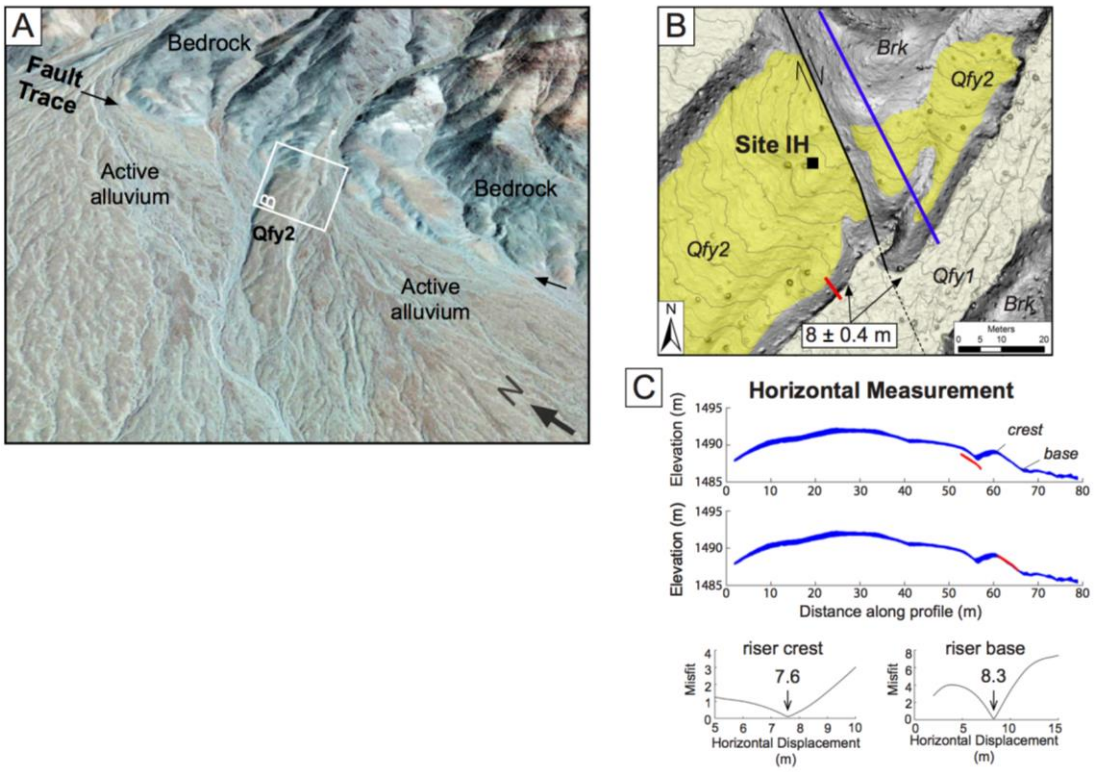

Figure 4. Indian Head fault slip rate site (see Figure 2 for location). A) Oblique view (looking northeast) of offset Qfy2 fan. B) Detailed geologic map over SfM slope shade image and 0.5 m contours of measured offset. Blue and red lines correspond to topographic profiles used for LaDiCaoz reconstructions shown in part (C). C) Horizontal reconstructions of topographic profiles. Lower plots show probability distribution functions and best fit of the reconstructions using the riser crest and base.

Gumdrop Hills Fault

The visible trace of the Gumdrop Hills fault strikes northwest for a distance of ~70 km from Soda Springs Valley (Figure 2). At the northern end of Soda Springs Valley, the fault is expressed intermittently within the distal portion of a dissected Qfi alluvial fan. The fault is concealed beneath Holocene alluvium and emerges along a bedrock-alluvial contact before cutting through the bedrock of the of the eastern Gabbs Valley Range (Ekren and Byers, 1986a). Within Win Wan Valley, the fault is expressed within Qfo and Qfy alluvial fans shedding from Chukar Ridge (Figure 2). A new offset of a right-laterally displaced fan riser, measuring ~36 m, is evident as the fault rises higher on these alluvial fan, and is manifested within a proximal Qfi alluvial fan composed of very coarse volcanic clasts. The fault continues along the western base of Chukar Ridge, occasionally crossing small alluvial filled basins and is concealed by Holocene (Qfy) and intermediate age (Qfi) alluvial fans. Evidence of the Gumdrop Hills fault is absent in Double Springs Flat, which is encircled by pluvial Lake Lahontan (~15.5 ka) shoreline features and filled by Holocene playa and basin fill deposits (Figure 2). Carlson (2014) maps the northern extension of the Gumdrop Hills fault north of Double Springs Flat as multiple discontinuous strands within the bedrock units of the Calico Hills. The trace does not break Holocene deposits on the northern flank of the Calico hills, and Carlson (2014) maps an inferred trace of the fault for another ~10 km to the northern end of the Painted Mountains (Figure 2).

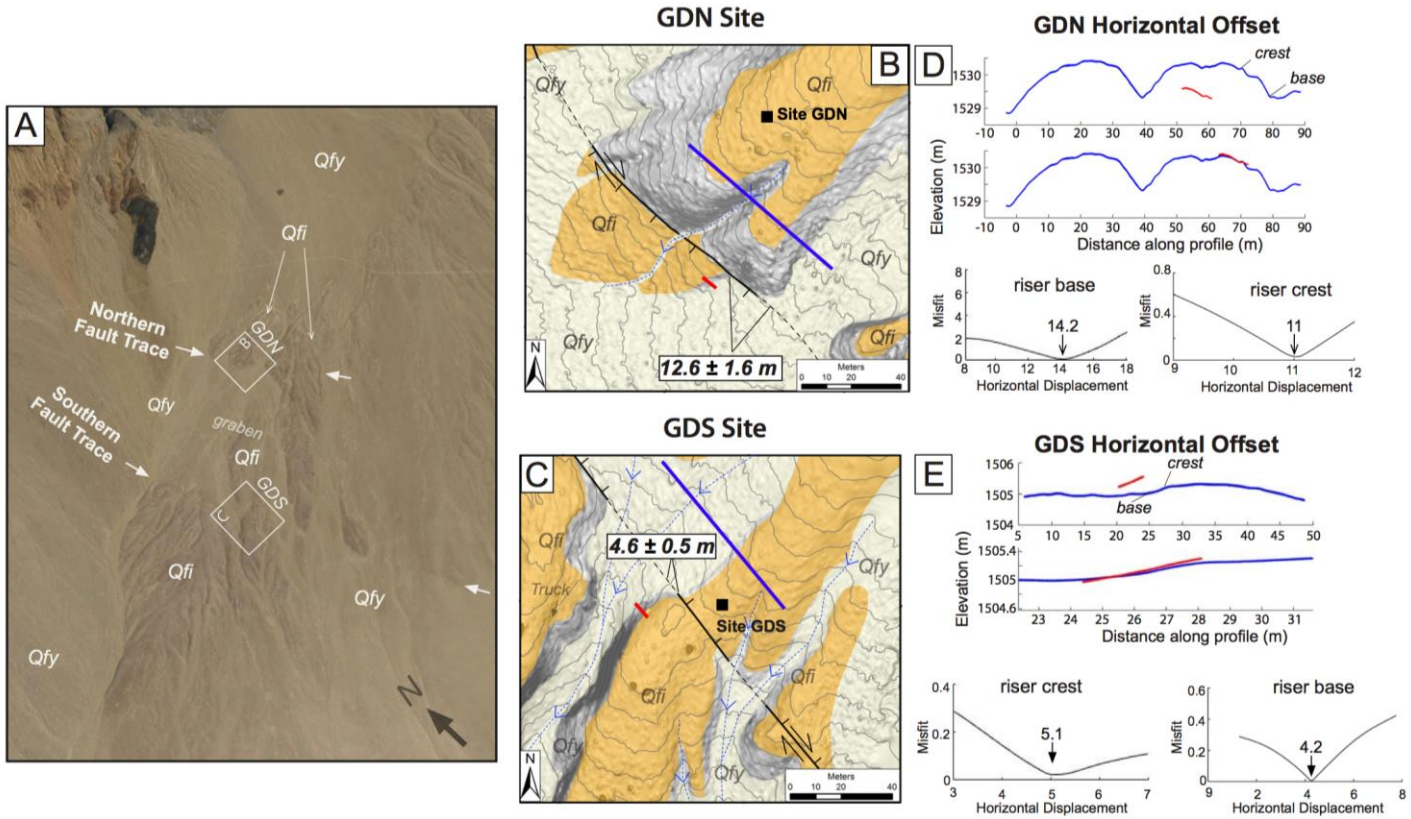

Figure 5. Gumdrop Hills fault slip rate sites GDN and GDS (please see Figure 2 for location). A) Oblique view (looking northeast) of offset distal Qfi fan unit from ESRI satellite imagery. B) and C) Detailed geologic maps over SfM slope shade images and 0.5 m contours showing measured offsets. Location of GDN and GDS ^{10}Be and ^{36}Cl cosmogenic pit shown by black squares. Blue and red lines correspond to topographic profiles used for LaDiCaoz reconstructions shown in parts C and E. C) and E) Horizontal reconstructions of topographic profiles shown by the red and blue lines in geologic maps. Lower plots show probability distribution functions and best-fit for the reconstructions using the riser crest and base.

In summary, the Gumdrop Hills fault is limited to expression within Qfi alluvial fans in the southern portion and further limited to bedrock expression at the north end, where it is concealed by Qfi. The lack of expression within Holocene units, especially within the Lahontan shoreline features in Double Springs Flat (Figure 2), suggests that the Gumdrop Hills fault has not ruptured during the Holocene, with the most recent rupture possible focused at the southern end.

Slip Rate Site

The fault splays into two subparallel fault traces forming a graben within the distal Qfi alluvial fan deposits at the southern end of the Gumdrop Hills fault (Figure 5a). The Qfi alluvial fan of which the fault is manifested in is sourced from a relatively large canyon to the northeast containing older fan units (Figure 2 and 3a). On the northern fault strand (site GDN; Figure 5a), the fault exhibits a ~3-m high southeast facing fault scarp within the Qfi fan (Figure 5b). Displacement of the southeastern riser records 11 and 14.2 m of right-lateral displacement of the crest and base of the riser, respectively (Figure 5b and d). We use the average of the two measurements (12.6 ± 2 m) to represent the amount of accrued displacement since abandonment of the alluvial fan surface. The southern fault strand, at site GDS (Figure 5a**),** forms a ~0.5 m uphill northeast facing scarp within the same Qfi alluvial fan (Figure 5c). Displacement of the base and crest of the northwest alluvial fan riser records 4.2 and 5.1 m of right-lateral offset, respectively (Figure 5e). The average (4.5 ± 0.5 m) is also assumed to have

accrued since abandonment of the alluvial fan surface. The offset measurements along the north and south strands sum to a cumulative displacement of 17.1 ± 2.5 m.

Benton Springs Fault

The 100-km-long Benton Springs fault strikes northwest from the southern end of the Soda Springs Valley. The fault is bounded by the western flank of the Pilot Mountains at the southern end of the Soda Spring valley (Figure 2) and displays mostly vertical offset. To the north, the fault appears within the lidar data as a southwest-facing scarp within Holocene (Qfy2) alluvial fans as it crosses the large drainage outlet of Dunlap Canyon and progressively displaces a series of Qfo and Qfi formations (Figure 3a). The fault continues along the western base of the Gabbs Valley Range and occasionally splays into the younger alluvium within Soda Springs Valley, where it forms small (<0.5 m) scarps within Holocene Qfy2 alluvial fans (Figure 3a). There are multiple smaller measured offsets, ranging from 2.7 to 6 m, within Qfy2 alluvial fans (Figure 3a) providing evidence for multiple Holocene ruptures. Larger magnitude offsets (10 – 36 m) are evident within Qfi alluvial fans along this stretch of the fault (Figure 3a). At the northeastern end of Soda Springs Valley, the fault enters a long linear canyon forming uphill facing scarps within smaller Qfi and Qfo fans and trends along small bedrock ridges within the canyon (Figure 3a). Larger offsets (>5 m) are present in this canyon within Qfi. The fault continues northwestward through the bedrock units of the Gabbs Valley Range (Ekren and Byers, 1986a) where it

splays into multiple fault strands. The fault traces are concealed by Holocene (Qfy) alluvial fans on the other side of the bedrock (Figure 2). No Quaternary trace has been identified in these Holocene alluvial fans, thus supporting the prior mapping (Ekren and Byers, 1986b). The fault bends to the left before entering Double Springs Flat, and remains concealed beneath Holocene deposits including Qfy, Qb, and Qp units. Along the northwestern corner of Double Springs flat, the fault parallels the Lahontan highstand (15.5 ka) and shoreline features, which do not appear to be offset where they curve to the west and intersect the fault trace (Figure 2). The fault trace reappears near the southern end of the Terrill Mountains within Qfi alluvial fan deposits and continues along the eastern flank expressed solely within Qfi and Qfo (Figure 3b). Analysis of the northern most lidar dataset (Figure 2), confirms a ~29 m right-lateral offset channel margin of a Qfi fan observed by Carlson (2017)(Figure 3b). The trace remains concealed by Holocene alluvial fan at the northern end of the Terrill Mountains and does not appear to offset shorelines within Rawhide Flat (Figure 2).

In summary, the fault exhibits Holocene displacement, marked by various measured of offsets within Qfy2 alluvial fans within Soda Springs Valley. In the valleys, flats, and along the slopes of the ranges to the north, there is no evidence of Holocene age ruptures; rather expression of the fault is limited to late Pleistocene alluvial fans (Qfi and Qfo), suggesting that this portion of the fault has not ruptured during the Holocene.

Slip Rate Site

Near the southern end of the Benton Springs fault, the fault crosses the outlet of Dunlap Canyon and displaces a series of Qfo, Qfi, and Qfy2 alluvial fans (Figure 6a). On the north side of the canyon outlet, the fault forms a ~2 m fault scarp within a Qfi fan (Figure 6b) and displaces the southern riser crest, slope, and base by 36 m, 34.2 m, and 33 m, respectively (Figure 6c). The constancy between the measurements provides a robust offset measurement and suggests that the displacement, averaging 34.5 ± 1.5 m, occurred sometime after abandonment and incision of the Qfi alluvial fan.

Petrified Springs Fault

The Petrified Springs fault is the eastern most fault of the central Walker Lane. Trending north-northwest for ~45 km, the fault starts just north of Dunlap Canyon, where prior mapping (Ekren and Byers, 1985a) places the fault through the bedrock in the southern portion of the Gabbs Valley Range (Figure 2). The Quaternary trace of the fault, just to the north, is in an elevated valley within the Gabbs Valley Range mostly along the bedrock alluvial contact (Figure 2). Here, the fault occasionally forms east and west facing subtle (<0.5 m) discontinuous fault scarps within Qfi fans but is concealed by Holocene alluvial fans as it crosses multiple drainage outlets (Figure 3c). Further to the north, the fault bends slightly to the west and is confined to the bedrock. The Quaternary trace of the fault reemerges along the eastern flank of the Gabbs Valley Range where it displaces large older (Qfi and Qfo) alluvial fans, forming a predominantly uphill

(west) facing fault scarp. Multiple larger magnitude (>10 m) horizontal offsets are present along this stretch that are mostly preserved as offset drainages channels (Figure 3c). To the northwest, the range-front steps west and the fault trace cuts across more distal parts of Qfi and Qfo alluvial fans. The fault is very linear and defined by shutter ridges, closed depressions, beheaded channels, and is expressed dominantly as a northeast-facing scarp within Qfi alluvial fans and bounds the eastern edge of Qfo alluvial fans (Figure 3c). At the northern end of this stretch, and at the northern end of the lidar dataset, the fault is covered by multiple Holocene alluvial fans and remains concealed fan (Figure 3c). As the range steps back to the right, the trace of the fault is concealed beneath the colluvium of steep eastern slope of the northern end of the Gabbs Valley Range (Ekren and Byers, 1986b). The final expression of the Petrified Springs fault is marked by a southwest facing fault scarp within a Qfi alluvial fan that extends into Gabbs valley (Figure 2). Ekren and Byers (1986b) identify northeast tending fault scarps within the playa deposits in Gabbs Valley (Figure 2), but trend perpendicular to the rest of the fault trace and are like not that of the Petrified Springs fault.

In summary, there is no evidence of Holocene rupture along the Petrified Springs fault. The multiple larger (>10 meter) offsets, however, show that the Petrified Springs fault was active during the Pleistocene.

Slip Rate Site

On the south side of Gabbs Valley, where the fault crosses more distal portions of alluvial fans, there is a beheaded channel incised into a Qfi alluvial fan and lies in front of a large fault scarp below a high Qfo fan surface (Figure 7a). The slopes of this high pediment surface are composed of bedrock. Reconstruction of the base and the crest of the southern channel margin of the beheaded channel to the northern prow end of the bedrock shutter ridge yield offset measurements of 92 and 93 m, respectively (Figure 7c). The values are relatively consistent and we determine an average offset of 92.5 ± 0.5 m for this site. A secondary fault splay is present to the west that appears to displace other Qfi alluvial fan units as well as form northeast facing fault scarps within the high Qfo surface adjacent to the beheaded channel (white arrows Figure 7a). No lateral measurement of offset could be determined within this surface due to the presence of this secondary fault splay; our offset measurement of the beheaded channel is thus representative of a minimum.

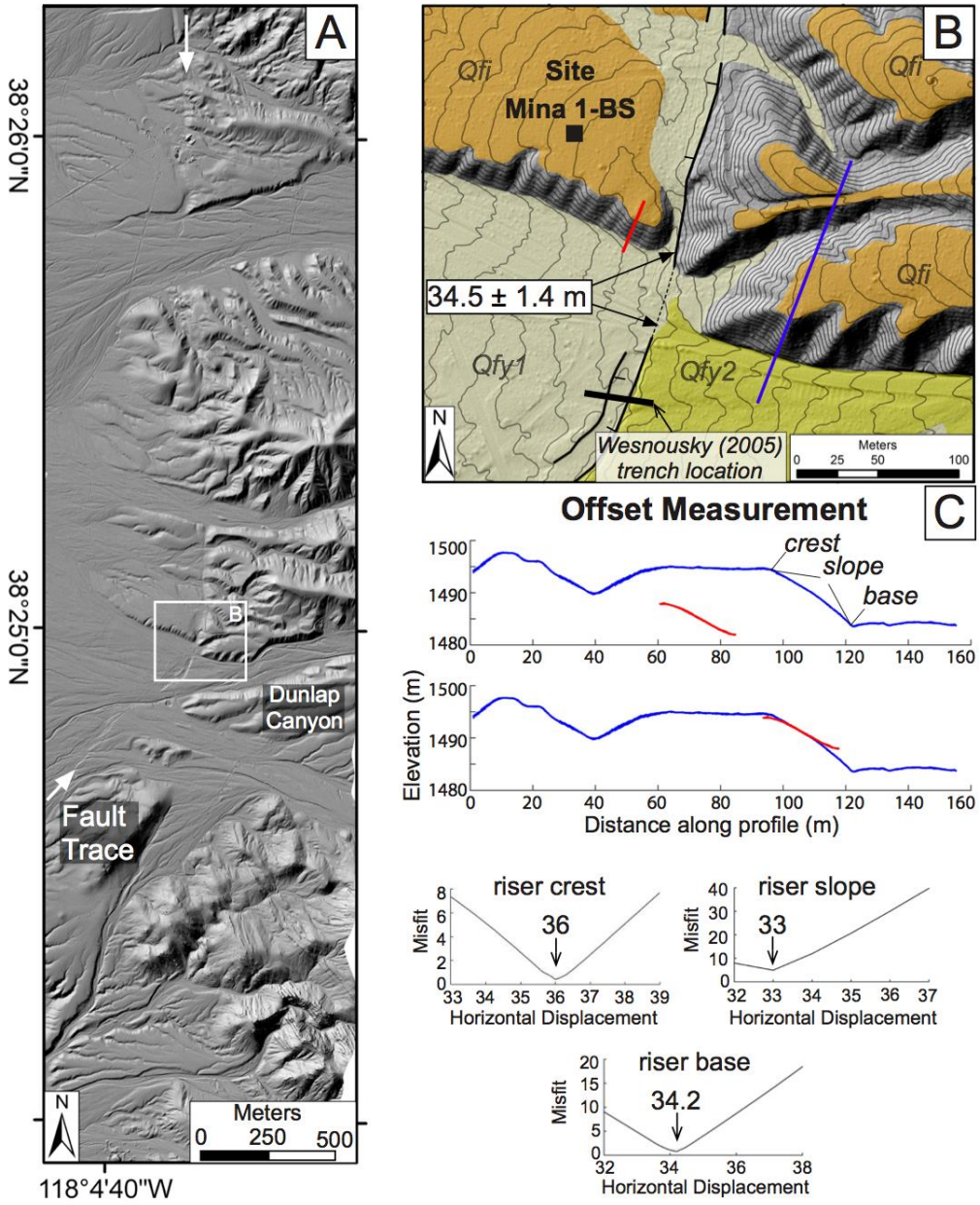

Figure 6. Benton Springs fault slip rate site (please see Figure 2 for location). A) Hillshade image of lidar data over southern portion of Benton Springs fault. B) Detailed geologic map within 0.5 m contour intervals. Location of Mina 1-BS ^{10}Be cosmogenic pit shown by the black square. Blue and red lines correspond to topographic profiles used for LaDiCaoz reconstructions shown in part (C). C) Horizontal reconstructions of topographic profiles. Lower plots show probability distribution functions and best fit of the reconstructions using the riser crest, slope, and base.

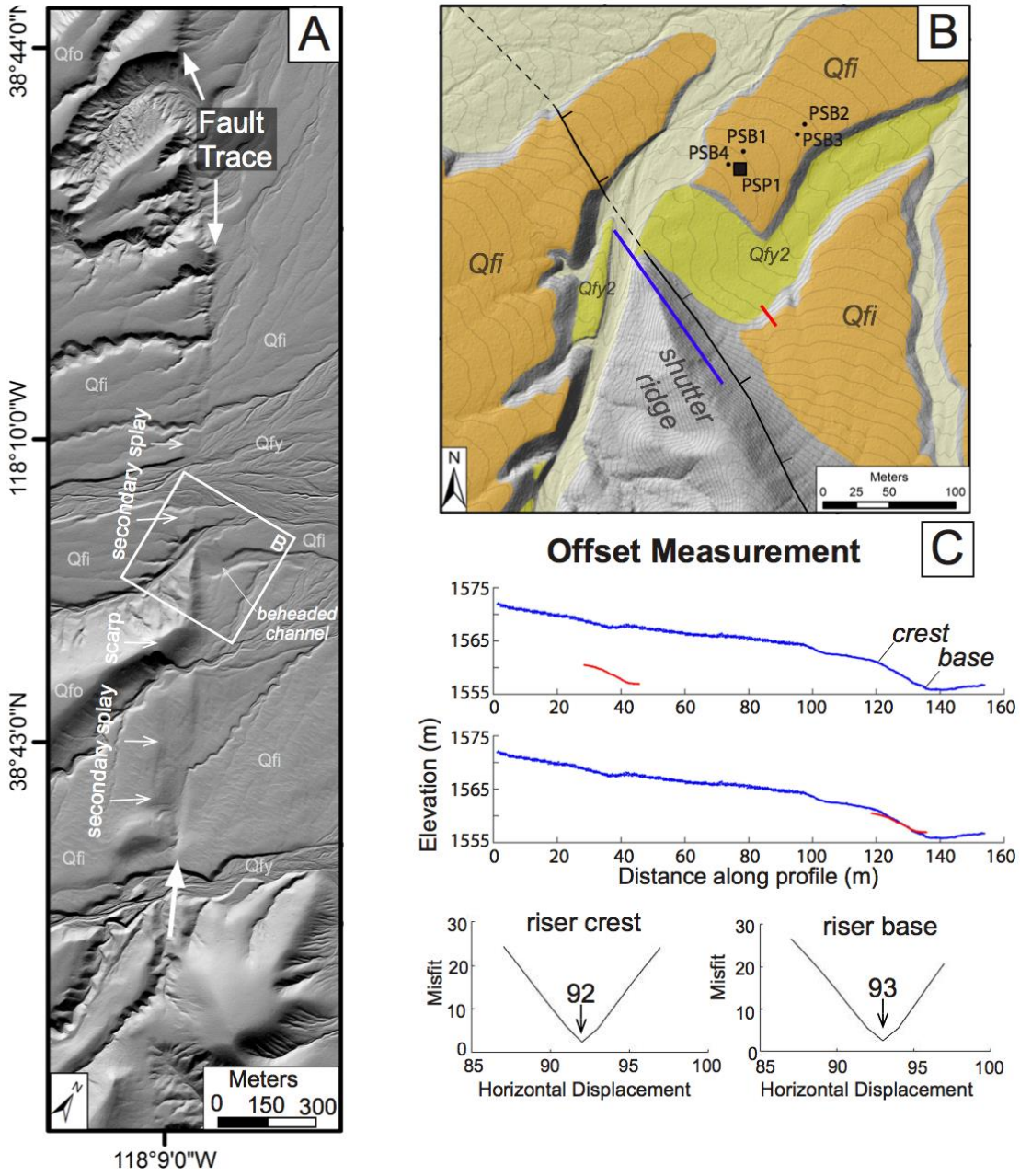

Figure 7. Petrified Springs fault slip rate site (please see Figure 2 for location). A) Hillshade image of lidar data along north portion of Petrified Springs fault. B) Detailed geologic map with 0.5 m contour intervals. Location of ^{36}Cl cosmogenic pit PSP1 shown by black square and boulder samples PSB1-4 are shown by black dots. Blue and red lines correspond to topographic profiles used for LaDiCaoz reconstructions shown in part (C). C) Horizontal reconstructions of topographic profiles. Lower plots show probability distribution functions and best fit of the reconstructions using the riser crest and base.

Dating Results

Results from the ^{10}Be and ^{36}Cl TCN dating of the offset fans at each slip rate site is listed in Tables 3, 4, and 5. The following provides detailed descriptions of the dated fan deposits, supported by site photos, generalized stratigraphic columns, and associated cosmogenic profile in the associated Figures 8 and 9. Detailed soil descriptions and texture analysis are provided in Table A1 within Appendix A. OSL results are provided in Figure 10.

^{10}Be Exposure Ages

Site IH ^{10}Be depth profile

The cosmogenic pit at the slip rate site on the Indian Head fault was excavated within the faulted Qfy2 alluvial fan surface at the location shown in Figure 4b. The pit exposed a poorly sorted unconsolidated massive conglomerate composed of angular pebbles and cobbles capped by a weak soil profile in the upper 17 cm of the deposit (Figure 8a). The soil is defined by a 7-cm-thick silt rich Av horizon underlain by an 11-cm-thick Bw-horizon (Figure 8a). Stage-1 carbonate development is observed through the entire section (Table A1). The ^{10}Be profile concentrations are similar throughout the depth profile and have no systematic decrease with depth (Figure 8a). The modeled simulations (grey shaded area) and best-fit model (black line) appear to capture the sample concentrations, however the roll over at the top of the section is not represented by the data. The best-fit profile provides an age of 10.4 $^{+37.1}/_{-0.3}$ ka.

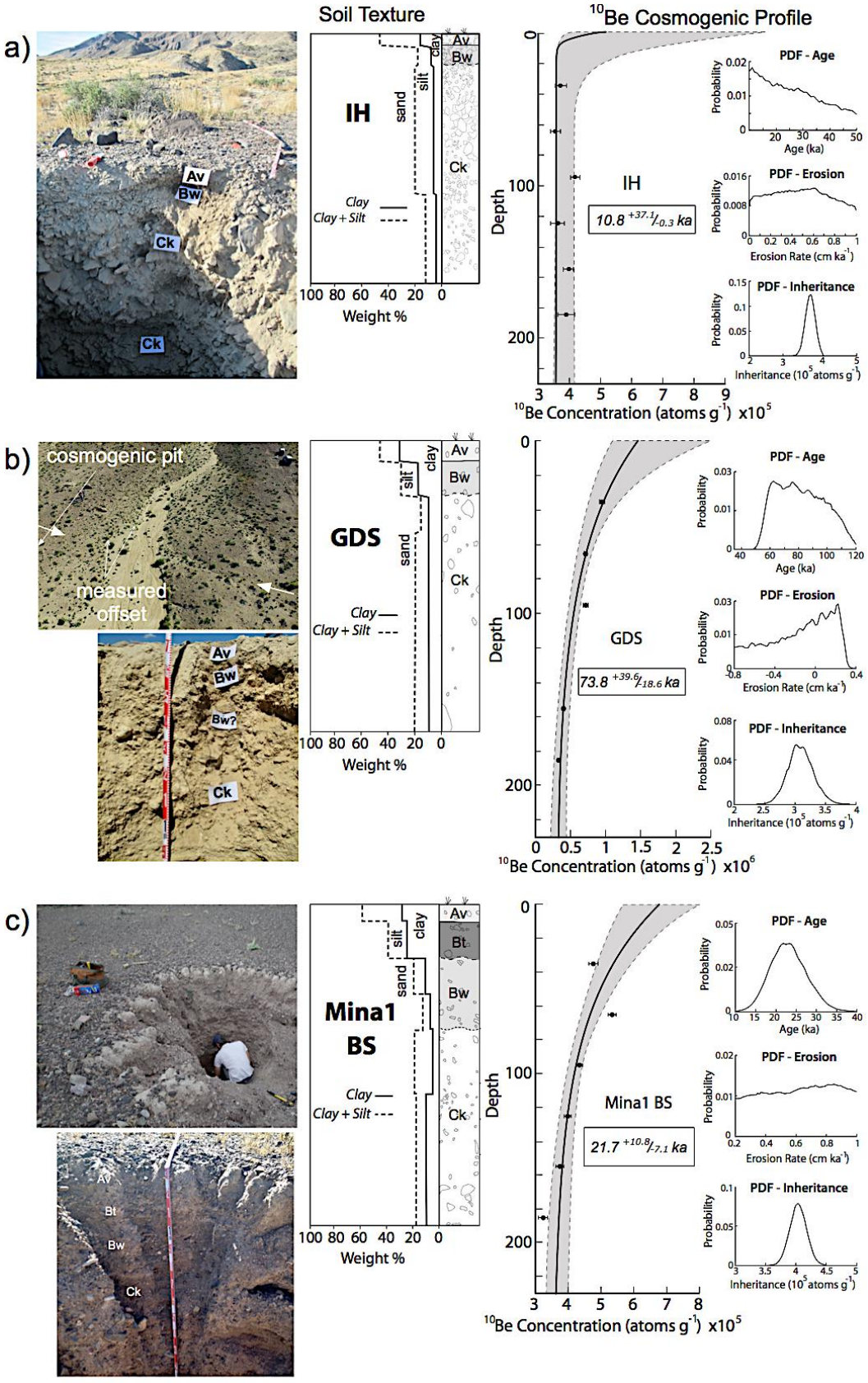
a)
Soil Texture
^{10}Be Cosmogenic Profile
Av
Bw
Ck
IH
sand
silt
clay
Clay
Clay + Silt
Weight %
Depth
IH
10.8 +37.1/-0.3 ka
PDF - Age
Probability
Age (ka)
PDF - Erosion
Erosion Rate (cm ka^{-1})
PDF - Inheritance
Inheritance (10^5 atoms g^{-1})
^{10}Be Concentration (atoms g^{-1}) x10^5
b)
cosmogenic pit
measured offset
Bw?
GDS
73.8 +39.6/-18.6 ka
^{10}Be Concentration (atoms g^{-1}) x10^6
c)
Bt
Mina1 BS
21.7 +10.8/-7.1 ka

Figure 8. ^{10}Be cosmogenic pit characteristics at sites IH (a), GDS (b), and Mina1-BS (c). Pictures of fan surface and pit are shown on the left. Middle shows soil texture plot (clay - solid line and clay+sand – dashed line) and soil horizons on simplified strat column. ^{10}Be concentrations vs. depth profiles are shown to the right. Solid black circles show sample concentrations with error bars. Gray area represents 100,000 profile simulations and solid black line shows best-fit output from Hidy et al. (2010) calculator. Subplots to the right show probability distribution functions (PDF) of age, erosion, and inheritance. Locations of each site are shown in Figures 4b, 5c, and 6b.

Table 3. Bayesian most probable ^{10}Be profile age results from Hidy et al. (2010) calculator.

^{10}Be Depth Profile	Surface Age (ka)	Inheritance (10^4 atoms g^{-1})	Erosion Rate (cm ka^{-1})
Mina1-BS	$21.7\ ^{+10.8}/_{-7.1}$	$40.38\ ^{+2.6}/_{-2.84}$	$0.84\ ^{+0.14}/_{-0.82}$
GDS	$73.8\ ^{+39.6}/_{-18.6}$	$30.33\ ^{+4.81}/_{-3.59}$	$0.23\ ^{+0.03}/_{-1}$
IH	$10.4\ ^{+37.1}/_{-0.3}$	$38.35\ ^{+2.17}/_{-3.18}$	$0.61\ ^{+0.36}/_{-0.41}$

Site GDS ^{10}Be Cosmogenic Pit

The depth profile pit at slip rate site GDS was dug into the Qfi fan on the north side of the southern fault strand (Figure 5c). The pit exposed a poorly sorted angular to subangular massive conglomerate composed of pebble-cobble capped by a 10-cm-thick silt rich Av horizon underlain by a ~15-cm-thick sandy loam Bw horizon (Figure 8b) with stage 2 carbonate development extending ~1.5 m below the surface (Table A1). The ^{10}Be concentrations generally show a systematic decrease with depth and the modeling appears to capture the data

(Figure 8b). The best-fit profile provides an age of 73.8 $^{+39.6}/_{-18.6}$ ka. The symmetrical pdf plot for inheritance (Figure 8b) suggest it to be reasonably well constrained, and thus the relatively larger uncertainty on both ends of the age is likely the consequence of the poorly constrained erosion rate, shown by the broad pdf plot for erosion (Figure 8b). The age of this surface does not match the amount of soil development observed in the pit. The relatively weak soil development observed in this pit is suggestive of Holocene age.

Site Mina1-BS ^{10}Be Cosmogenic Pit

The Mina1-BS depth profile pit was excavated into the displaced Qfi alluvial fan at the slip rate site for the Benton Springs fault (Figure 6b). The pit exposed a poorly sorted massive pebble conglomerate that has a moderately developed soil within the upper ~90 cm of the surface, characterized by a ~20-cm-thick rubified Bt horizon, marked by greater clay content (Figure 8c). The ^{10}Be concentrations generally show a systematic decrease with depth. The best-fit profile for all the samples provides an exposure age of 21.7 $^{+10.8}/_{-7.1}$ ka. Near the surface, the 30 and 60 cm sample concentrations appear to have respectively less and higher concentrations than what the modeling predicts and may be responsible for some of the uncertainty (Figure 8c). Similar to the GDS site above, the pdf of erosion appears to be poorly constrained and thus is likely adding to the uncertainty as well.

^{36}Cl Exposure Ages

Site GDS ^{36}Cl Cosmogenic Pit

^{36}Cl profile samples for site GDS were collected from the same pit as the GDS ^{10}Be samples (Figure 5c) and detailed description of the deposit and soil for this pit is provided in the appropriate section above. The strat column and soil textures are shown again in Figure 9a to provide context to the cosmogenic profile to the right. The ^{36}Cl profile concentrations show a systematic decrease with depth (Figure 9a) and modeling appear to fit most of the data. The best-fit profile yields a surface age of 61.4 ± 1.2 ka. Similar to the ^{10}Be profile at this site (Figure 8a), these results are much older than that what is expected from the soil development observations in the soil, yet is falls within error of the ^{10}Be profile age (73.8 $^{+39.6}/_{-\ 18.6}$ ka).

Site GDN ^{36}Cl depth profile pit

Cosmogenic profile samples were collected at the GDN slip rate site from a pit dug within the faulted Qfi fan surface on the northwest side of the fault (Figure 5b). The pit exposed a poorly sorted angular to sub angular pebble-cobble massive conglomerate, capped by a 10-cm-thick Av horizon underlain by a ~15-cm-thick sandy loam Bw horizon with stage 2+ carbonate development extending ~1.5 m below the surface (Figure 9b and Table A1). These observations are very similar to those previously described in the GDS cosmogenic pit and support our correlation of the Qfi surface between the two

slip rate sites (Figure 5a). The ^{36}Cl profile concentrations for the GDN profile show a systematic decrease with depth (Figure 9b) and the modeling appears to capture all the data points. The best-fit profile yields an age of 70.2 ± 5.7 ka. This age falls within the range of the two age results from the pit at site GDS, a surface correlative to site GDN, and similarly does not agree with the observed soil.

Site PSP1 ^{36}Cl Cosmogenic Pit

The PSP1 cosmogenic pit was dug into the Qfi surface of which the measured behead channel is incised into at the Petrified Springs fault slip rate site (Figure 7b**)**. The pit exposes a poorly sorted angular conglomerate composed of a sandy matrix supporting pebbles and cobbles (Figure 9c). A relatively well-developed argillic soil is present within the upper 25 cm of the deposit that is characterized by a ~15-cm-thick rubified Bt horizon, yielding high clay content, and stage 3 carbonate development (Figure 9c and Table A1). The ^{36}Cl concentrations show a systematic decrease with depth and the modeling appears to capture most of the data. The best-fit profile (black line; Figure 9c) yields an age of 153.5 ± 11.2 ka. Given that the soil is the most developed soil observed in this study, the older age result here seems to agree.

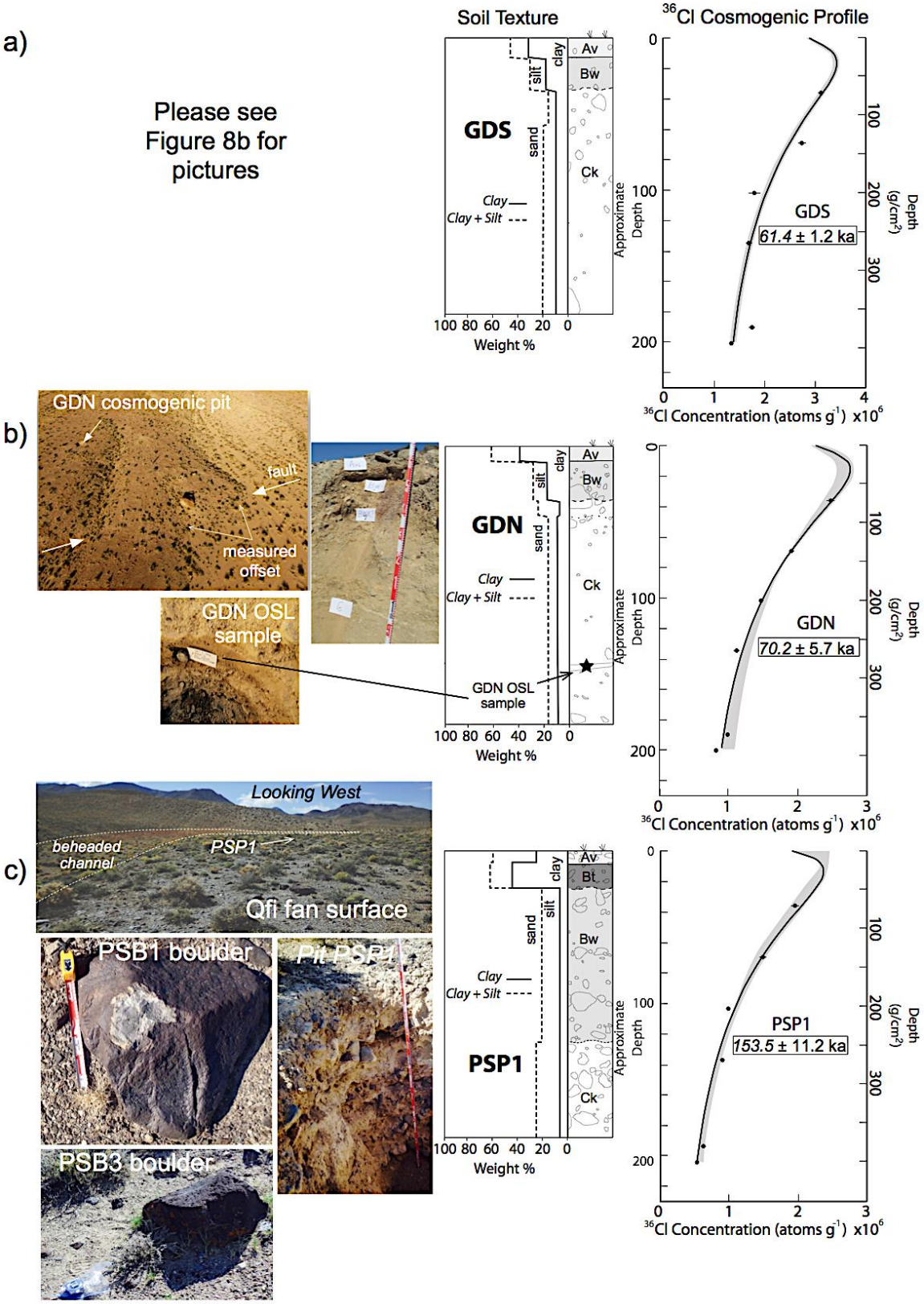
a)
Please see Figure 8b for pictures
Soil Texture
^{36}Cl Cosmogenic Profile
GDS
clay
silt
sand
Av
Bw
Ck
Clay
Clay + Silt
Weight %
Approximate Depth
GDS
61.4 ± 1.2 ka
^{36}Cl Concentration (atoms g^{-1}) x10^{6}
Depth (g/cm^2)
b)
GDN cosmogenic pit
fault
measured offset
GDN OSL sample
GDN
GDN OSL sample
70.2 ± 5.7 ka
c)
Looking West
beheaded channel
PSP1
Qfi fan surface
PSB1 boulder
Pit PSP1
PSB3 boulder
Bt
PSP1
153.5 ± 11.2 ka

Figure 9. ^{36}Cl cosmogenic pit characteristics at sites GDS (a), GDN (b), and PS (c). Pictures of fan surface and pit are shown on the left. Middle shows soil texture plot (clay - solid line and clay+sand – dashed line) and soil horizons on simplified strat column. ^{36}Cl concentrations vs. depth profiles for cosmogenic profiles shown to the right. Grey areas show uncertainty from 10,000 Monte Carlo simulations and black line shows best-fit output from CRONUScalc. Locations of each site are shown in Figures 5 b and c, and 7b.

Table 4. Bayesian most probable ^{36}Cl profile surface ages from CRONUScalc

^{36}Cl Profile	Surface Age (ka)	Inheritance (10^4 atoms g^{-1})	Erosion Rate ($g/cm^2/ka$)
GDS	61.4 ± 1.2	3.126	0 - 0.06
GDN	70.2 ± 5.7	2.22	0 - 0.06
PSP1	153.5 ± 11.2	2.611	0 - 0.43

^{36}Cl Boulder Exposure Ages

Four andesite boulders samples were collected from the same surface in which ^{36}Cl depth profile PSP1 was excavated (PSB1-4; Figure 7b). Pictures of boulder PSB3 and PSB1 are shown with the PSP1 cosmogenic profile in Figure 9c**,** and the age results from CRONUScalc are summarized in Table 5. Average age results from the two scaling schemes yield 127 ± 33 ka, 305 ± 76 ka, 119 ± 24.5 ka, 410 ± 150 ka for boulders PSB1, PSB2, PSB3, and PSB4, respectively.

Table 5. Summary of ^{36}Cl boulder exposure ages. Values shown from Lifton-Sato scaling scheme (Lifton et al., 2014) and Lal-Stone (Lal, 1987; Stone, 2000) along with average age.

^{36}Cl Boulder Sample	Lifton-Sato (ka)	Lal-Stone (ka)	Average (ka)
PSB1	116 ± 22	130 ± 30	127 ± 33
PSB2	276 ± 47	315 ± 66	305 ± 76
PSB3	111 ± 16	123 ± 21	119 ± 24.5
PSB4	370 ± 110	430 ± 130	410 ± 150

OSL Age Results

An OSL sample was collected within a lens of fine-medium sand ~1.5 m below the surface within the GDN cosmogenic pit (Figure 9b). Two statistically significant peaks are identified using *RadialPlotter* (Vermeesch, 2009) and are shaded with a corresponding number in Figure 10. Peak 1 has a dose equivalent value of 761.8 ±9.7 Gy and peak 2 has a dose equivalent value of 1395 ±23 Gy (Figure 10). Applying a dose rate value of 4.4 ± 0.27 Gy/ka, these values provide ages of 18.89 ka ± 1.2 and 32.26 ka ± 4.3 ka for Peaks 1 and 2, respectively. We interpret Peak 1 (18.89 ± 1.2 ka) to most likely represent the last exposure event of the sample, while Peak 2 is likely representative of partially bleached grains, those not fully exposed or reset during deposition. The age of Peak 1 (18.89 ± 1.2 ka) is assumed to be representative of the approximate time of burial, and since the OSL sample was collected 1.5 m below the surface, this age provides a maximum age to the surface of the Qfi deposit at site slip rate site GDN. This age is much younger than the predicted surface age from the ^{36}Cl GDN profile (Figure 9b), which is from the same pit. Furthermore, the ^{36}Cl and ^{10}Be ages from the correlative surface at the GDS cosmogenic pit of 61.4 ± 1.2 and 73.8 $^{+39.6}/_{-18.6}$ ka, respectively, contrast with the OSL age. This younger OSL age is in line the soil in both the GDN pit (Figure 9b) and the GDS pit (Figure 8b).

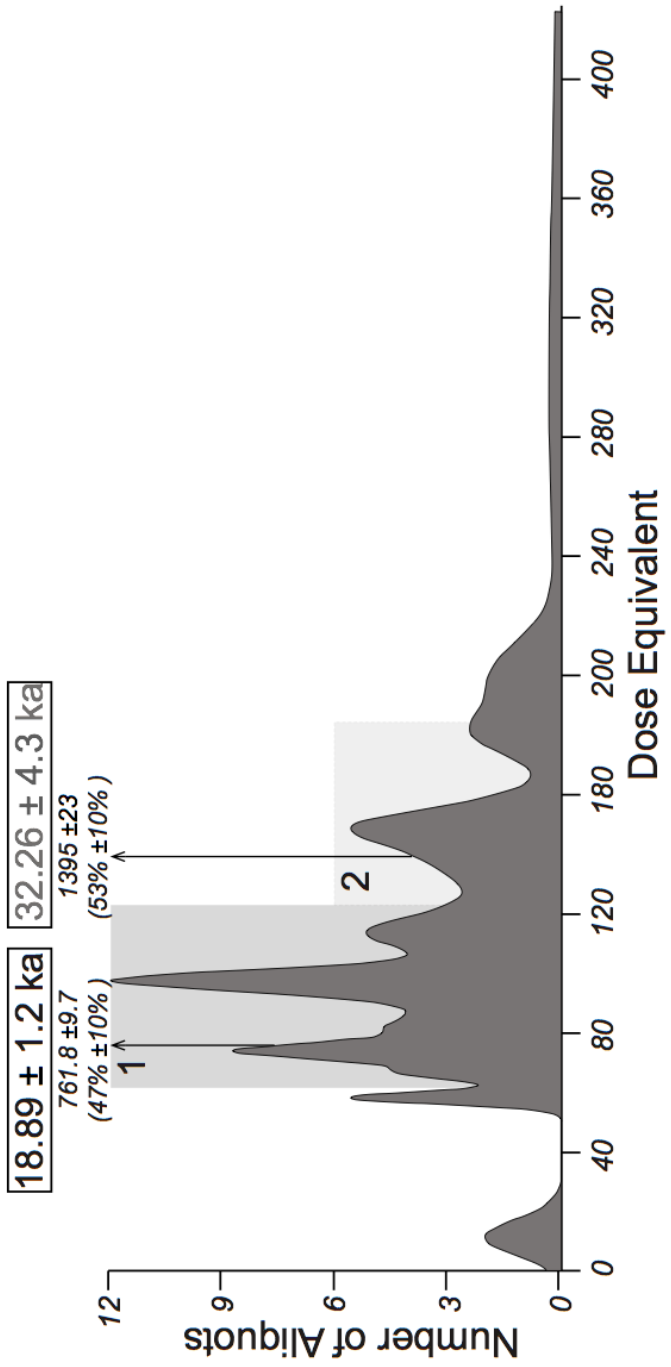

Figure 10. Dose Equivalent plot of OSL sample from site GDN for 32 aliquot measurements. Location of sample is shown in Figure 9b. Shaded areas show two statistically significant peaks (1 and 2) with associated ages above using dose rate of 4.4 ± 0.27.

Discussion

Reconciling Alluvial Fan Surface Ages at the Slip Rate Sites

PS Site

Comparison of ^{36}Cl depth profiles and surface boulder ages show two age populations (Figure 11). Group 1 includes the ^{36}Cl profile (PSP1) and boulder samples PSB1 and PSB3, spanning an age of 94 to 164.7 ka. Using the best-fit age result from the PSP1 profile (153.5 ka) and the maximum age limit of the Lifton-Sato scaling scheme of the PSB3 boulder (127 ka), we can constrain an age of 148 ± 13.3 ka that is within error of the boulder samples and covers most probable age result of PSP1 for Group 1 (Figure 11). The older ages of the boulders that comprise Group 2, PSB2 and PSB4, span range from 229 to 560 ka, and are likely a reflection of inheritance thus are unrepresentative of the deposition and abandonment of the Qfi fan. We use the age of Group 1 (148 ± 13.3 ka) as the preferred age for the abandonment of the Qfi surface at the Petrified Springs slip-rate site (Figure 7b), as it includes the profile and half of the four boulders sampled. This age serves as a maximum to the measured displacement, as the abandonment of the Qfi surface occurred during incision, forming the beheaded channel, and later sequential offset (Figure 7b).

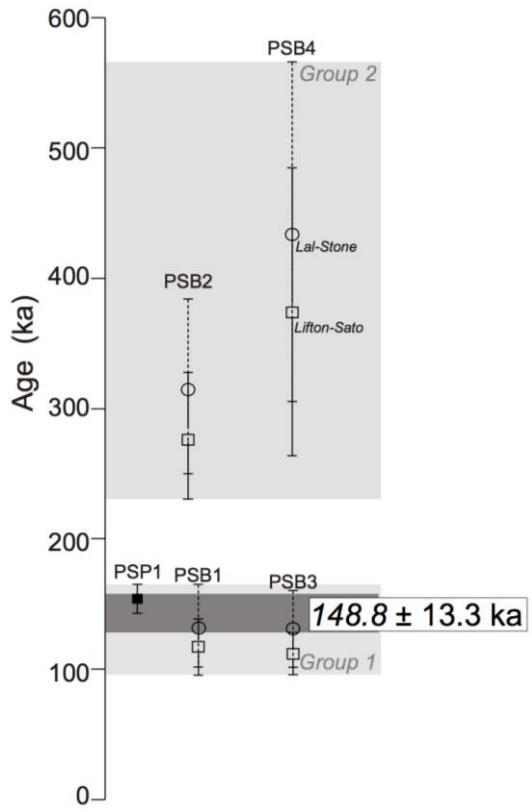

Figure 11. Age distribution of cosmogenic ^{36}Cl samples collected at the Petrified Springs fault slip rate site (PS). Sample locations are shown in Figure 7b. Age results are plotted along with the associated uncertainties, represented by error bars. The solid black square is the Bayesian most probable age from the ^{36}Cl cosmogenic pit. Boulder age results are shown as hollow boxes and circles with associated uncertainty using the scaling schemes of Lifton-Sato (Lifton et al., 2014) represented by squares with solid lines and Lal-Stone (Lal, 1987; Stone, 2000) represented by circles with dashed lines. Lighter grey shading shows age range of Groups 1 and 2 and the darker grey show age ranges that are within error for Group 1.

Mina1-BS Site

The soil profile observed in the Mina1-BS cosmogenic pit (Figure 8c and Table A1) is similar to, if not, slightly more developed than other soil profiles within the region that have been associated to the 15.5 ka Lahontan highstand (Benson and Thompson, 1987; Adams and Wesnousky, 1999). The ^{10}Be

cosmogenic profile exposure age result (21.7 $^{+10.8}/_{-7.1}$ ka) is relatively consistent with the age of the highstand, thus the amount of soil development in the Mina1-BS cosmogenic pit agrees with the age result. The estimated erosion rate (0.84 $^{+0.14}/_{-0.82}$ cm ka^{-1}) is relatively poorly constrained (Table 3 and Figure 8c); yet the amount of soil development in the pit suggests that the erosion has been minimal to this surface. The uncertainties in the age result are likely a reflection of the poor constraint on erosion. We cannot rule out either the upper or lower bound, thus we consider the full age rage of the ^{10}Be cosmogenic profile (21.7 $^{+10.8}/_{-7.1}$ ka) to represent the age of the surface. This age also generally agrees with other prior age estimates (< 36 ka) made for this exact surface based on soil chronosequences developed within Dunlap Canyon and the region (Bell, 1995; Wesnousky, 2005a). We consider the exposure age to best represent the abandonment of the faulted Qfi surface at the Benton Springs fault slip rate site, and thus serves as a maximum age to the faulting manifested within the Qfi fan.

GDS and GDN Sites

The faulted Qfi fan at the two Gumdrop fault slip rate sites is correlative between the two sites, thus the age results from the two pits should be similar. The ^{10}Be and ^{36}Cl cosmogenic profile ages from both sites (GDN and GDS) fall within the uncertainty of another, providing a wide range of possible exposure ages, ranging from 55.2 to 113.4 ka (Figure 12). Using the preferred age results from the GDS ^{10}Be and ^{36}Cl profiles (73.8 and 61.4 ka), an age of 67.6 ka ± 6.2 satisfies the most probable output for all profiles. This cosmogenic age contrasts

with the much younger age result of the GDN-OSL sample (18.9 ± 1.2ka; Figure 12), which should provide a maximum age to the surface.

There are several observations that support the use of the younger OSL age over the cosmogenic age for the surface. First, the soils in both the GDN and GDS pits (shown in Figures 9a and b) are less developed that the soil observed in the Mina1-BS cosmogenic pit (Figure 8a), determined to be ~21.7 ka. Soils such as these are comparable to the soils associated with the 15.5 ka Lahontan highstand (Adams and Wesnousky, 1999), and provides support to the OSL age (18.9 ± 1.2 ka). Second, the locations of the GDN and GDS sites are within the distal portion of the Qfi fan and lie below deeply incised older and higher fan deposits within the large canyon to the northeast (Figure 2) and are likely sourcing the sediment to these sites. In Figure 3a, we point to these older fans within the canyon that are mapped on the lidar data. Progressive erosion of the older fan units and subsequent sequential deposition could potentially mask the in-situ signal expected for these profiles, such that the modeled inheritance in the profile is underestimated and thus results in an apparently older age. This may provide an explanation as to why the cosmogenic ages are consistently older than the OSL age. We cannot provide clear evidence of this from our observations, thus we consider both the cosmogenic age (67.6 ± 6.2 ka) and the OSL age (18. 9 ± 1.2 ka) for slip rate calculations.

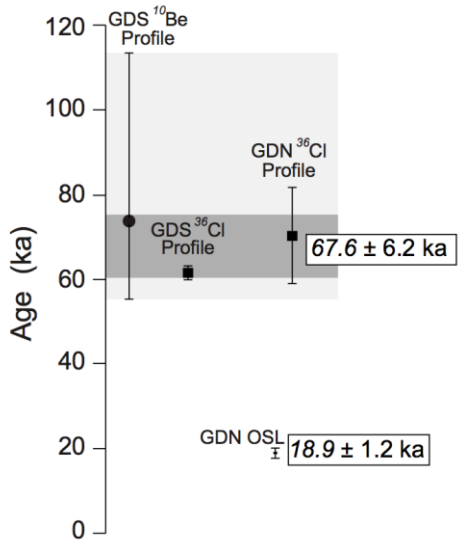

Figure 12. Gumdrop Hills fault age distribution of the offset Qfi fan at slip rate site GDN and GDS. Age results from ^{10}Be and ^{36}Cl profiles and the OSL sample are plotted along with the associated uncertainties, represented by error bars. The range of cosmogenic ages is shaded in light grey, and the darker grey is the age that falls within error of all three profiles. Cosmogenic profile models and pit characteristics are shown in Figures 8 and 9. Histogram plot of OSL dose equivalent for the measured aliquot samples is shown in Figure 10.

IH Site

The age result of the IH cosmogenic profile (10.4 $^{+37.1}/_{-0.3}$ ka) has a relatively large positive uncertainty associated with it. There are several observations that lead us to disregard the upper age bound. First, the large positive uncertainty (+37.1 ka) is likely the result of the abrupt roll over of the profiles modeled near the surface (<30 cm), however, this is not reflected by the sample concentrations and is likely not real (Figure 8a). Second, the lack of a systematic decrease of ^{10}Be concentration with depth observed in the IH cosmogenic profile (Figure 8a) are generally symptomatic of younger deposit

(Owen et al., 2011), where the inherited TCN signal is likely exceeding the concentrations of ^{10}Be produced in-situ. This explains the relatively well-constrained pdf plot for inheritance shown in Figure 8a, and the value of inheritance (38.35 x 10^4 atoms g^{-1}) is similar to the concentrations of all the profile samples (Figure 8a). Finally, the soil profile observed within the deposit (Figure 8a and Table A1) is the least-developed out of all the depth profile pits in our study, and the geomorphic expression of the alluvial fan element, exhibited by bar and swale topography and no desert pavement development, which suggest a youthful surface. We therefore interpret the age of this surface to be more likely around 10.8 to 10.5 ka, and use this range to represent the age of abandonment of the Qfy2 surface at the Indian Head slip-rate site, providing a maximum age to the faulting.

Slip Rates

We determine horizontal slip rates for each of the slip rate sites based on the offset measurements and age constraints made for each site. We use the probabilistic approach of Zechar and Frankel (2009), where age and displacement measurements are treated as random variables and characterized by a probability density function (pdf). The slip rate pdf is then solved for by the integration of the age and displacement pdf's (Figure 13). Our method of measuring displacement using the crest and bases of the fan risers within LaDiCaoz generally provides a best-fit offset that we associate with a representative uncertainty based on site conditions, thus we apply Gaussian

pdf's to represent our displacements in these analysis. The results from our discussion of the ages of the faulted surfaces generally yield symmetrical age distributions, and we also apply Gaussian pdf's to the ages. Input parameters are provided in Table 6. The result are presented at 95.45% confidence levels in Table 6, and are representative of minimum rate, due the assumption made at each slip rate site that the displacement accrued post abandonment of these fans.

Results yield a horizontal slip rate for the IH site on the Indian Head fault at 0.8 ± 0.1 mm/yr for the displaced Qfy2 fan. A slip rate of 0.3 ± 0.1 mm/yr using TCN ages and a rate of $0.9\ ^{+0.3}/_{-0.2}$ mm/yr using OSL ages are determined for the GDN and GDS sites on the Gumdrop Hills fault. The pdf for the cosmogenic slip rate for sites GDN and GDS is absent in Figure 13 due to the very low rate. The Mina1-BS site on the Benton Springs faults provides the fastest slip rate of 1.5 ± 0.2 mm/yr and the PS site on the Petrified Springs fault yields a slip rate of 0.6 ± 0.1 mm/yr. These latter rates are comparable to prior geologic estimates (Wesnousky, 2005a), which provide rate estimates on the order of ~1 and 1.1–1.6 mm/yr for the Benton Springs and Petrified Springs faults, respectively. For all but the Indian Head fault, these rates are derived from measured offsets within late-Pleistocene deposits, thus can be considered late- Pleistocene slip rates. The Indian Head fault slip rate was determined within an early-Holocene age fan, and thus is representative of a Holocene rate.

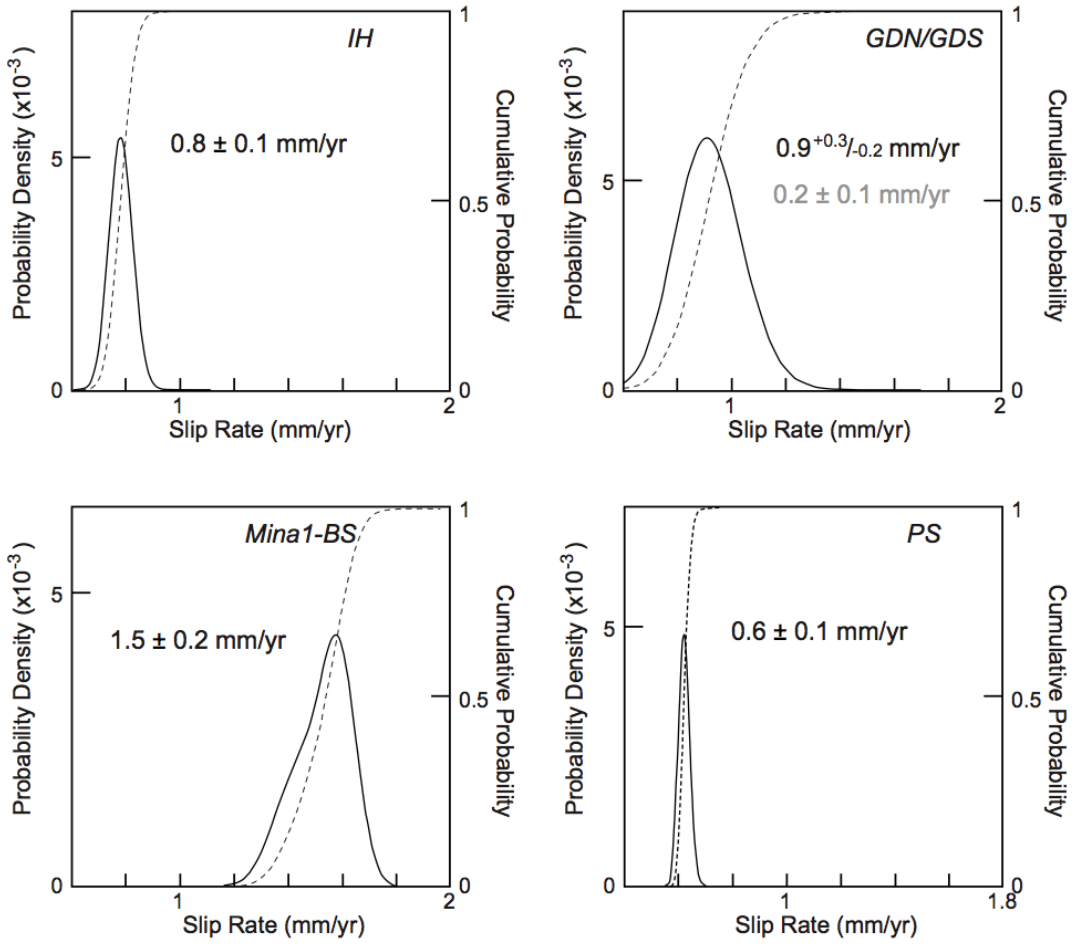

Figure 13. Horizontal slip rate probability density function (pdf) using Zechar and Frankel (2009) method based on measured offset risers and modeled ages of each slip rate site (IH – Indian Head fault; GDN/GDS – Gumdrop Hills fault; Mina1-BS – Benton Springs fault; PS – Petrified Springs fault). Solid black lines represent pdf of the slip rate and dashed line represent cumulative probability distribution of the data shown in Table 6.

Table 6. Input parameters and results of slip rate analysis.

Site	Displacement (m)	Age (ka)	**Slip Rate (mm/yr)**	Fault
IH	8 ± 0.4	10.25 ± 0.25	**0.8 ± 0.1**	Indian Head Fault
GDN/GDS	17.25 ± 2.05	67.6 ± 6.2 18.9 ± 1.2	**0.3 ± 0.1** **$0.9^{+0.3}/_{-0.2}$**	Gumdrop Hills Fault
Mina1-BS	34.5 ± 1.4	23.6 ± 1.4	**1.5 ± 0.2**	Benton Springs Fault
PS	92.5 ± 0.5	148.8 ± 13.3	**0.6 ± 0.1**	Petrified Springs Fault

The slip rate derived from the cosmogenic ages on the Gumdrop Hills fault is significantly less in comparison to the others (Table 6), while the rate derived from the OSL age is more equivalent to the other faults. It could be suggested that the locations of the slip rate sites (GDN and GDS) on the Gumdrop Hills fault (Figure 2) are at the southern end of the fault, and thus the offset measured across the two fault stands is an under-representation of the total slip (e.g. Bürgmann et al., 1994; Jónsson et al., 2002). A fault with a low rate, such as 0.3 mm/yr, would likely not be as well-expressed in the geomorphology, and the observations from the regional mapping suggest that the Gumdrop Hills fault is relatively well-expressed and is likely slipping faster than 0.3 mm/y. Because of this, we give preference towards the higher ($0.9\ ^{+0.3}/_{-0.2}$ mm/yr) slip rate for the Gumdrop Hills fault but cannot neglect the possibility for the lower rate.

Prior geodetic studies have shown that the majority of dextral shear motion (1–5 mm/yr) is accommodated in the eastern portion of the central Walker Lane, across the strike-slip faults of this study, while the majority of the extensional component (>2 mm/yr) of the transtensional strain is focused to the west, along the normal fault bounded basins (Figure 1; Oldow et al., 2001; Surpless, 2008; Bormann et al., 2016). Summing the preferred slip rate of the four faults studies here provides a cumulative geologic rate of 4.0 ± 0.7 mm/yr. We consider this cumulative rate to be a minimum for the central Walker Lane strike slip faults, as we were unable to determine a slip rate for the Agai Pah fault (APF; Figure 2). It appears that the minimum cumulative rate found in this study

lies near the higher end of the geodetic estimates, and suggest that the normal faults to the west (Figure 2) accommodated almost half of the ~8 mm/yr of geodetic strain budget for the central Walker Lane.

Cumulative displacement estimates across the central Walker Lane faults have ranged from 48–60 km (Ekren and Byers, 1984) to 60–78 km (Hardyman et al., 2000), but due to the overlap of these faults with the normal faults to the west and northwest (Figure 1), a value of ~40 km is now the preferred cumulative offset value (Faulds and Henry, 2008) since the initiation of faulting in the central Walker Lane at ~10 Ma (Hardyman and Oldow, 1991). If we apply our cumulative slip rate (4.0 ± 0.7 mm/yr) over the 10 Ma time-span, we get a cumulative offset of 33 to 47 km, values that are within range of the prior long-term estimates. The lower value (33 km) may suggest that the rates have decrease over the last 10 Ma, while the higher value (47 km) may suggest more constant rates of slip, however the data we present here are insufficient to say.

Rupture Characteristics and Seismotectonic Scaling Relations

The Benton Spring fault is the longest of the central Walker Lane strike-slip faults, stretching for ~100 km (Figure 2). Empirical scaling relations (Wells and Coppersmith, 1994; Wesnousky, 2008) for a strike-slip fault of this length would suggest maximum coseismic displacements of 3–5 m. The lower values of offset (1.25–5 m) observed along the southern portion of the Benton Springs (Figure 3a) are within Holocene alluvial fans (Qfy2) and are within range of expected coseismic displacements. Given that this is the longest fault of the

central Walker Lane fault system, one should expect the others to have less coseismic displacements. Using the higher coseismic values in conjunction with the range of the new slip rates determined here, spanning from 0.6 to 1.7 mm/yr, we find reoccurrence time intervals to be on order of 5.6 ± 2.7 ka, with M_w <7.2.

The observations from fault trace types in the Quaternary regional mapping (Figure 2) revealed variable Quaternary fault activity along strike. This is best illustrated by our observations along the Benton Springs fault (Figure 2 and 3a), where the southern portion of the fault exhibited fault traces within Holocene alluvial fan units and are associated with various lower magnitude offsets (1.25–5 m). Further to the northwest along strike, after the fault cuts through the Gabbs Valley Range (Figure 2), the fault trace is concealed by Holocene deposits, including Qfy, Ql, and Qb deposits, and the mapped “certain” fault traces (solid fault lines; Figure 2 and 3b) are limited to late Pleistocene (Qfi) alluvial fans and bedrock. This suggests that the most recent surface ruptures have been limited to the southern portion of the fault in Soda Spring Valley (Figure 2), where the length of the fault extends for ~30 km. Empirical scaling relations for a fault of this length suggest that the southern segment of Benton Springs fault is capable of a M_w 6.9, equivalent to a maximum coseismic offset of ~4 m, and is similar to the lower magnitude offset observed along the fault within Soda Springs Valley (Figure 2). These observations suggest that the most recent surface rupturing events on the Benton Springs faults were limited to the southern portion, such that the fault is segmented along strike. The lack of age constraints on the faulted

Qfi fan surfaces to the north, along the Terrill Mountains (Figure 2 and 3b), prevents us from saying whether this holds true for the long-term, thus this may only be characteristic of Holocene ruptures.

Spatiotemporal variable strain release across the Central Walker Lane

The observations from the Quaternary regional mapping also revealed variable Quaternary fault activity amongst the faults. The Indian Head and the Benton Springs faults have clear expressions within Holocene (Qfy2) alluvial fans, suggesting that both have experienced surface rupturing events during the Holocene. This is supported on the Benton Springs fault by the paleoseismic trench of Wesnousky (2005a), which showed evidence for a surface rupturing earthquake during the last ~1000 years (location of trench shown in Figure 6b). In addition, the smaller magnitude offsets observed along the southern portion of the Benton Springs fault range from 1.25–7 m and are manifested within Qfy2 fans (Figure 3a). The range in offset magnitude is suggestive of multiple Holocene ruptures, with the lower values (1.25–4 m) representative of the most recent event (MRE), and the larger (5–7 m) offsets are likely the culmination of the MRE and penultimate event. The paleoseismic history of the Indian Head fault is less constrained, however, the age result of the displaced Qfy2 fan (10.3–10.8 ka) obtained at the slip rate site (IH; Figure 4) shows that the displacement is of Holocene age. Using empirical scaling relations (Wells and Coppersmith, 1994; Wesnousky, 2008) for a ~45 km long strike-slip fault, would predict maximum coseismic displacements to be on the order of 3–4 m. The offset

measurement at the slip rate site provided an average displacement measurement of 8 ± 0.4 m, thus it is likely that of at least two Holocene earthquakes have occurred.

The “certain” fault traces (solid fault lines; Figures 2 and 3) of the Gumdrop Hills (GDF) and Petrified Springs faults (PSF), on the other hand, are limited to intermediate (Qfi) and older (Qfo) fan units and are absent within the Holocene fans (Figure 2 and 3), suggesting that these faults have not ruptured during the Holocene. Yet, their rates of slip determined in this study, ~0.9 (GDF) and ~0.6 mm/yr (PSF) (Table 6), are comparable to those estimated for the multi-event Holocene active Benton Springs fault (~1.5 mm/yr) and Indian Head fault (~ 0.8 mm/yr). The reoccurrence interval discussed above suggests a maximum reoccurrence interval of 8.3 ka, meaning the Gumdrop Hills fault and the Petrified Springs fault should have at least one Holocene age rupture. This was not observed along these two faults.

Explanations for this observed Holocene quiescence of the Gumdrop Hills and Petrified Springs faults may be the result of longer-term spatiotemporal variations of slip amongst the central Walker Lane fault system (e.g. Frankel et al., 2011; Dolan et al., 2016), such that Walker Lane dextral shear strain is released at different time periods on different faults within the system. Implications for this type of behavior results in less predictable or uncertain reoccurrence intervals on the individual faults.

Conclusions

The new offset measurements and age results performed in this study allow for minimum late Pleistocene to Holocene strike-slip rates to be placed on the Benton Springs (1.5 ± 0.2 mm/yr), Petrified Springs (0.6 ± 0.1 mm/yr), Gumdrop Hills (0.9 $^{+0.3}/_{-0.2}$), and Indian Head (0.8 ± 0.1 mm/yr) faults in the central Walker Lane. The cumulative rate suggests that these faults accommodate at least half of the ~8 mm/yr geodetic stain budget measured across this portion of the Walker Lane and satisfies the cumulative displacement since initiation of faulting. Regional along-strike Quaternary mapping of these faults further suggest that the Benton Springs and Indian Head faults have had multi-event Holocene ruptures, while surface rupture on the Gumdrop Hills and Petrified Springs faults have likely not occurred since the late Pleistocene. We also find that Holocene rupture on the Benton Springs fault was likely limited to the southern segment, possibly reaching magnitudes up to M_w *6.9*, and associated with the 1 – 4 m offsets manifested within the Holocene fan deposits observed along the fault. The new slip rates and associated coseismic Holocene displacements further suggests maximum reoccurrence time intervals to be on order of 5.6 ± 2.7 ka, and the absence of Holocene rupture on the Gumdrop Hills and Petrified Springs faults suggests that Walker Lane shear strain is released at different time periods on different faults within the strike slip fault system.

Acknowledgements

Many people deserve thanks for helping with the ideas and results of this research come to fruition. Big thanks to Xinnan Li for assistance in hand digging many of the pits, documentation of soil characteristics, and sampling for cosmogenics. Discussion in the field or in the office with fellow UNR graduate students Ian Pierce, Tabor Reedy, and Chad Carlson were very helpful. Many thanks my friends and other graduate students at the University of Cincinnati for training me in the lab and keeping me in good company for the 2 months spent in the cosmogenic labs. In particular, thanks to Jason Cesta who provided necessary advice and assistance for the cosmogenic ^{36}Cl sample preparation and modeling.

References Cited

Adams, K. D., and Wesnousky, S. G., 1999, The Lake Lahontan highstand: age, surficial characteristics, soil development, and regional shoreline correlation: Geomorphology, v. 30, p. 357-392.

Argus, D. F., and Gordon, R. G., 1991, Current Sierra Nevada-North America motion from very long baseline interferometry: Implications for the kinematics of the western United States: Geology, v. 19, p. 1085-1088.

Bell, J. W., 1995, Quaternary geologic map of the Mina quadrangle, NV: Nevada Bureau of Mines and Geology, Reno, NV.

Bell, J. W., Caskey, J. S., and Ramelli, A. R., 2004, Pattern and rates of faulting in the central Nevada seismic belt, and paleoseismic evidence for prior beltlike behavior: Bulletin of the Seismological Society of America, v. 94, no. 4, p. 1229-1254.

Bennett, R. A., Wernicke, B. P., Niemi, N. A., Friedrich, A. M., and Davis, J. L., 2003, Contemporary strain rates in the northern Basin and Range province from GPS data: Tectonics, v. 22, no. 2.

Benson, L. V., and Thompson, R. S., 1987, Lake-level variation in the Lahontan Basin for the past 50,000 years: Quaternary Research, v. 28, p. 69 - 85.

Birkeland, P. W., 1984, Soils and geomorphology. Oxford University Press, New York, 372 pp.

Borchers, B., Marrero, S. M., Balco, G., Caffee, M. W., Goehring, B., Lifton, N. A., Nishiizumi, K., Phillips, F., Schaefer, J., and Stone, J. O., 2016, Geological calibration of spallation production rates in the CRONUS-Earth project: Quaternary Geochronology, v. 31, p. 188-198.

Bormann, J. M., Hammond, W. C., Kreemer, C., and Blewitt, G., 2016, Accommodation of missing shear strain in the Central Walker Lane, western North America: Constraints from dense GPS measurements: Earth and Planetary Science Letters, v. 440, no. C, p. 169-177.

Bull, W. B., 1991, Geomorphic responses to climatic change.

Burgmann, R., Pollard, D., Martel, S., 1994, Slip distributions on faults: Effects of stress gradients, inelastic deformation, teterogeneous host-rock stiffness, and fault interaction: Journal of Structural Geology, v. 16, no. 12, p. 1675-1690.

Carlson, C. W., 2014, Preliminary geologic map of the Terrill Mountains quadrangle, Churchill and Mineral counties, Nevada. Open-File Report 14-4.

Carlson, C. W. 2017, Kinematics and Transfer Mechanisms of Strain Accommodation at the Transition between the Northern and Central Walker Lane, Western Nevada: PhD Dissertation, Univeristy of Nevada Reno.

Carlson, C. W., Pluhar, C. J., Glen, J. M. G., and Farner, M. J., 2013, Kinematics of the west-central Walker Lane: Spatially and temporally variable rotations evident in the Late Miocene Stanislaus Group: Geosphere, v. 9, no. 6, p. 1530-1551.

Cashman, P. H., and Fontaine, S. A., 2000, Strain partitioning in the northern Walker Lane, western Nevada and northeastern California: Tectonophysics, v. 326, p. 111-130.

Cowgill, E., 2007, Impact of riser reconstructions on estimation of secular variation in rates of strike–slip faulting: Revisiting the Cherchen River site along the Altyn Tagh Fault, NW China: Earth and Planetary Science Letters, v. 254, no. 3-4, p. 239-255.

Daniel, T., and Langille, J., 2016, Constraints on the Quaternary Fault Offset History Along the Benton Springs Right-Lateral Strike-Slip Fault, West-Central Nevada, The National Conference on Undergraduate Research 2016: Asheville, NC, NCUR.

Dokka, R. K., and Travis, C. J., 1990, Role of the eastern California shear zone in accommodating Pacific-North American plate motion: Geophysical Research Letters. v. 17, no. 9, p. 1323 - 1326.

Dolan, J. F., McAuliffe, L. J., Rhodes, E. J., McGill, S. F., and Zinke, R., 2016, Extreme multi-millennial slip rate variations on the Garlock fault, California: Strain super-cycles, potentially time-variable fault strength, and

implications for system-level earthquake occurrence: Earth and Planetary Science Letters, v. 446, p. 123-136.

Dortch, J.M., Owen, L.A., Haneberg, W.C., Caffee, M. W., Dietsch, C., Kamp, U., 2009, Nature and timing of mega-landslides in northern India: Quaternary Science Review 28, p. 1037-1056.

Ekren, E. B., and Byers, J., F M, 1984, The Gabbs Valley Range - A well-exposed segment of the Walker Lane in west-central Nevada: Western geological excursions, Guidebook, v. 4, edited by J. Lintz Jr., p. 203-215, Geological Society of America, Boulder, CO.

Ekren, E. B., and Byers, J., F M, 1985a, Geologic Map of the Gabbs Mountain, Mount Ferguson, Luning, and Sunrise Flat Quadrangle, Mineral and Nye Counties, Nevada., U.S. Geological Survey Map, I-1577.

Ekren, E. B., and Byers, J., F M, 1985b, Geologic map of the Win Wan Flat: Kinkaid NW, Kinkaid, and Indian Head Peak Quadrangles, Mineral County, Nevada: US Geological Survey, Miscellaneous Investigations Series Map I-1578.

Ekren, E. B., and Byers, J., F M, 1986a, Geologic map of the Mount Annie NE, Mount Annie, Ramsey Spring, and Mount Annie SE quadrangles, Mineral and Nye counties, Nevada, U.S. Geological Survey Map, I-1579.

Ekren, E. B., and Byers, J., F M, 1986b, Geologic map of the Murphys Well, Pilot Cone, Copper Mountain, and Poinsettia Spring quadrangles, Mineral County, Nevada, U.S. Geological Survey Map, I-1576.

Faulds, J. E., and Henry, C. D., 2008, Tectonic influences on the spatial and temporal evolution of the Walker Lane: An incipient transform fault along the evolving Pacific–North American plate boundary, in Spencer, J.E., and Titley, S.R., eds., Ores and orogenesis: Circum-Pacific tectonics, geologic evolution, and ore deposits: Arizona Geological Society Digest 22, p. 437-470.

Faulds, J. E., Henry, C. D., and Hinz, N. H., 2005, Kinematics of the northern Walker Lane: An incipient transform fault along the Pacific–North American plate boundary: Geology, v. 33, no. 6, p. 505.

Frankel, K. L., Brantley, K. S., Dolan, J. F., Finkel, R. C., Klinger, R. E., Knott, J. R., Machette, M. N., Owen, L. A., Phillips, F. M., Slate, J. L., and Wernicke, B. P., 2007, Cosmogenic 10Be and 36Cl geochronology of offset alluvial fans along the northern Death Valley fault zone: Implications for transient strain in the eastern California shear zone: Journal of Geophysical Research, v. 112, no. B6, p. 47.

Frankel, K. L., Dolan, J. F., Owen, L. A., Ganev, P., and Finkel, R. C., 2011, Spatial and temporal constancy of seismic strain release along an

evolving segment of the Pacific–North America plate boundary: Earth and Planetary Science Letters, v. 304, no. 3-4, p. 565-576.

Gold, R. D., Cowgill, E., Arrowsmith, R. J., Gosse, J. C., Chen, X., and Wang, X. F., 2009, Riser diachroneity, lateral erosion, and uncertainty in rates of strike-slip faulting: A case study from Tuzidun along the Altyn Tagh Fault, NW China: Journal of Geophysical Research, v. 114, no. B4, p. 47.

Gosse, J. C., and Phillips, F. M., 2001, Terrestrial in situ cosmogenic nuclides: theory and application: Quaternary Science Reviews, v. 20, p. 1475-1560.

Greene, R. C., Stewart, J. H., John, D. A., Hardyman, R. F., Silberling, N. J., and Sorensen, M. L., 1991, Geologic map of the Reno 1 by 2 Quadrangle: Nevada and California: US Geological Survey Miscellaneous Field Studies Map MF-2154-A, scale, v. 1, no. 250,000.

Haddon, E. K., Amos, C. B., Zielke, O., Jayko, A. S., and Bürgmann, R., 2016, Surface slip during large Owens Valley earthquakes: Geochemistry, Geophysics, Geosystems, v. 17, no. 6, p. 2239-2269.

Hammond, W. C., Blewitt, G., and Kreemer, C., 2011, Block modeling of crustal deformation of the northern Walker Lane and Basin and Range from GPS velocities: Journal of Geophysical Research, v. 116, no. B4, p. B04402.

Harden, J. W., Taylor, E. M., Hill, C., and Mark, R. K., 1991, Rates of soil development from four soil chronosequences in the southern Great Basin: Quaternary Research, v. 35, p. 383-399.

Hardyman, R. F., 1980, Geologic Map of the Gillis Canyon Quadrangle, Mineral County, Nevada. U.S. Geological Survey Map, I-1237.

Hardyman, R. F., Ekren, E. B., and John, D. A., 2000, Evidence for Cenozoic dextral displacement across the Walker Lane, west central Nevada: Geological Society of America Abstracts with Programs, v. 32, no. 7, p. 105.

Hardyman, R. F., and Oldow, J. S., 1991, Tertiary tectonic framework and Cenozoic history of the central Walker Lane, Nevada, in Raines, G. L., Listle, R. E., Schafer, R. W., and Wilkinson, W. H., eds., Geology and ore deposits of the Great Basin: Reno, Nevada, geological Society of Nevada Symposium Proceedings, v.1, p, 279 - 301.

Jonsson, S. Zebker, H., Segall, P., Amelung, F., 2002, Fault slip distribution of the 1999 Mw 7.1 Hector Mine, California, earthquake, estimated from satellite radar and GPS measurements: Bulletin of the Seismological Society of America, v. 92, no. 4, p. 1377-1389.

Koehler, R. D., and Wesnousky, S. G., 2011, Late Pleistocene regional extension rate derived from earthquake geology of late Quaternary faults across the Great Basin, Nevada, between 38.5 N and 40 N latitude: Geological Society of America Bulletin, v. 123, no. 3-4, p. 631-650.

Kreemer, C., Hammond, W. C., Blewitt, G., Holland, A. A., and Bennett, R. A., A. 2012, Geodetic Strain Rate Model for the Pacific-North America Plate

Boundary, Western United States. Nevada Bureau of Mines and Geology, Map 178.

Lal, D., 1987, Cosmogenic nuclides produced in situ in terrestrial solids: Nuclear Instruments and Methods in Physics Research. Section B, Beam Interactions with Materials and Atoms, v. 29 (1/2), p. 238 - 245.

Li, X., Huang, W., Pierce, I. K., Angster, S. J., and Wesnousky, S. G., 2017, Characterizing the Quaternary expression of active faulting along the Olinghouse, Carson, and Wabuska lineaments of the Walker Lane: Geosphere, v. 13, no. 6, p. 2119-2136.

Lifton, N. A., Sato, T., and Dunai, T. J., 2014, Scaling in situ cosmogenic nuclide production rates using analytical approximations to atmospheric cosmic-ray fluxes: Earth and Planetary Science Letters, v. 386, p. 149-160.

Marrero, S. M., Phillips, F. M., Borchers, B., Lifton, N. A., Aumer, R., and Balco, G., 2016, Cosmogenic nuclide systematics and the CRONUScalc program: Quaternary Geochronology, v. 31, no. C, p. 160-187.

Murray, A. S., and Wintle, A. G., 2000, Luminescence dating of quartz using an improved single-aliquot regenerative-dose protocol: Radiation measurements, v. 32, no. 1, p. 57-73.

Oldow, J. S., Alken, C. L. V., Hare, J. L., Ferguson, J. F., and Hardyman, R. F., 2001, Active displacement transfer and differential block motion within the

central Walker Lane, western Great Basin: Geological Societry of America, v. 29, no. 1, p. 19-22.

Owen, L. A., Frankel, K. L., Knott, J. R., Reynhout, S., Finkel, R. C., Dolan, J. F., and Lee, J., 2011, Beryllium-10 terrestrial cosmogenic nuclide surface exposure dating of Quaternary landforms in Death Valley: Geomorphology, v. 125, no. 4, p. 541-557.

Orr. E., Owen, L., Murari, M., Saha, S., Caffee, M. 2017, The timing and extent of Quaternary glaciation of Sok, northern Zanskar Range, Transhimalaya, of northern India. Geomorphology, v. 284, p. 142-155

Snyder, S.L. and Duval, J.S., 2003, Design and Construction of a Gamma-ray Spectrometer System for Determining Natural Radioelement Concentrations in Geological Samples at the U.S. Geological Survey in Reston, Virginia. U.S. Geological Survey Open File Report 03-029.

Soil Survey Division Staff, 1993, Soil survey manual. United States Department of Agriculture Handbook No. 18, p. 437.

Stewart, J. H., 1980, Geology of Nevada: A discussion to accompany the Geologic Map of Nevada: Nevada Bureau of Mines and Geology Specitial Publication 4, p. 1-14.

Stone, J. O., 2000, Air pressure and cosmogenic isotope production: Journal of Geophysical Research: Solid Earth, v. 105, no. B10, p. 23753-23759.

Stone, J. O., Allan, G. L., Fifield, L. K., and Cresswell, R. G., 1996, Cosmogenic chlorine-36 from calcium spallation: Geochemical et Cosmochimica Acta, v. 60, no. 4, p. 679-692.

Surpless, B. E., 2008, Modern strain localization in the central Walker Lane, western United States: Implications for the evolution of intraplate deformation in transtensional settings: Tectonophysics, v. 457 (3-4), p. 239-253.

Thatcher, W., Foulger, G. R., Julian, B. R., and Svarc, J., 1999, Present-day deformation across the Basin and Range province, western United States: Science, v. 283, p. 1714 - 1718.

Unruh, J., Humphrey, J., Barron, A., 2003, Transtensional model for the Sierra Nevada frontal fault system, eastern California: Geology, v. 31, no. 4, p. 327 - 330

Vermeesch, P., 2009, RadialPlotter: A Java application for fission track, luminescence and other radial plots: Radiation Measurements, v. 44, no. 4, p. 409-410.

Wells, D. L., and Coppersmith, K. J., 1994, New Empirical Relationships Among Magnitude, Rupture Length, Rupture Width, Rupture Area, and Surface Displacement: Bulletin of the Seismological Society of America, v. 84, no. 4, p. 974-1002.

Wesnousky, S. G., 2005a, Active faulting in the Walker Lane: Tectonics, v. 24, no. 3.

Wesnousky, S. G., 2005b, The San Andreas and Walker Lane fault systems, western North America: transpression, transtension, cumulative slip and the structural evolution of a major transform plate boundary: Journal of Structural Geology, v. 27, no. 8, p. 1505-1512.

Wesnousky, S. G., 2008, Displacement and Geometrical Characteristics of Earthquake Surface Ruptures: Issues and Implications for Seismic-Hazard Analysis and the Process of Earthquake Rupture: Bulletin of the Seismological Society of America, v. 98, no. 4, p. 1609-1632.

Wesnousky, S. G., Bormann, J. M., Kreemer, C., Hammond, W. C., and Brune, J. N., 2012, Neotectonics, geodesy, and seismic hazard in the Northern Walker Lane of Western North America: thrty kilometers of crustal shear and no strike-slip?: Earth and Planetary Science Letters, v. 329-330, no. C, p. 133-140.

Wesnousky, S. G., and Caffee, M. W., 2011, Range-bounding normal fault of Smith Valley, Nevada: Limits on age of last surface-rupture earthquake and late Pleistocene rate of displacement: Bulletin of the Seismological Society of America, Vol. 101, No. 3.

Zechar, J. D., and Frankel, K. L., 2009, Incorporating and reporting uncertainties in fault slip rates: Journal of Geophysical Research, v. 114, no. B12, p. B12407.

Zielke, O., Klinger, Y., and Arrowsmith, R. J., 2015, Fault slip and earthquake recurrence along strike-slip faults — Contributions of high-resolution geomorphic data: Tectonophysics, v. 638, no. C, p. 43-62.

Appendix A - Lab Procedures and Sample Preparation

Steps and Lab Procedures for ^{10}Be sample processing

Lab ^{10}Be processing of sediment and rock samples collected in the field was performed at the University of Cincinnati. For the ^{10}Be processing, sediment samples for were sieved to obtain the 250 – 500 μm size fraction. All but one, Mina 1 Site on the Benton Spring fault, produced a sufficient amount of quartz at the end of sieving. For Mina 1, the 500μm – 2mm sample fraction size was crushed and added to the 250 – 500 um size fraction for all profile samples. Four acid leaches were used to further process the samples including; aqua regia for >9 hrs, one 5% HF/HNO_3 leach for ~24 hrs, one 100% HF for <1 hr (to remove "quartz coating"), and one 1% HF/HNO leach for 24 hrs. An atomic absorption spectrometry (AAS) Beryllium carrier was added to the pure quartz. The quartz was then dissolved in 49% HF and then passed through anion and cation exchange columns along with chemical blanks to extract $Be(OH)_2$. The $Be(OH)_2$ was oxidized through ignition at 750 - 1000 ^{0}C and mixed with Nb Powder and loaded in steel targets for measurement. ^{10}Be concentrations were measured by accelerator mass spectrometry at Purdue University PRIME lab. Detailed for standard, blanks, and age calculations are shown in Table 1 of manuscript.

Approximately 80 to 100g of each remaining sample was leached for 12 hr in 70% 2.0 M HNO_3. Samples were then decanted and rinsed using deionized water and then dried. Samples were weighed and then spike with ^{35}Cl and

measured again before being dissolved in a HF/70% HNO_3 solution. AgCl was the precipitated through the addition of 0.15M HNO_3.

Steps and Lab Procedures for ^{36}Cl sample processing

The ^{36}Cl samples were also processed at the laboratories at University of Cincinnati. Sediment samples were first sieved to obtain the 2mm to 250μm fraction, which was then crush and sieved again to obtain the 125 – 250μm size fraction. The four boulder samples at site PS were also crushed and sieved to obtain the 125 – 250μm size fraction. Aliquots of each sample were sent to Bureau Veritas Commodities Canada Ltd. for analysis of major elements and U and Th as well as gamma emission spectrometry of B and Gd. Approximately 80 to 100g of each remaining sample was then processed at UC following the standard procedure outlined in (Zreda, 1994). Processed samples were sent to PRIME Lab at Purdue for AMS analysis of the $^{36}Cl/^{35}Cl$ ratio and these results are provided in Table 2 in manuscript.

Steps and Lab Procedures for OSL sample processing

The tube was carefully opened in the laboratory and the sediment was removed in the following way: 1) the sediment present at the extremities of the tubes (~5 cm for each end), was removed, separated, and kept aside for water content and dose-rate measurements while 2) the sediment at the center of the tube was removed and reserved for the OSL. The sample corresponding to the extremities of the tubes, was weighted, fully dried and weighted again, to

estimate their water content. An unbiased selection of the sample was crushed with an agate mill and sent to a laboratory (WHICH) for chemical analysis, in order to obtain U, Th, K and Rb concentrations, needed for dose-rate (DR) determinations. The sediment for OSL was pretreated with 10% HCl (hydrochloric acid) and then with 10% H_2O_2 (hydrogen peroxide) to remove carbonates and organic. The sample was then rinsed with DIW (deionized water), dried at temperatures ≤40°C, and sieved. In order to etch the quartz surface grains and simultaneously dissolve feldspars and other existent silicates, the 90-150 µm fraction was treated with 48% HF (hydrofluoric acid) for 60 minutes, rinsed with DIW and treated with 38% HCl for about 40 minutes to remove any fluorides left by the HF dissolution in the sample. Both processes were done in a magnetic stirring plate, so that the sample was constantly stirred. The sample was then rinsed with DIW, dried and subjected to a magnetic separation by a variable magnetic field (Franz isodynamic magnetic separator), to remove heavy minerals (generally magnetic) from the sample and grains with magnetic inclusions. After all referred laboratory treatments, aliquots for each sample were subjected to IRSL and OSL to test for feldspar presence and evaluate quartz quality; when necessary, the etching step was repeated.

For the dose equivalent (DE) measurements, we measured several aliquots in multi-grain steel disks in an automated Risø TL-DA-20 OSL reader. The single aliquot regeneration (SAR) method of Murray and Wintle (2000) was used to determine the equivalent dose (DE) for age estimation.

Table A1. Soil Descriptions for cosmogenic profiles

Horizon [a]	Depth (cm)		Color [b]		Texture [c]	Size (% wt)			Structure [d]	Consistency [e]		CaCo3, Effervescence [f]	Roots [g]	Lowest Boundary [h]
	Top	Base	Dry	Moist		Sand	Silt	Clay		Dry	Wet			
IH Profile (38.579, -118.207)														
Av	0	7	10YR 6/3	10YR 5/3	sl	54	30	16	2cbk	lo	ss	s1	vf1	as
Bw	7	18	10YR 6/4	10YR 5/4	ls	82	10	8	0	lo	ns	w1	vf1	gs
Ck	18	90	10YR 7/3	10YR 5/3	ls	80	14	6	0	lo	ns	w1	vf1l	ds
C	90	170	10YR 7/3	10YR 5/3	s	88	8	4	0	lo	ns	a	vf1l	
GDN (38.579, -118.314)														
Av	0	10	10YR 7/3	10YR 5/3	c	37	23	40	2cbk	sh	s	es1	vf1	as
Bw	10	35	10YR 6/6	10YR 5/4	sl	71	11	18	1fgr	lo	ns	es1	vf1l	aw
Bwk	35	45	10YR 7/4	10YR 6/4	sl	75	17	8	0	lo	ns	es1	vf1l	aw
Ck	45	175	10YR 6/4	10YR 5/6	ls	83	7	10	0	lo	ns	s1	vf1l	
GDS (38.574, -118.211)														
Av	0	11	10YR 7/2	10YR 6/4	scl	53	15	32	2vcbk	lo	ns	s1	f1	as
Bw1	11	30	10YR 7/3	10YR 5/4	sl	69	13	18	1vfgr	lo	ns	s1	f1	gs
Bw2	30	50	10YR 7/2	10YR 5/6	ls	84	6	10	1vfgr	lo	ns	s1	f1	gs
Ck	50	170	10YR 6/2	10YR 5/4	ls	80	10	10	0	lo	ns	sl1	f1l	
Mina1 (38.4168, -118.074)														
Av	0	10	10YR 7/3	10YR 7/3	cl	40	30	30	2msbk	h	ps	es	nd	as
Bw	10	25	10YR 6/6	10YR 4/4	ls	84	8	8	1vfgr	lo	ns	es	nd	di
Bk	25	65	10YR 6/4	10YR 5/6	s	88	8	4	1vfsbk	lo	ns	vs2	nd	gi
Ck	65	100	10YR 5/6	10YR 5/8	s	91	5	4	0	lo	ns	es	nd	
PSP1 (38.7241, -118.1592)														
Av	0	7	10YR 4/3		l	43	32	25	2mbk/pl	sh	s	e	nd	aw
Bt	7	23	10YR 5/4	not	c	40	18	42	1fsbk	so	ss	ne	nd	cw
Bk	23	120	10YR 7/2	recorded	ls	80	14	6	2msbk	h	ns	vs2	nd	d
Ck	120	140	10YR 6/2		ls	78	16	6	0	lo	ns	vs2	nd	
IH-South (38.4705, -118.2296)														
Av	0	4	10YR 6/3	10YR 5/3	sl	Particle size analysis			2cbk	so	ss	s1	vf1	aw
Bw	4	14	10YR 6/4	10YR 4/4	Ls	not performed			1mgr	lo	ns	w1	vf1	gw
Ck	14	100	10YR 6/4	10YR 4/4	ls	(Textures determined from field analysis)			0	lo	ns	w1	vf1	

[d] Descriptions and abbreviations follow criteria in soil Survey Division Staff (200?)
[b] From Munsell Soil Color Charts (1990)
[c] g, gravel; vg, very gravelly;. Eg, extremely gravelly; c, cobbly or cobbles; f, flaggy or flagstone; s, sand; ls, loamy sand; sl, sandy loam; scl, sandy clay loam; sil, silt loam; l, loam
[d] (Grade) 0, structureless; 1, weak; 2, moderate; 3, strong (Size) vf, very fine; f, fine; m, medium; c, coarse; vc, very coarse; pl, platy; pr, prismatic; cor, columnar; bk, blocky; abk, angular blocky; gr, granular; cr, crumb; sg, single grain; m, massive; sbk, subangular blocky
[e] Dry: lo, loose; so, soft; sh, slightly hard; h, hard. Moist: lo, loose; vfr, very friable; fr, friable; fi, firm. Wet: ns, non-sticky;, ss, slightly sticky; s, sticky; po, non plastic; ps, slightly plastic; p, plastic; NA, not applicable; ND, not determined
[f] Matrix: e, slightly effervescent; es, strongly effervescent; vs, violently effervescent. Clasts: 1, stage 1; 2, stage 2; 3, stage 3; 4, stage 4.
[g] vf, very fine; f, fine; m, medium; l, localized; 1, few; 2, common; 3, many; ir, irregular; v, vesicular, NA, not applicable; ND, not determined.
[h] a, abrupt; c, clear; g, gradual; d, diffuse; s, smooth; w, wavy; I, irregular; ND, not determined

CHAPTER 3

Quaternary faults and folds of the northern Sacramento Valley: Contraction in the northern Sierra and southern Cascadia transition zone

Stephen Angster, Steven G. Wesnousky, Paula Figueirdo,

Lewis A. Owen, Thomas Sawyer

Abstract

The northern Sacramento Valley is located at the transition between the Sierra Nevada and Cascadia tectonic provinces. Observations from magnetic anomaly maps, 2D seismic reflection profiles, mapping of Quaternary units, and longitudinal fluvial terrace profiles provide evidence within the transition zone of late Pleistocene contraction oriented in a northerly direction. The observations encompass several east-west trending structures in the valley including: 1) the Red Bluff fault, 2) the Inks Creek fold system, 3) the Battle Creek fault zone, and 4) the Bear Creek fault. Radiocarbon and OSL ages on deformed strath terraces indicate elevated rates of ~1.5 mm/yr of bedrock incision along the Sacramento River during the last ~30 ka. The higher incision rates are at least partially due to tectonic uplift associated with the Inks Creek fold system and Red Bluff fault. The degree of folding and ages of the folds indicates horizontal shortening across this zone could be on the order of ~1 mm/yr. Faults associated with the folds generally show north-side-up and provide plausible evidence for left-lateral motion associated with the Battle Creek fault zone and the Bear Creek fault. This study provides evidence for late Quaternary transpressional strain accommodation within the northern Sacramento Valley, marking the southern most extent of the northern Sierra and southern Cascadia transition zone. Implications of these finding relate to a reevaluation of the seismic hazard of the region.

Introduction

The northern Sacramento Valley is located at the transition between the Sierra Nevada and Cascadia tectonic provinces (Figure 1a). Geodesy shows the area of transition to be characterized by general north-south contraction (Hammond and Thatcher, 2005) and seismology records the presence of localized transpressional shear strain release within the northern part of the Sierra Nevada (Unruh and Humphrey, 2017). The deformation is attributed to relative motions between the more rapid northwest-translation of the Sierra Nevada batholith and clockwise rotation of the crust in northernmost California and Oregon, defining the Oregon Coast Block (Figure 1a; (Wells et al., 1998; Wells and Simpson, 2001; Williams et al., 2006; Humphreys and Coblentz, 2007). Prior geologic mapping (Helley et al., 1981; Blake et al., 1999) has shown the presence of several east-west oriented structures within the northern Sacramento Valley including: 1) the Red Bluff fault, 2) Inks Creek fold system, 3) the elongated Hooker Dome structure, 4) the Battle Creek fault zone, and 5) the Bear Creek fault (Figure 1b). These east-west structures mark an abrupt change in structural fabric from the massive Sierra Nevada batholith and northwest trends of the Chico monocline and Corning fault immediately to the south (Figure 1). The purpose of this study is to consider whether the east-west structures are currently active in accommodating strain within the transition zone between the northern part of the Sierra Nevada and southern Cascadia.

We map geologic structure and date deformed Quaternary landforms to asses the evidence for Quaternary deformation. Observations of fault style and recency are drawn from previous regional maps of the area, magnetic anomaly maps, vintage 2-D seismic reflection profile images, and lidar. Aspects of mapping include development of a detailed Quaternary surficial map along the course of the Sacramento River where it traverses the field area, construction of topographic and longitudinal profiles of the river and adjacent fluvial terraces, and radiocarbon and optically stimulated dating of fluvial terrace deposits. The sum of observations are used to quantify bedrock uplift and place first-order constraints on fault slip rates associated with the east-striking faults and folds that cross the river, and conclude the presence of active Quaternary deformation in the northern Sacramento Valley.

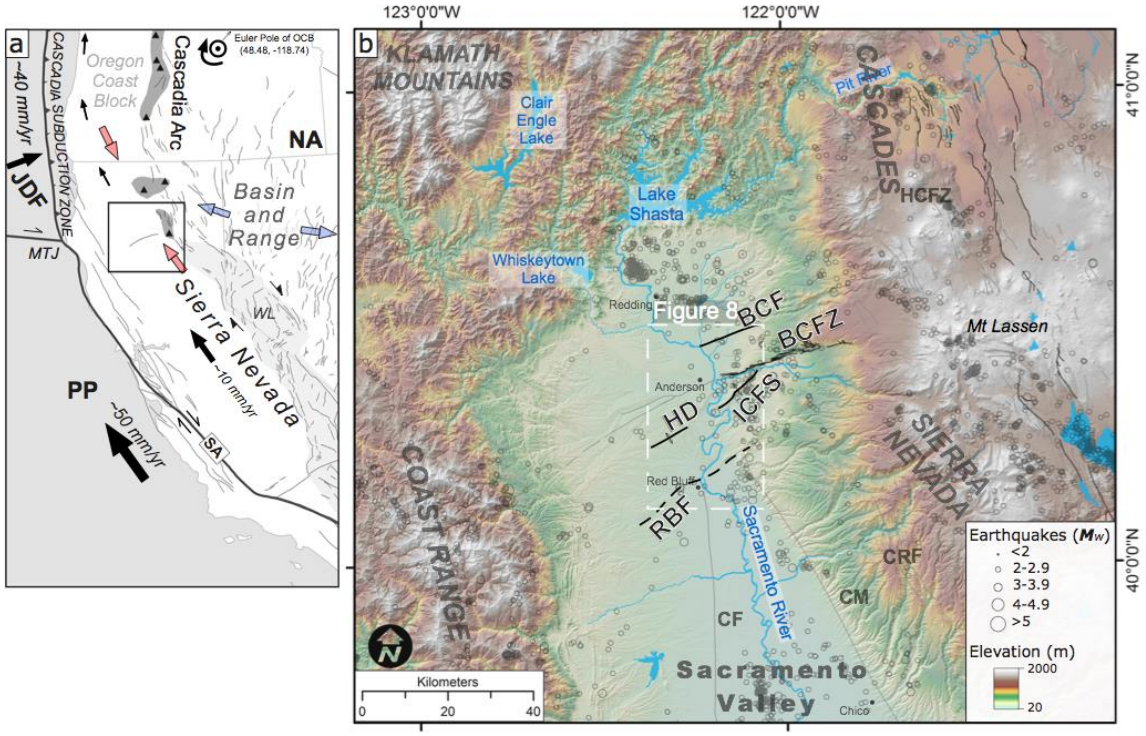

Figure 1. (inset) Regional tectonic setting of western North America. Thin grey lines are simplified traces of Quaternary active faults (USGS Quaternary fault and fold database). Solid black arrows show general contemporary motion defined by geodetic velocities. Hollow grey arrow represent contemporary regional strain field (Hammond and Thatcher, 2005). Labeled tectonic plates include Juan De Fuca Plate (JDFP), Pacific Plate (PP), and North America Plate (NA) with boundaries (SA – San Andreas fault; MTJ – Mendocino Triple Junction). Intraplate blocks and tectonic provinces include the Oregon Coast Block (OCR), Sierran Microplate (SN), Walker Lane shear zone (WL), and the Basin and Range (B&R). Main map displays hillshade relief and structure map of the northern Sacramento Basin. Includes Quaternary active faults as black lines and late-Cenozoic structures in grey (CF – Corning fault; CM – Chico Monocline). Faults focused on in this study include the Red Bluff fault (RBF), Hooker Dome (HD), Inks Creek Fold System (ICFS), the Battle Creek Fault Zone (BCFZ), and the Bear Creek Fault (BCF).

Prior Mapping of East-West Trending Structures in the northern Sacramento Valley

The northern Sacramento Valley is characterized by elevated incised topography that is encircled by the Coast Range to the west, Klamath Mountains to the northwest and north, and the northern Sierra and Mt. Lassen volcanic region along its eastern boundary (Figure 1b). The surrounding mountains comprise the expansive watershed of the Sacramento River, which flows south through the Sacramento Valley (Figure 1b). Before the construction of the Shasta Dam (1944), the free-flowing river experienced large widespread seasonal fluctuations in flow, ranging from ~85 m^3/s in the late summer to over ~2260 m^3/s in the late winter months.

The major late Cenozoic structures in the Sacramento Valley include the northwest trending Corning fault and Chico monocline (Harwood, 1984; Helley and Jaworowski, 1985), which parallel the Sierra Nevada and terminate at a zone, marked by the Red Bluff fault, of mapped east-west striking faults and folds

(Figure 1b). Prior geophysical studies have documented ~140 m of late Cenozoic down-to-south displacement of the base of Pliocene rocks resulting from folding or faulting on the Red Bluff fault (Blake et al., 1999). Major right-lateral slip on the Red Bluff fault has been inferred from tentative correlations of observed offset magnetic and gravity anomalies within the basement, however no surficial observations have been made to support this sense of motion (Griscom, 1973; Blake et al., 1999).

The prominent escarpment of the Battle Creek fault zone extends to the northeast towards Mount Lassen, progressively increasing in height (Figure 2), forming up to ~485 m of topographic relief near its eastern end. The early mapping efforts of Helley et al. (1981) describe down-to-south displacements within the basal contacts of the Quaternary-aged Coleman Forebay basalt and Red Bluff fanglomerate unit across the Battle Creek fault zone, measuring ~373 and ~127 m, respectively (Figure 2). On this basis, the east-striking Battle Creek fault zone is included in the USGS Quaternary fault and fold database as an active normal fault. The designation conflicts with the current geodetic field as a fault of this orientation would be expected to be reverse (e.g. Unruh and Humphrey, 2017).

Helley et al. (1981) recognized that the large meanders of the Sacramento River and accompanying narrowing of the channel are spatially correlated to an anticline-syncline pair of the Inks Creek fold system, located between the towns of Cottonwood and Red Bluff (Figure 2). The anticline axis of the Inks Creek fold system is expressed in Pliocene strata and plunges to the SW, while the

synclinal axis strikes along Inks Creek on the south side on the anticline (Figure 2). The anticlinal axes trends obliquely to and possibly merges with the Battle Creek fault zone to the northeast (Figure 2), suggestive of a genetic relationship (Harwood, 1984).

On the west side of the Sacramento River, Pliocene strata are arched over the Hooker Dome structure (Helley et al., 1981; Blake et al., 1999). Uplift of the elongated dome is presumably responsible for the dissected topography of the surrounding area and a drainage divide, which marks the axis of the Hooker Dome. Drainages to the south of the divide generally flow southeast (e.g., Blue Tent Creek) and those to the north of the divide (e.g., Hooker Creek) generally flow northeastward (Figure 1 and 2). An unconformity observed between the overlying 590 ± 20 ka Rockland Ash unit (Lanphere et al., 2017) and underlying erosional contact of the Quaternary Red Bluff Formation and Pliocene Tehama Formation exposed at Round Mountain (Figure 2) have been interpreted as evidence of Quaternary uplift associated with the Hooker Dome and Inks Creek fold system (Helley et al., 1981; Blake et al., 1999).

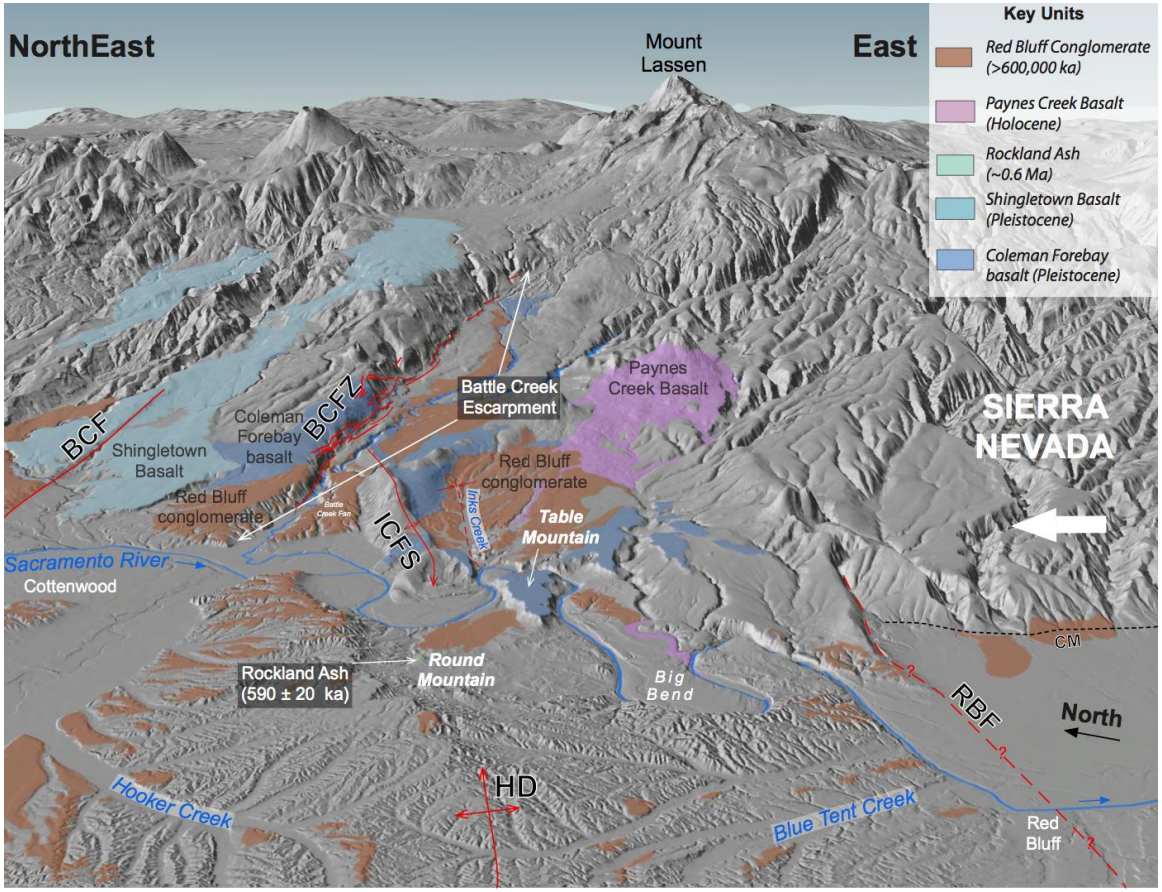

Figure 2. Oblique view looking eastward across study area. Topography is vertically exaggerated (~10x) to show relief. Structure labels are described in caption of Figure 1. Mapped Quaternary units from Blake et al., (1990) are shown in key in upper right. Other units remain transparent, exposing 10-meter DEM hillshade image below. Large white arrow shows translation direction of Sierra Nevada block.

The Bear Creek fault is the northern most mapped east-west trending structure within the northern Sacramento Valley and produces a well-expressed east-northeast trending fault scarp, characterized by higher topography on the northern side that displaces the Quaternary Shingletown basalt and truncates the Quaternary fanglomerate of the Red Bluff Formation (Figure 2; Blake et al., 1999). Blake et al. (1999) speculate that the Bear Creek fault structure may reflect pre-Neogene left-lateral displacement, accommodating early Cenozoic clockwise rotations of the Klamath Mountains and Oregon Coast block (Figure 1). There are no recent studies describing the geometry, genesis, or Quaternary activity of the Bear Creek fault.

Methods and Data

Geophysical-based datasets of the subsurface are used to assess the general style and relative age of deformation in the field area. Geologic and geomorphic relationships are further used to show the recency of deformation and absolute dating techniques are used to place age constraints on deformed terraces.

Prior Mapping

The early maps and observations of Helley et al. (1991) and Harwood and Helley (1987) produced within the northern Sacramento Valley are incorporated

in the most recent quadrangle map of Blake et al. (1999). I adapt the geologic unit contacts and structure lines from these prior maps and combine with a 10-m-resolution digital elevation model (DEM) acquired from the USGS National Elevation (https://nationalmap.gov/elevation.html) to make surficial observations of the study area.

Geophysical Data

Seismic reflection profile images and aeromagnetic data are used to assess subsurface evidence of faults and folds. The aeromagnetic data used comes from the dataset provided in the open file report of the integrated magnetic anomaly map of North America (Bankey et al., 2002). The data was downloaded from the USGS aeromagnetic archives (https://mrdata.usgs.gov/magnetic/) and consists of 1-km-grids constructed from numerous merged datasets. The map is representative of the total intensity of Earth's magnetic field at 305 m above the terrain with long-wavelength anomalies (>500 km) removed. Accuracies in the data set are suggested to be in the range of 1 to 10 nanotesla (nT) (Bankey et al., 2002).

Two unpublished industry seismic lines and profiles acquired from Pacseis Inc., with permission to publish as preprocessed images, are used to illustrate the subsurface structural and stratigraphic geometries associated with folds and faults and place relative age constraints of deformation. Due to the limitations of acquisition data and information, we are unable to register and migrate the data, thus the utility of the profiles to quantify depths and dips is limited. Interpretation

of subsurface geometries and structures are based on the observation of truncations, folding, and on-lapping geometries within the seismic reflectors following the approach outlined in Mitchum et al. (1977) and Prosser (1993). Interpretations of these profiles are compared with others that were made from proprietary seismic lines, interpret from migrated original data and generalized into a cross-section presented in the consulting report for the Cottonwood Creek project for the U.S. Army Corps of Engineers Sacramento District published in Tait et al. (1983).

Lidar Dataset and Quaternary mapping

A ~600 km^2 airborne lidar dataset was acquired from the California Department of Water Resources along the Sacramento River channel. Analysis of the dataset are performed on 0.5-m-resolution bare-earth DEM's to aid the mapping of Quaternary units and provides the basis to construct accurate topographic profiles of fluvial terraces along the river. Other topographic profiles are extracted from the 10-meter DEM for the portions of the study area not covered by the lidar dataset.

We follow the allostratigraphic framework developed for the northern Sacramento Valley and build on prior mapping and studies (e.g. Steele, 1980; Helley et al., 1981; Blake et al., 1999), adapting names and contacts of Plio-Pleistocene units. Lidar and field investigation along with standard mapping techniques are used to perform higher resolution mapping of younger terrace deposits along the Sacramento River. Different age units are assessed by

relative height to one-another, surficial characteristics within the lidar, and soil development observed from natural exposures.

Geochronology

Ages of terrace deposits are estimated from radiocarbon dating and optically stimulated luminescence (OSL) dating. Detrital charcoal samples were carefully collected from cut bank exposures along the river, placed in glass sampling tubes, and cleaned by removing large fragments of attached sediment. Samples were then sent to Beta Analytic Inc. for analysis, radiocarbon dating, and calibration following Talma and Vogel (1993) and Reimer et al. (2013). The OSL sample was obtained by hammering an opaque ~20 cm long plastic tube into the center of a freshly cleaned face of exposed fluvial sand. The tube was packed tight, taped, sealed, and later processed and measured in the Luminescence Geochronology Laboratory at University of Cincinnati. There, the OSL sample was prepared for measurement following the method described in Counts et al. (2015), and an automated Risø TL-DA-20 OSL reader was used for the OSL measurements and irradiation. An unbiased selection of the sample was sent to Actlab for chemical analysis of U, Th, and K concentrations following the procedure described in Snyder and Duval (2003) for dose rate determinations. Thirty-two aliquots were measured using the single aliquot regeneration (SAR) method of Murray and Wintle (2000). The Java application RadialPlotter of Verneesch (2009) was used to help determine statistically significant peaks

within the dose equivalent measurements. We use the weighted mean and minimum age model.

Fluvial Terrace Profiling

Longitudinal profiles of the mapped Quaternary terrace surfaces along the Sacramento River were constructed using the lidar dataset. River profiles were also constructed measuring distance downstream following the center of the river following the method of Merritts et al. (1994). Terrace surface elevations were projected to the center of the river so they follow the general migration path of the river during abandonment (Figure 3)**.** Uncertainty lies within this method where terrace surface points are incorrectly projected to the exact point on the river that they correspond to; however, this method allows for the projection of terrace surfaces points where large sinuosity's occur, and the river channel flows in the opposite general direction, whereas standard plotting of terrace surface points along a linear transect would overlap in this environment. The grade of the river through the study region is relatively low (~0.00077), thus elevation changes are minimal over small (<1 km) distances, decreasing the amount of uncertainty in this method. An additional element of uncertainty lies within the fluvial terrace surfaces, as they are inherently subject to differential erosion and deflation through time. To minimize this systemic uncertainty, we chose elevations to project to the river from terrace surfaces that appeared to be the least modified and deflated. Such surfaces are characterized by relatively finer grain sediments capping the terrace and have smooth continuous surfaces. As a result, this limits

the amount of projections per terrace, especially for the older more incised terraces, but allows for more consistency. The approximate uncertainty is about ± 0.5 m in elevation for our terrace surface projections.

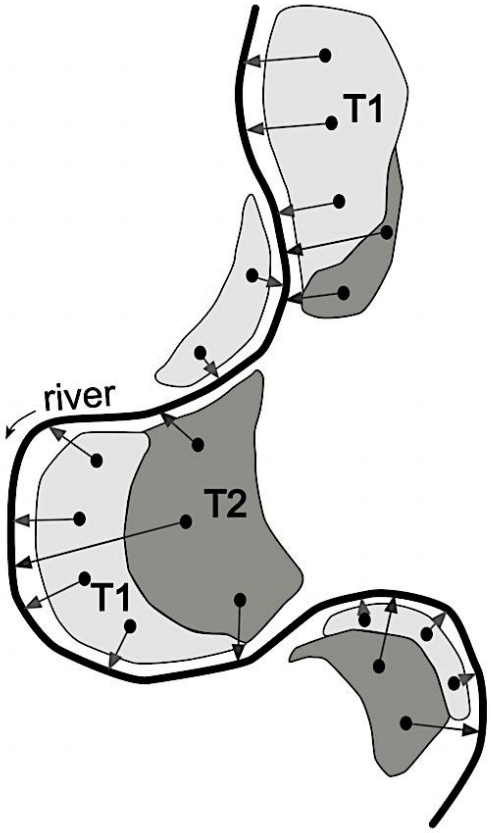

Figure 3. Method of projecting terrace surface elevations to river following Merritts et al. (1994). In this case, T1 represents the younger terrace and T2 is the older terrace. Black circles represent surface elevations that are projected following arrows to the river.

Observations

Aeromagnetics

Magnetic anomalies reflect localized disparities in Earth's magnetic field resulting from variations in the chemical composition or magnetic fluctuations within bodies of rock. Sharp variations within the magnetic field or steep gradients within the magnetic signal often reflect the presence of basement structures (e.g., Meghraoui, 1996). Abrupt magnetic gradients correspond to the location of the Battle Creek zone and Bear Creek faults (Figure 4). The region of highest magnetic intensity is juxtaposed to a region of the lowest magnetic intensity and exhibits an apparent left-lateral offset across the Battle Creek fault zone (Figure 4). A similar apparent left-lateral offset is evident in the magnetic signal at the west end of the Bear Creek fault (black arrows in Figure 4). This may be explained by left-lateral, vertical, or a combination of both types of offset of bedrock in the subsurface.

A broad relative magnetic low appears to be in the same general location and on-trend with the elongated axis of the Hooker Dome structure (Figure 4). To the south, the Red Bluff fault appears to parallel and define the boundary between this relative low and a magnetic high at the very southern portion of the map (Figure 4). These relationships suggest that the Hooker Dome and Red Bluff faults are linked to deep-seated structures that warp and vertically offset bedrock in the subsurface.

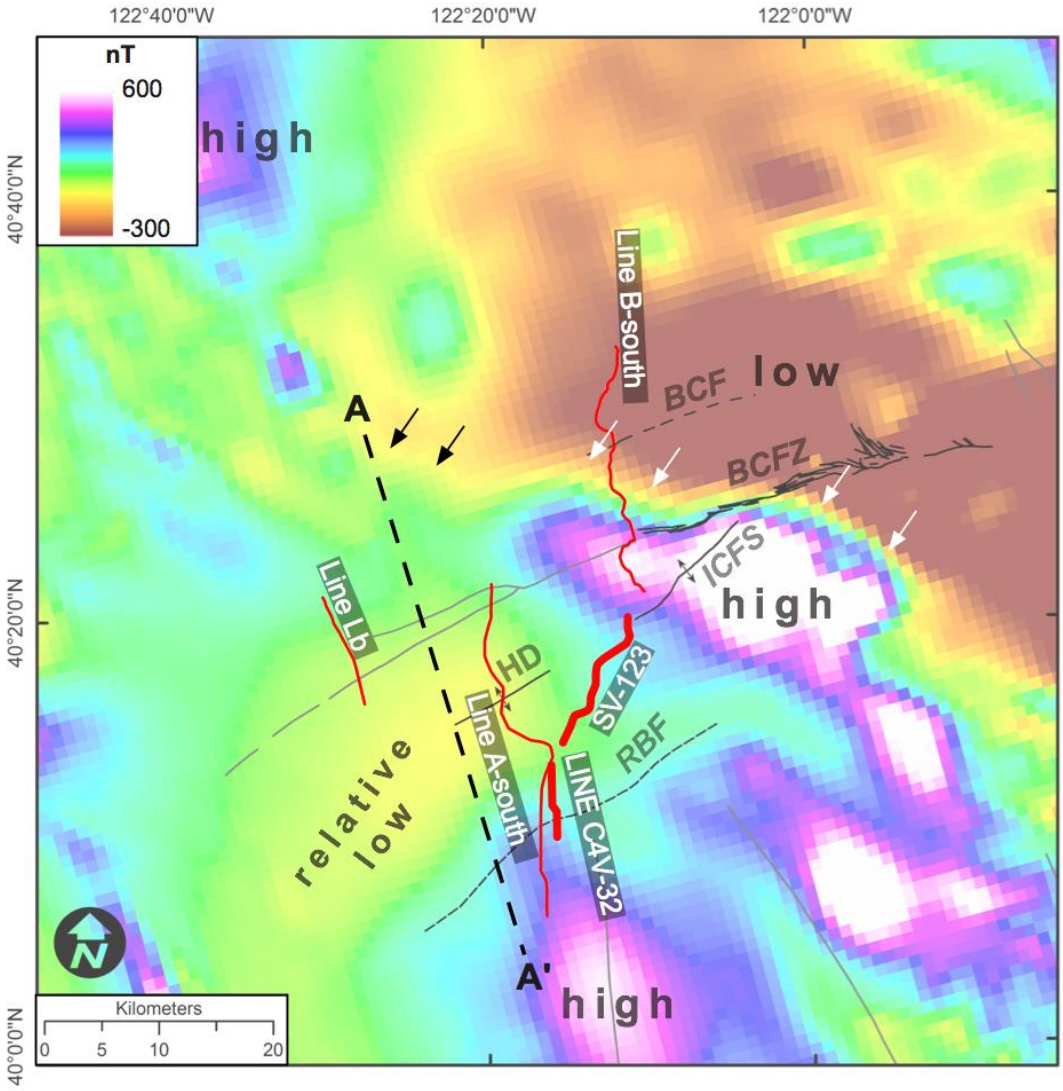

Figure 4. Magnetic anomaly map of study region and locations of seismic reflection profiles used in this study (white lines). Magnetic anomaly data is from USGS open file report of Daniels et al. (2002), showing the downloaded 5 km digital grids of study area, representing the magnetic field at 305 m above terrain with long-wavelength anomalies (>500 km) removed. Key in upper left shows color scheme and scale of nano tesla (nT) values for magnetic data. The thicker white lines (Line 4V-32 and SV-123) represent the reflection profiles interpreted in Figures 5 and 6. The thin white lines of Line Lb, Line A-south, and Line B-south are the proprietary reflection profiles used to generate the generalized cross-section (Associates et al., 1983) shown in Figure 10. Mapped surface traces of structural features are shown by black lines (BCF - Bear Creek fault; BCFZ - Battle Creek fault zone; IFCS - Inks Creek Fold system; HD - Hooker Dome; RBF - Red Bluff fault; CF - Corning fault; CM - Chico Monocline).

Seismic Stratigraphy and Structure

Seismic reflection profile LINE C4V-32 generally runs north-south and crosses the mapped trace of the Red Bluff fault (Figure 4). A parallel set of strong reflectors is evident at 0.6–0.7 s depth at the northern end of the profile (Figure 5b). These reflectors appear to be truncated, near the center of the profile, and are displaced downward to 0.7–1 s depth at the southern end of the profile (Figure 5). The overlying seismic stratigraphy is interpreted to exhibit layers that on-lap but do not continue over the scarp (Figure 5b). The reflectors are more continuous and exhibit folding in the form of a monocline at <5 sec depth. These upper reflectors step-down to the south and appear to be more separated from the lower truncated reflectors than on the north. The stratigraphy is interpreted to be the result of displacement on a blind low-angle north-dipping thrust fault that has accumulated growth strata within the footwall.

Reflection profile Line SV-123 runs along a southwest-northeast transect that crosses the eastern end of the magnetic relative low, just east of the elongated axis of the Hooker Dome structure (Figure 4). Faint discontinuous reflections are observed within the lower portion of the profile at 2.2–1.8 s (Figure 6b) and indicate south-side-down displacement. A much stronger reflector at 0.6–1 sec is almost continuous across the entire profile and is broadly folded near the center and more tightly folded at the southern end of the profile (Figure 6). Reflectors above this horizon, are discontinuous, diverge to the north, and are tightly folded near the southern end above the broad fold observed below.

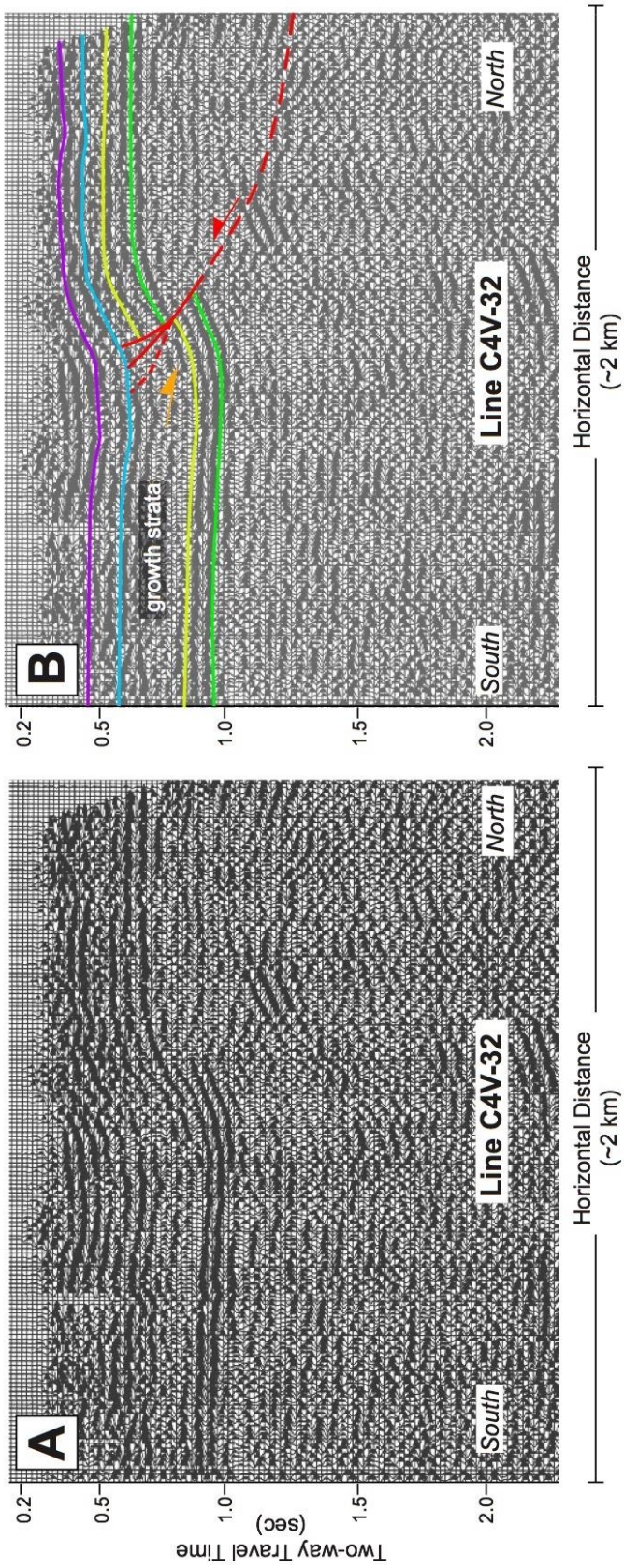

Figure 5. Seismic reflection profile LINE C4V-32. Uninterrupted (a) and interpreted (b) images of profile. Location of profile is shown in Figure 4. Red lines and arrow are representative of interpreted faults and associated motion. Orange arrows depict on-lap geometries. Other colored lines are key horizons discussed in text.

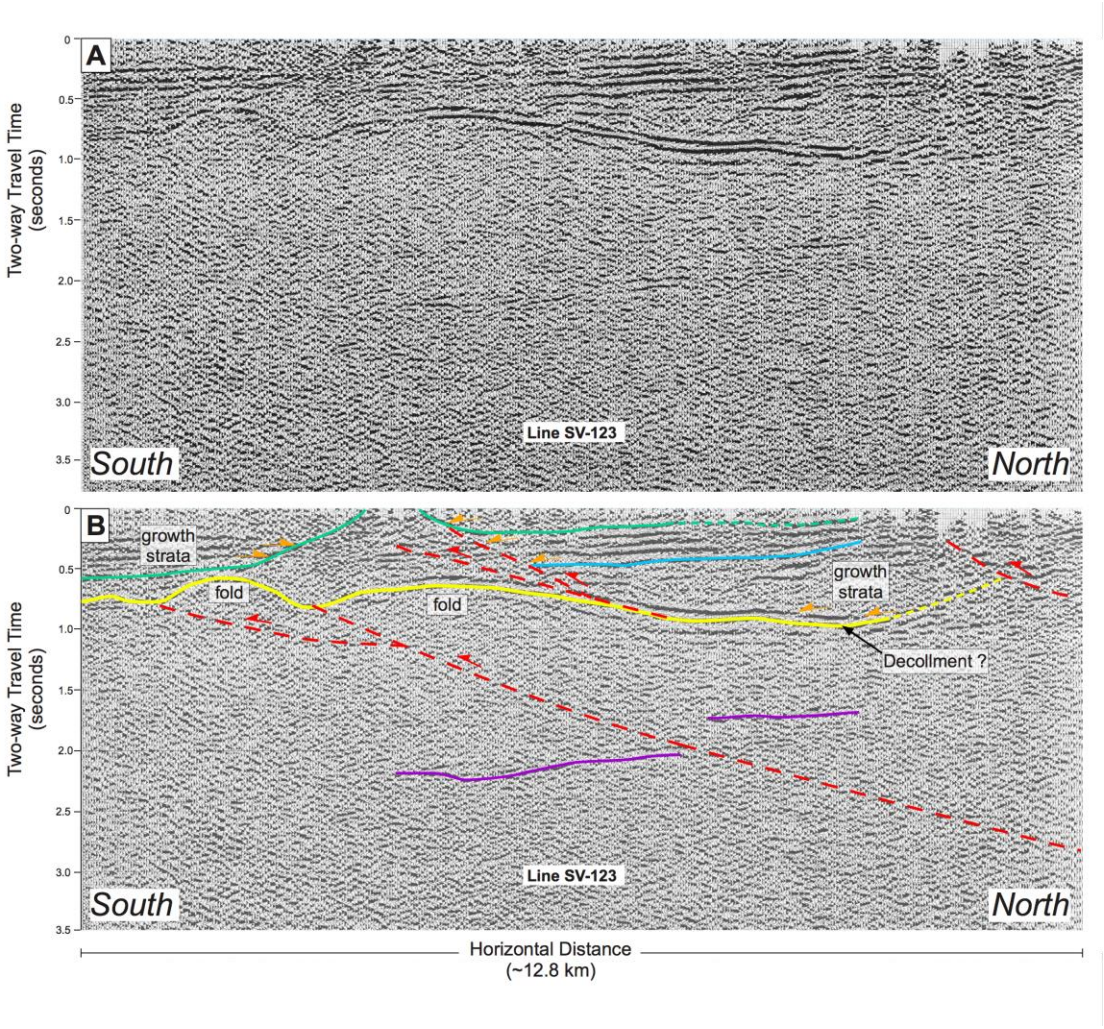

Figure 6. Seismic reflection profile LINE SV-123. Uninterrupted (a) and interpreted (b) images of profile. Location of profile is shown in Figure 4. Red lines and arrow are representative of interpreted faults and associated motion. Orange arrows depict on-lap geometries. Other colored lines are key horizons discussed in text.

Reflectors appear to on-lap and are interpreted as growth stratigraphy.

The sum of observations from this profile is interpreted to depict a series of north dipping blind thrust faults. The seismic stratigraphy at the northern end of the profile image is discontinuous and less apparent (Figure 6a), and the geometry of the strong reflector is less defined (yellow horizon; Figure 6a). The interpretation queries this reflector to fold upward to the north and is possibly truncated by a north-dipping fault (Figure 6b). These interpretations may suggest that the broad fold geometry in the subsurface are the result of south-vergent thrust faulting associated with the Hooker Dome, and the spatial relationship with the relative magnetic low (Figure 4), which this profile crosses, further suggest that these thrust faults continue to the basement.

The generalized cross-section (Figure 7) was constructed from prior interpretations (Tait et al., 1983) of proprietary seismic lines LB, line-south, and Line B (Figure 4). At the very northern end, the cross-section displays two relatively low-angle reverse faults that dip to the north and displace basement and mid-Cretaceous strata (Figure 7). These may likely be the western extension of the Bear Creek fault (Figure 4). To the south, the Battle Creek fault zone is a steep south-dipping fault that displaces basement and Cretaceous strata (Figure 7). On the northern footwall, the lower Cretaceous is missing (Figure 7), while in the hanging wall the lower Cretaceous overlays basement, forming a much thicker package of Cretaceous strata. This relationship suggests that the Battle Creek fault zone was active as a south-dipping normal fault during the Cretaceous. Above the fault zone,

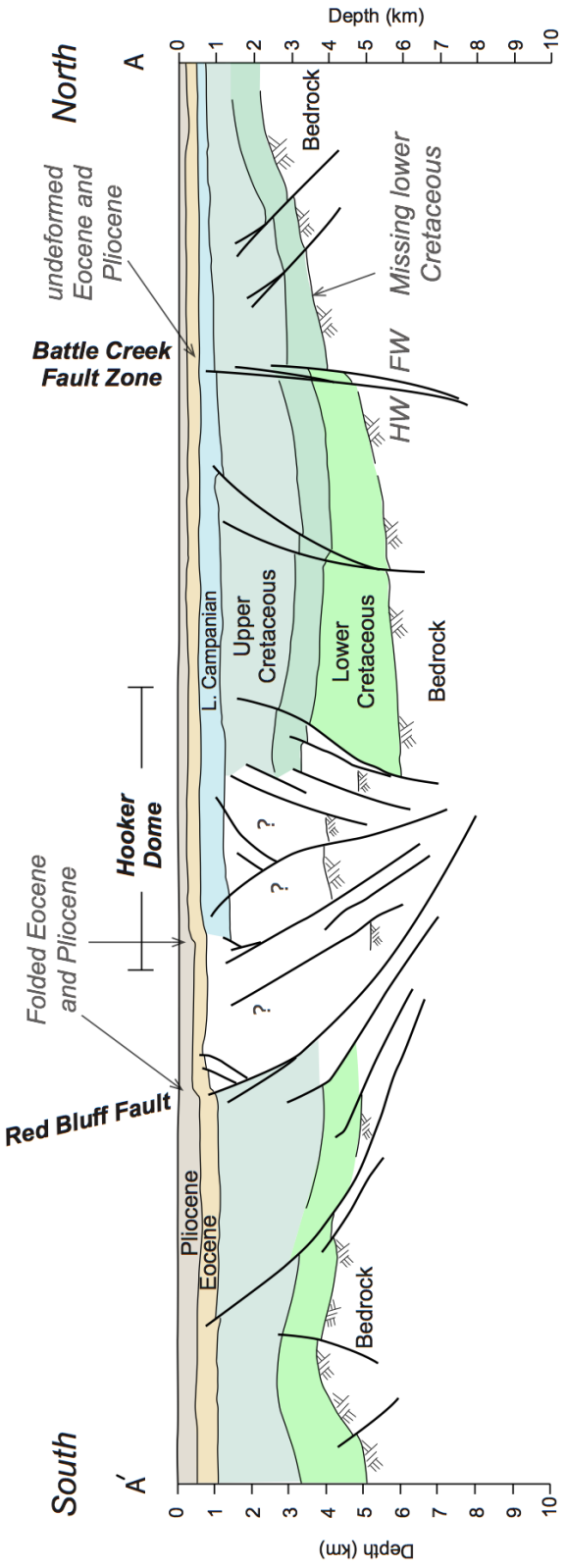

Figure 7. Generalized Cross-section from(Associates et al., 1983) consulting report. Cross Section was developed from interpretations of proprietary seismic reflection lines (Line Lb, Line A-south, and Line B-North) shown in Figure 4.

younger Eocene and Pliocene age strata are unfaulted and undeformed (Figure 7). To the south these same strata are folded above lower angle north-dipping, reverse faults, including the Red Bluff fault and those associated with the Hooker Dome. Beneath the Hooker Dome, the combination of steeper reverse faults resembles flower structure geometry, commonly attributed to shear displacement.

Quaternary Mapping

The major Quaternary fluvial deposits along the Sacramento River (Qrl, Qru, Qml, and Qmu; Figure 8) and volcanic units of the region (Qcb and Qsb; Figure 8) show evidence for contractional deformation. Pliocene and older units are considered to be bedrock and form the channel walls into which the Sacramento River channel is incised (Figure 8). The two major Pliocene formations can be differentiated by their location relative to the Sacramento River and erosional characteristics displayed in the hillshade. The alluvial units of the Tehama Formation lie on the west side of the river and are eroded by ephemeral streams reflecting a dendritic texture, while the volcanic derived units of the Tuscan Formation lie on the eastern side of the river and display much smoother surfaces (Figure 8).

There are four late Pleistocene to Holocene fluvial terrace units within the main channel of the Sacramento River that serve as datum’s helping to indicate recent deformation. The upper Modesto deposit (Qmu) forms the lowest terrace surfaces, sitting ~4 m above the modern river, and is considered to be Holocene

(Steele, 1980; Helley et al., 1981; Blake et al., 1999). The surfaces of these deposits are fresh, exhibiting muted bar and swale topography on the lidar and in the field, and soils are absent a B-horizon. This surface is occasionally flooded during flood stage of the Sacramento River. The lower Modesto deposits (Qml) are differentiated from the upper, as their surfaces sit relatively higher (1–2 m) above the Qmu surface and have a weak B-horizon within the deposit. The surface of this unit is rarely flooded, and is more commonly disturbed by agriculture activity, covered by various orchards, and displays smooth surface within the lidar data where undisturbed. The Modesto deposits are considered to be late Pleistocene to Holocene (Steele, 1980; Helley et al., 1981; Blake et al., 1999). Both of the Modesto terraces are generally fill terraces, but can be considered strath terraces within the meandering section of the Sacramento River where the bedrock contact is exposed, usually close to modern river level. The surfaces of the upper and lower members of the Riverbank deposits, Qru and Qrl, respectively, sit at 7–10 m above the river. Riverbank deposits are inset within the bedrock wall of the river channel, forming a sharp, deep fluvial cut within the Pliocene bedrock. Soils within these deposits have Bt-horizons, show significant rubification, and characteristically contain a duripan. The older Qrl surface is differentiated from the Qru surface by its higher elevation, greater incision, and relatively better-developed soil. Based on the prior correlations of Steele (1980) the upper (Qru) and lower (Qrl) riverbank deposits have been estimated to be 40–125 and 200–250 ka, respectively.

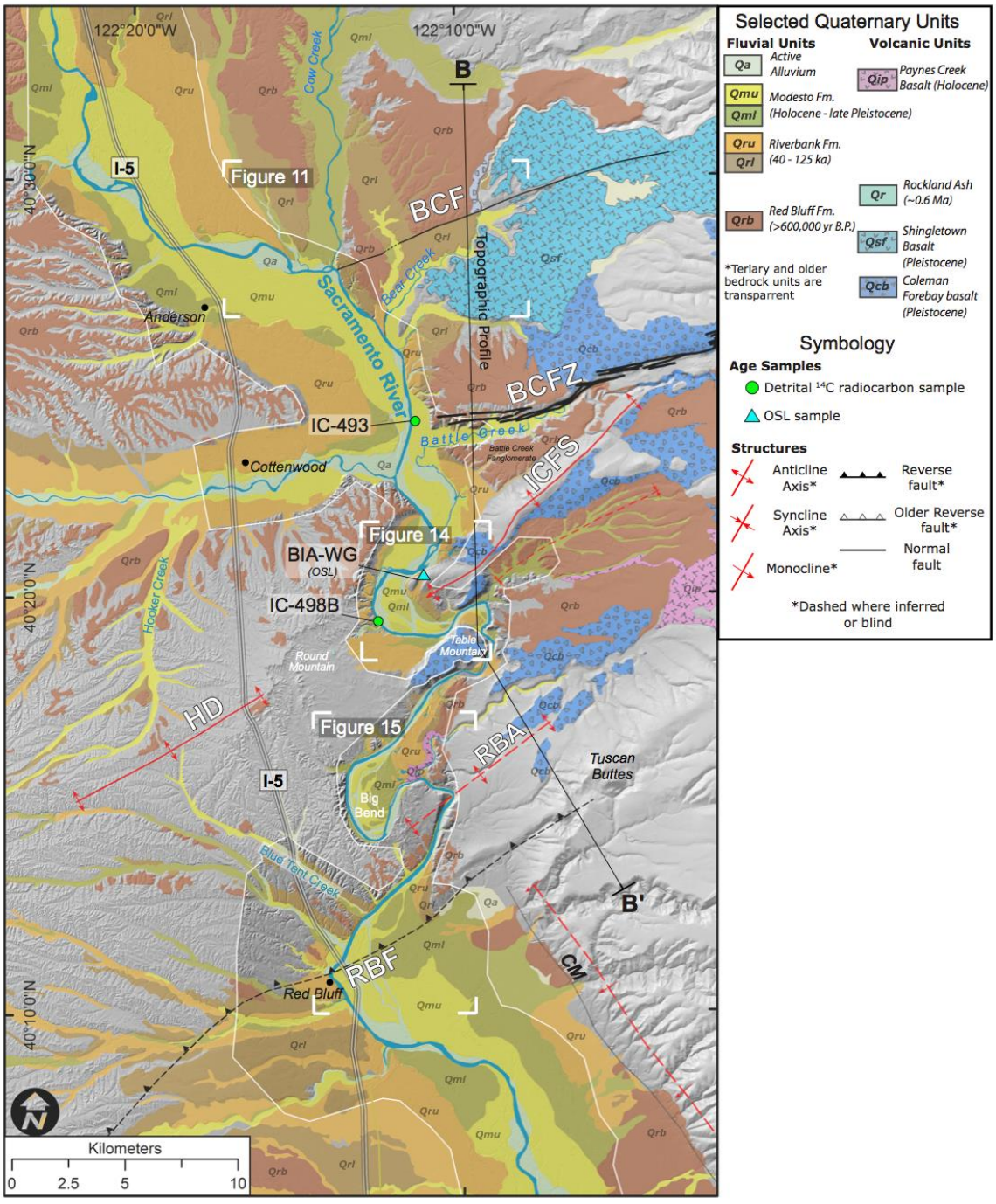

Figure 8. Quaternary unit and structure map of study region (modified from Blake et al., 1999). Thin white line shows extent of CDWR airbone lidar dataset. Quaternary units are described in key above. Tertiary and older bedrock units have been left transparent to reveal erosional characteristics within 10-meter DEM hillshade image. Mapped faults and structures follow the same annotation described in the caption of Figure 1.

River Terrace Dating Results

Numerical dating of fluvial terrace deposits provides minimum ages and enables calculation of maximum bedrock incision rates. Detrital charcoal samples (IC-493 and IC-498B) were collected from Qmu deposits along the Sacramento River (green circles in Figure 8). The samples yielded ages of 5,545 ± 60 and 1812 ± 77 cal yr BP for samples IC493 and IC498B, respectively (Table 1).

Detrital charcoal sample IC-493 was extracted from a Qmu deposit, just west of the Battle Creek, upstream of the meanders (Figure 8). The surface of the deposit sits ~6.3 m above the modern river at baseflow and is underlain by an upward fining sequence of coarser fluvial gravels that grade into fine sands and silt (Figure 9a). The bedrock strath surface lies below the water of the river, which flows on a bedrock channel ~1.5 m below the modern river water surface at baseflow. The detrital charcoal fragment was collected ~2.5 m below the Qmu surface within the fine fluvial sands and silt (Figure 9a). The absence of a strath surface suggests minimal uplift and the radiocarbon age of 5545 ± 60 cal yr BP places a minimum age on when the active bedrock channel was incising. Assuming that the strath surface of which the terrace deposits lie on is near the surface of the modern river and dividing 1.5 m by the age of the Qmu sample, we calculate a maximum bedrock incision rate of 0.27 ± 0.1 mm/yr for this location (Table 1).

Detrital charcoal sample IC-498B was collected ~3 m below the surface of a Qmu deposit further downstream (Figure 9b) on the west side of the river, on

trend with the anticline axis of the Inks Creek fold system (Figure 8). The terrace deposit sits on a Pliocene strath surface that lies just above the modern river (Figure 9b). Sample IC-498B's age of 1812 ± 77 cal yr BP places a minimum age to the strath surface. Assuming the same water depth as the previous site (1.5 m), we estimate a maximum bedrock incision rate of 0.83 ± 0.1mm/yr (Table 1). The river channel is much narrower at this location, and thus the depth of the river here is likely deeper than 1.5 m, so we suspect that this incision rate value may underestimate the true value.

OSL sample BIA-WG was collected from an exposure of a Qru deposit proximal to the anticlinal axis of the Inks Creek fold system (blue triangle in Figure 8). The exposure displays a well-developed rubified soil, characterized by a ~30-cm-thick B-horizon and a ~30-cm-thick duripan, lying above a ~3-m-thick fining upward succession of fluvial gravels and sands that sit on a bedrock strath surface 19 m above the modern river. The sample was collected within a fine grained sand lens ~1.5 m below the surface (Figure 9c). The OSL sample yields a weighted mean age of 27 ± 1.6 ka and a minimum of 20.35 ± 1.96 ka (peak 1; Figure 7). These age results provide a minimum age to the strath surface. Dividing the relative height of the strath surface (19 m) above the bedrock channel of the modern river (20.5 m), assuming 1.5 m water depth, by the OSL ages, results in a maximum local bedrock incision rate of 0.75 ± 0.1 mm/yr for the weighted mean age, and up to 1.02 ± 0.1 mm/yr using the age of peak 1 (Table 1).

Table 1. Fluvial terrace age results and incision rate calculations.

Age Results				**Incision Rate Calculations**			
Sample	*Age*		*Terrace Unit*	*Bedrock Strath Height Relative to Modern River (m)*	*Depth of River to Bedrock Channel (m)*	*Bedrock Incision Rate (mm/yr)*	
^{14}C Radiocarbon Sample	*(cal yr B.P.)*						
IC493	5545	± 60	Qmu	assumed level (0)	1.5	0.27	± 0.1
IC498B	1812	± 77	Qmu	level (0)	1.5	0.83	± 0.1
OSL Sample	*(ka)*						
BIA-WG *(wm)*	27.52	± 1.6	Qru	19	1.5	0.75	± 0.1
BIA-WG *(p1)*	20.35	± 1.9	Qru	19	1.5	1.02	± 0.1

wm – weighted mean average
p1 – peak 1

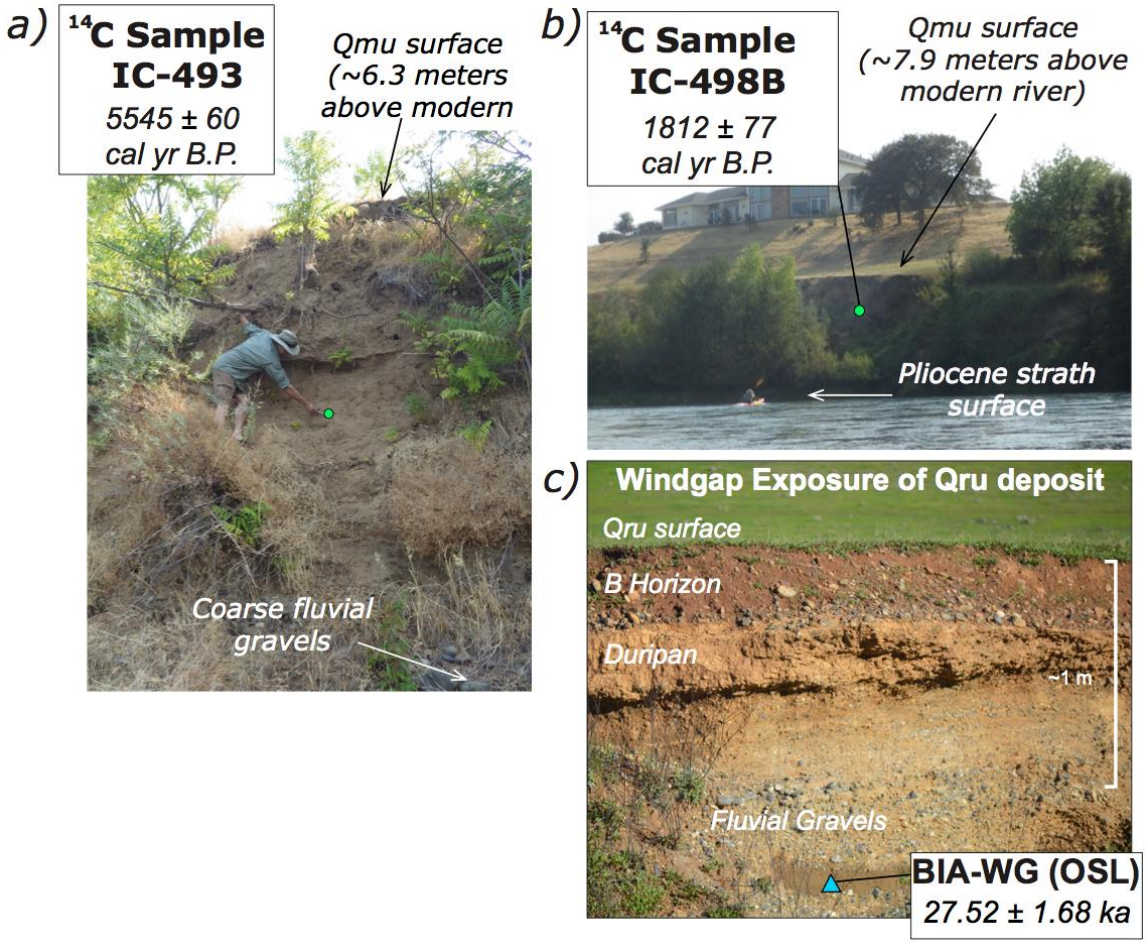

Figure 9. Photos of deposits where age dating samples were extracted. a) Picture of cut bank exposure of Qmu deposit where detrital charcoal sample IC-493 (green circle) was extracted from. b) Picture of Qmu deposit on outside bend of meander associated with the Inks Creek Fold System anticline. Green circle shows location of detrital charcoal sample IC-498B. c) Picture of road cut exposure of Qru deposit within windgap. Blue triangle shows location of OSL sample BIA-WG. Map locations are shown in Figure 8.

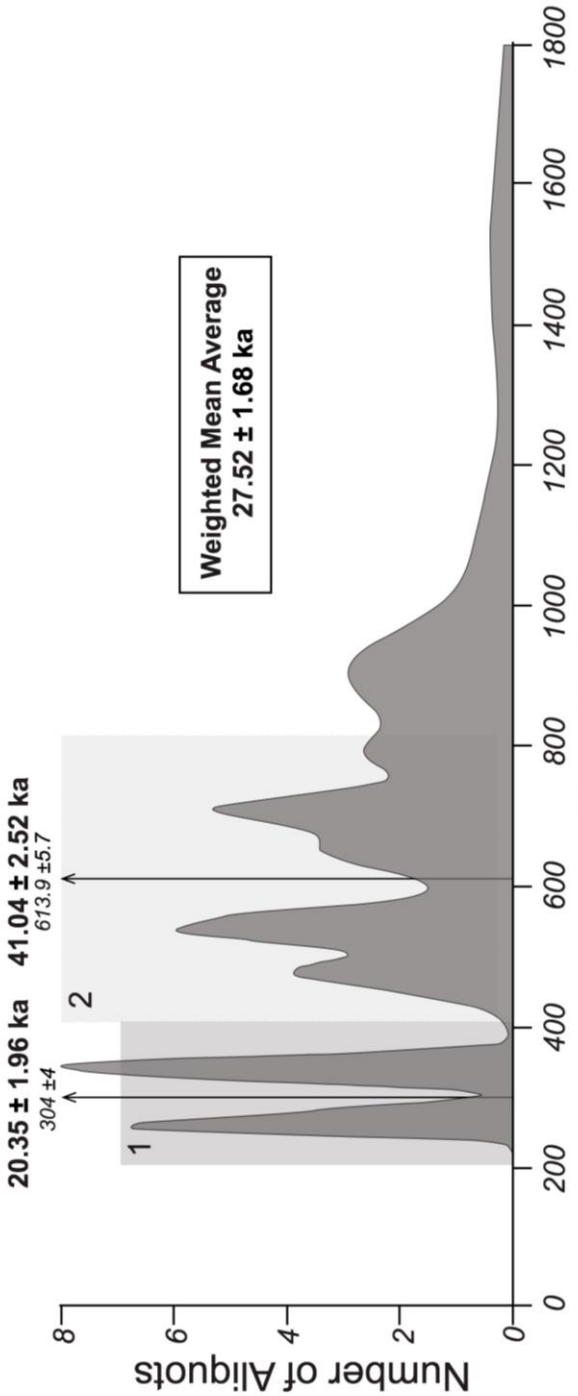

Figure 10. Histogram plot of the dose equivalent distribution from OSL sample "BIA-WG". Statistical peaks 1 and 2 are shaded in greys behind histogram with associated ages above using a dose rate of 1.632. Weighted Mean Average age includes all 32 aliquots of entire histogram

Topographic Profiles

Topographic profiles traversing older Quaternary unit surfaces provide insight to the presence and style of Quaternary deformation associated with the faults and fold of this study. The topographic profile B-B' is oriented from north to south and crosses each of faults and folds of this study in order to capture the dips of the geomorphic surfaces (Figures 8 and 11).

The Coleman Forebay basalt (black unit; Figure 11) has an assumed thickness of 10 m (Blake et al., 1999). The profile shows the basalt arching over the anticline of the Inks Creek Fold System, with the surface gradually rising on the northern flank and then quickly sloping to the south (dipping ~4^0) on the south flank before it is truncated by the Sacramento River (Figure11). Across the river and to the south, the basalt capped surface of Table Mountain is relatively flat and sits at an elevation of ~180 m above modern sea level (msl) (Figure 11). The basalt gradually rises to the south, topping out at ~295 m above msl, where it flattens just before the Tuscan Buttes (Figures 11). The geometry of Coleman Forebay basalt surface in is interpreted to reflect folds overlying and caused by Quaternary displacement on the Inks Creek fold system and Red Bluff fault. The axis of the broad anticlinal fold is interpreted above the Red Bluff fault by the flattening of the basalt surface occurring between the last two basalt remnants to the south (Figure 11). The low-dipping angles of the basalt surface on the northern flanks of the Inks Creek fold system and Red Bluff anticlines suggest that these are gentle asymmetric fold structures.

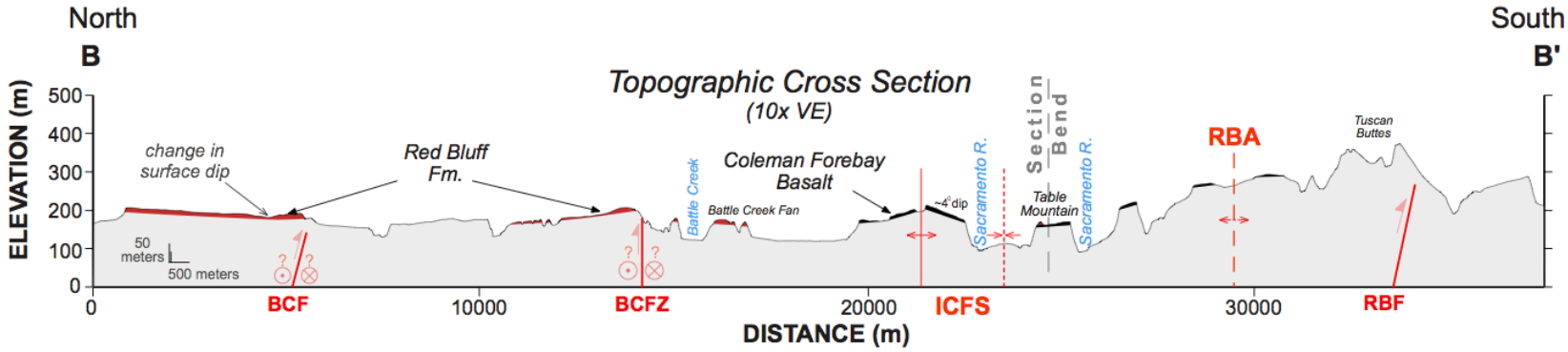

Figure 11. Topographic profile B-B' (location shown in Figure 6 extracted from 10-meter (1/3 arc-second) DEM. Black unit represents ~10 meter thick Coleman Forebay basalt unit and red is 10 meter thick Red Bluff formation. Location of mapped structures shown by red lines (RBF – Red Bluff fault; ICFS – Inks Creek Fold System; BCFZ – Battle Creek Fault Zone; BCF – Bear Creek Fault).

At the northern end of the B-B' profile, the surface of the >600 ka Red Bluff Formation (red unit), gradually slopes down to the south and appears to suddenly rise, and is back tilted to the north, just before it is truncated by the Bear Creek fault (Figure 11). Further to the south the surface/top of the Red Bluff Formation begins to rise again, leading to the Battle Creek fault zone (Figure 10), where it is truncated by the fault zone and the basal contact is displaced by ~30 m down to the south, where it comprises the 'Battle Creek Fan' (Figures 11 and 8). This is generally consistent with the prior observations of Helley et al. (1981), who measured ~127 m of offset further to the east where the escarpment of the Battle Creek fault zone rises.

The Bear Creek fault displaces the Pleistocene Shingletown basalt down-to-the-south and truncates a younger submember of the basalt (Qsb1) along its southern boundary (Figure 12). Farther to the west and on the north side of the fault, there is a large southeast oriented paleochannel incised within the back tilted surface the Red Bluff Formation (Figure 12). The paleochannel is filled with Qrl deposits and the topographic profile C-C' (Figure 12) is drawn across this surface. Profile C-C' (Figure 12) displays a ~10 m south facing fault scarp that is also evident in the field. Projecting the surfaces on either side of the scarp provides a vertical displacement measurement of ~13 m at the center of the scarp. The fault scarp is absent in the inset Qml surface on the western side of the paleochannel where the fault projects across the front of the channel (Figure 12). The trace of the Bear Creek fault terminates to the west at the confluence of

the Sacramento River and Cow Creek (Figure 12) and is associated with a large left bend within the Sacramento River channel (Figure 8). No scarp appears to be present within the topographic profile of D-D', drawn across the Holocene Qmu surface (Figure 12).

The consistent north-side-up vertical displacement of the older (Qsb, Qsb1, Qrb, and Qrl) Pleistocene units along the Bear Creek fault suggests that the paleochannel was once occupied by Cow Creek sometime in the late Pleistocene, and was subsequently uplifted associated with the Bear Creek fault that pushed Cow Creek further to its current location to the west. The absence of fault scarps within the Qml and Qmu suggest that the fault has not recently accommodated vertical motion, however the left-bend of the Sacramento River channel may suggest that it has rather more recently accommodated left-lateral horizontal motion.

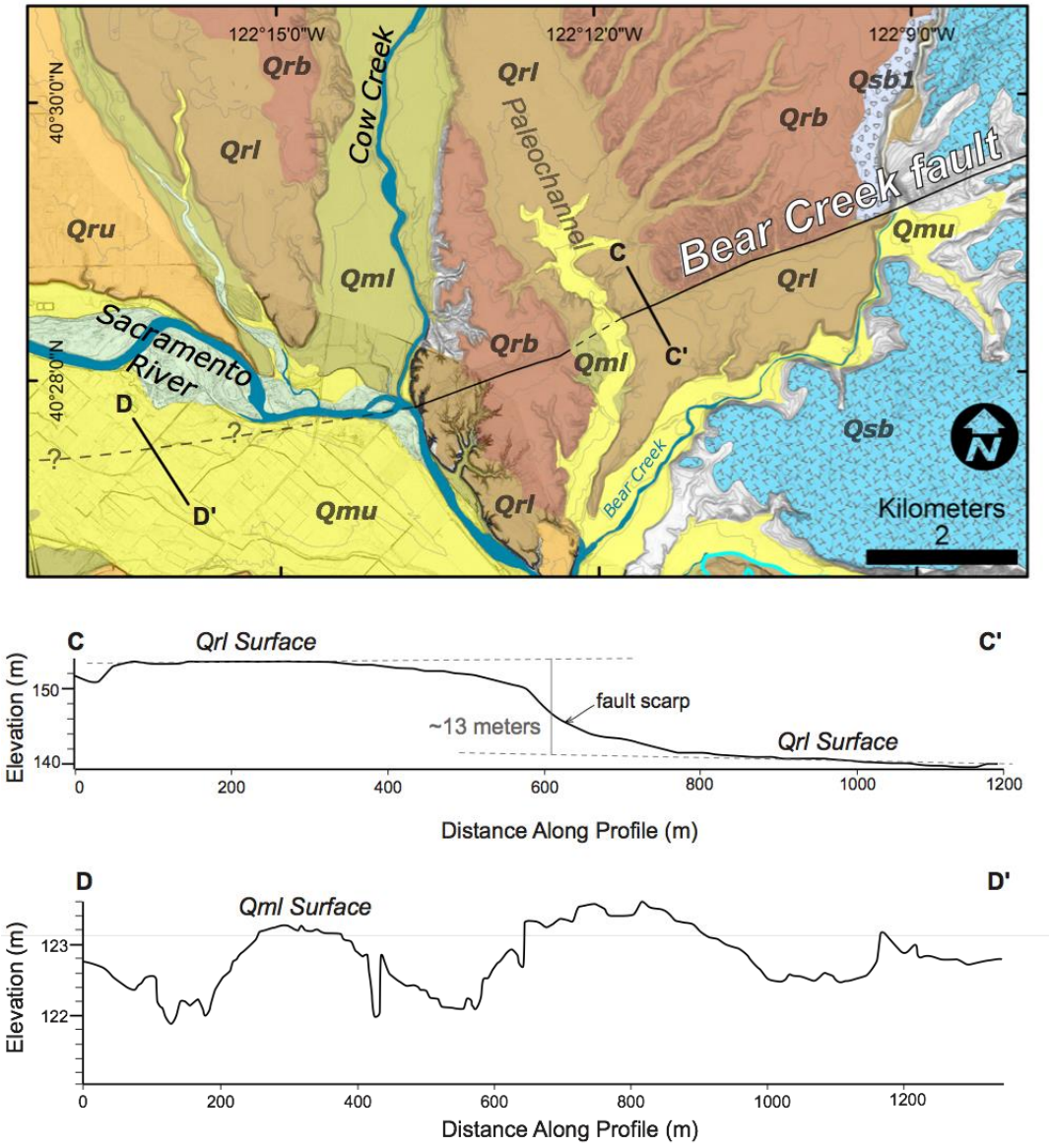

Figure 12. Detailed Quaternary map of the western end of the Bear Creek fault (BCF) over slope shade image. Thin contour lines are displayed every 10 meters. Unit identification is provided in **Figure 6**. Unit Qsb1 is a younger submember of the Shingletown basalt (Qsb). Topographic profiles C-C' is extracted from 10-meter DEM and D-D' is from 0.5-meter lidar dataset.

Sacramento River Geomorphology and Terrace Profiles

Terrace sequences along a river or drainage channel result from progressive incision through the process of base level change, predominantly influenced by tectonic or climatic changes. River terraces are abandoned floodplain surfaces that mark prior base levels of the drainage basin to which the river is graded to at that time. Graded rivers form smooth longitudinal profiles that systematically decrease in slope downstream (Bierman and Montgomery, 2014). Any irregularities or bumps within the longitudinal profile of a river are commonly a result of tectonic displacement (Bierman and Montgomery, 2014).

The Sacramento River channel is relatively straight and fluvial terrace units Qmu, Qml, Qru, and Qrl form broad expansive surfaces in the northern portion of the study area (Figure 8). The longitudinal terrace profiles show all the terraces to have a gradual consistent slope, between river distances 0 m and ~39000 m (Figure 13), that is generally parallel to the modern Sacramento River. There are no rises of the terrace surfaces that coincide with the mapped locations of the Bear Creek fault or Battle Creek fault zone (BCF and BCFZ; Figure 13), and we interpret no tectonic uplift along this stretch of the river. This is supported by the absence of a fault scarp in the Qmu deposit shown the profile D-D’ in Figure 12.

The width of the Sacramento River channel abruptly narrows and the spatial distribution of the terrace units significantly decreases as the river flows past the Battle Creek fault zone and enters the more incised channel beginning

at the Inks Creek fold system (Figure 8). The anticlinal axis of the fold system extends obliquely to the southwest from the Battle Creek fault zone and plunges into the Sacramento River, coinciding with a large meander (Figure 8). On the nose of the anticline, there is a wind gap incised within Pliocene bedrock (Tuscan Formation) and lined with Qru deposits near the axial trace of the anticline (Figure 14), where OSL sample “BIA-WG” was extracted (Figure 9c). Down plunge of the anticline axis (southwest) there is a water gap (Figure 14), which floods seasonally and isolates the incised Qmu and Qml surfaces at the very end of the anticline. Geomorphic features such as wind gaps and water gaps are commonly associated with active uplifting structures (e.g., Bullard and Lettis, 1993).

The longitudinal profiles of the Qrl and Qru terraces (squares and circles in Figure 13) show a sudden rise in relative elevation above the modern river and to the younger Qmu and Qml terraces, at ~3900 m river distance. The rise continues across the axis of the Inks Creek fold system anticline and decreases near the mapped syncline (Figure 13). A small rise may also be present within the Qmu terrace (Figure 13), though there is uncertainty with the terrace projections. A similar rise in the older Qml surface would support this, but due to limited preservation of original terrace surfaces and anthropogenic processes, Qml surface points are limited proximal to this structure (Figure 13). The rise in the Qrl and Qru surfaces provides evidence towards late-Pleistocene tectonic warping of the fluvial terraces.

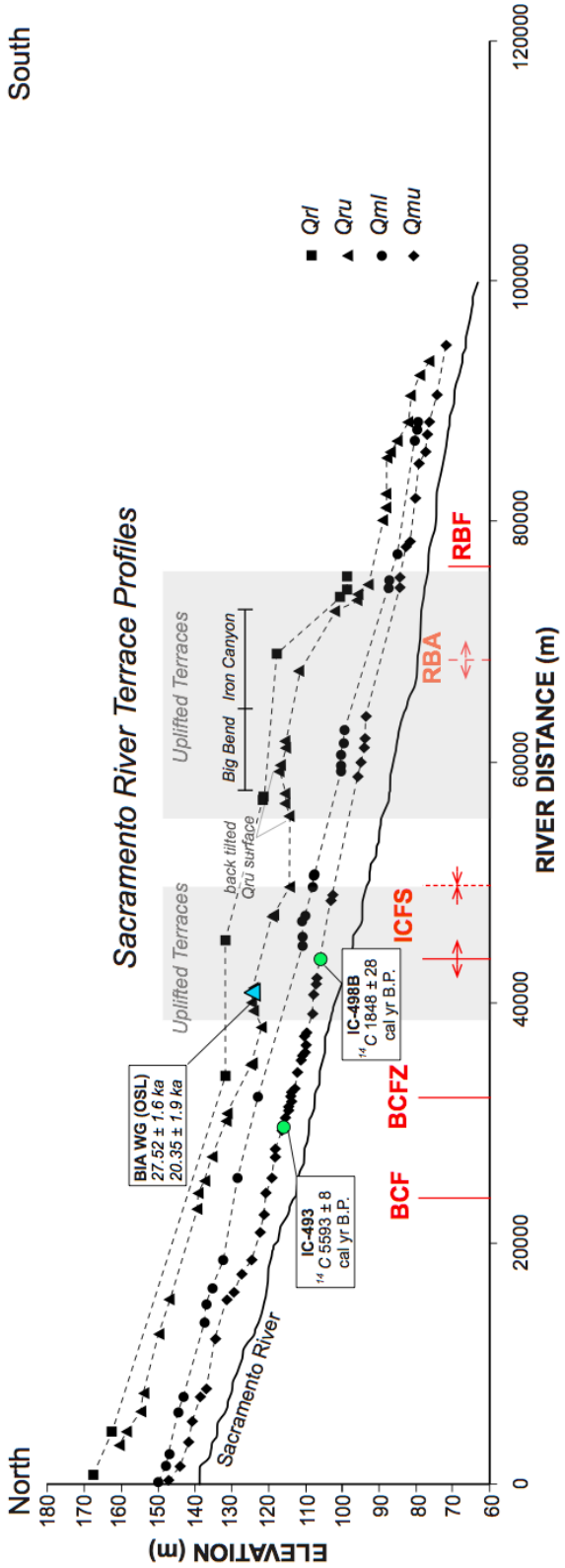

Figure 13. Sacramento River fluvial terrace profiles of units Qrl (squares), Qru (triangles), Qml (circles), and Qmu (diamonds). Terrace elevations (y-axis) acquired from 0.5 m/pix lidar dataset. X-axis is in river distance. Location of age detrital charcoal samples are shown by green circles and the OSL by the blue triangles dating. Modern Sacramento River is represented by solid black line. Sections of interpreted tectonic uplift are highlighted in grey.

Continuing downstream along the Sacramento River, beyond the syncline of the fold system, the longitudinal profiles (Figure 13) of the Qru and Qrl terrace surfaces begin to rise again relative to the modern river at ~5700 m river distance. Near ~60000 m river distance the Qru surface further appears to be back tilted as it approaches the Big Bend (Figure 13). The Qru and Qrl terrace surfaces stay elevated, through the Big Bend, and begin to slope downward to the river just before they cross the Red Bluff fault, where they become more in grade with the modern river (Figure 13). A similar observation is seen within the Qml and Qmu profiles, but to a progressively lesser degree in amplitude and beginning farther downstream, rising at ~6,400 m river distance (Figure 13). These observations suggest broader tectonic warping of the late Pleistocene river terraces, and possibly of the Holocene river terraces, associated with the Red Bluff fault, and from which the Red Bluff anticlinal axis (RBA; Figure 13) is defined.

There are several flights of preserved terraces on the Big Bend that depict progressive westward migration of the river (Figure 15). As the river curves around Big Bend, it passes through the Chinese Rapids just before entering the narrow deep channel of Iron Canyon (Figure 15), where the Sacramento River channel is at its deepest incision within the Pliocene Tuscan Formation and river terrace preservation is sparse. The river takes its final last large meander to the west as it approaches the Red Bluff fault. On the east side of the river, sequential westward truncation of Qrl, Qru, Qml, and Qmu fluvial terrace units reflect progressive westward migration of the river. The older terrace units, Qrl and Qru,

appear to be truncated to the south along the queried trace of the Red Bluff fault (Figure 15). A gradual southward sloping Qrl surface that flattens relatively abruptly at ~450 meters along the profile (Figure 15). Profile F-F' is noisy due to prolific anthropogenic processes, but shows a gentler continuous southward slope. South of the Red Bluff fault the river channel width greatly broadens into the main Sacramento Valley (Figure 8) and the Qmu and Qml surfaces become more in grade with the river (Figure 13). The Qru surfaces are undulated at this end of the profile (Figure 13), and are likely the result of the large Qrl and Qru mapped surfaces emanating from other drainages to the west (Figure 8). The progressive flight of fluvial terraces and gradual sloped Qru and Qml terrace surfaces to the south (Figure 15) are interpreted to be the southernmost expression of the broad warp observed along this stretch of river in the terrace profiles (Figure 13).

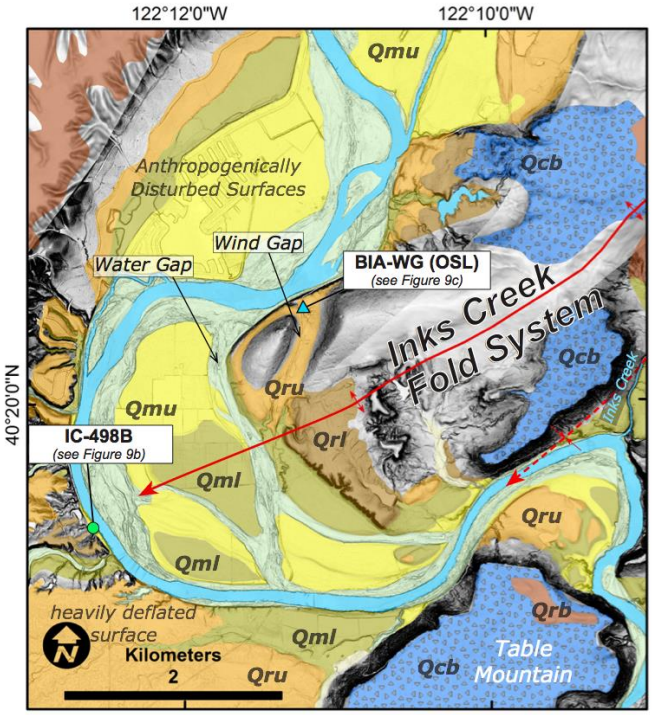

Figure 14. Detailed map of the Inks Creek Fold System highlighting associated geomorphology. Unit identification and descriptions are provided in Figure 8. Green circle shows location of detrital charcoal sample IC-498B (Figure 9b) and blue triangle show location of OSL sample BIA-WG (Figure 9c).

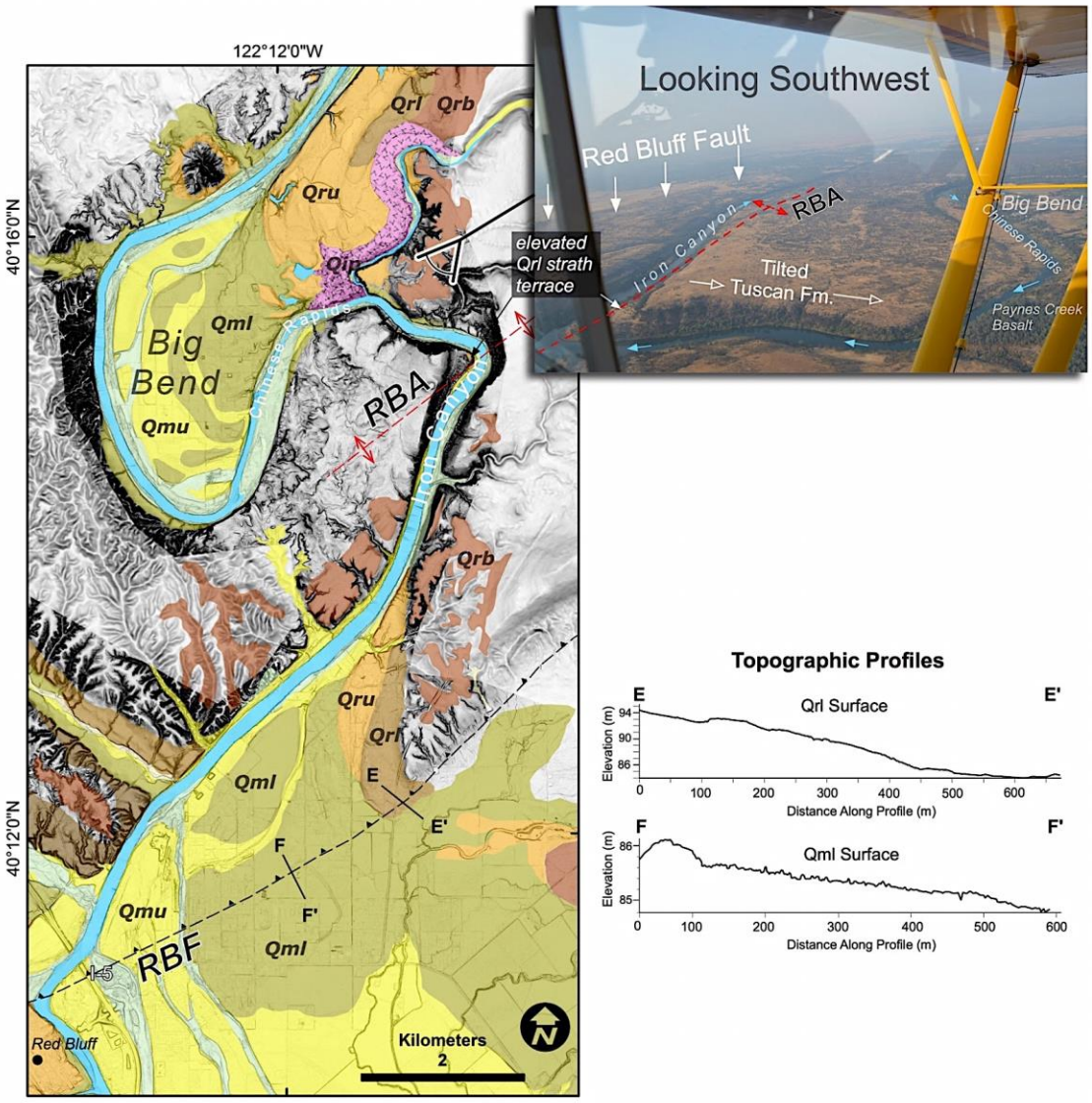

Figure 15. Detailed Quaternary map over slope shade image of the meanders associated with the "Big Bend" and Red Bluff fault. Unit identification and description is provided in Figure 6. Payne's Creek Basalt is show by pink unit. Upper right picture shows oblique photo from the air looking to the southwest across the interpreted Red Bluff anticline structure (RBA). Topographic profiles E-E' and F-F' are extracted from 0.5-meter lidar dataset.

The anticlinal axis of this broad warp (RBA; Figure 13) is similar to that defined in the Coleman Forebay basalt in the topographic profile B-B' (RBA; Figure 11). Using the locations of where these axes cross the profiles, one can delineate the axial trend of the Red Bluff anticline (Figure 8). In general, this fold axis trends parallel to the Red Bluff fault, and coincides with the deepest part of the Sacramento River channel that is called the "Iron Canyon" (Figure 15), and fluvial terraces are at their highest position above the modern river at the Iron Canyon (Figure 13). The sum of the observations at this end of the study area suggests that the meander that forms the Big Bend of the Sacramento River (Figure 15) is likely a result of progressive uplift of the Red Bluff anticline and the need for the river to extend its length to keep its grade.

Discussion

Evidence for Convergence

The subsurface data (Figures 5, 6, and 7) show consistent deformational styles exhibited by folding of shallower strata above relatively low angle faults that spatially coincide with those of this study. The topographic profile (Figure 11) drawn across the older Quaternary units (Qrb and Qcb; Figure 8) further demonstrates that these folds in the subsurface are expressed at the surface and have folded and displaced the Quaternary deposits above each of the structures.

The two zones of uplift identified in the fluvial profiles (grey boxes; Figure 13) are characterized by warped late-Pleistocene, and possibly Holocene, fluvial terraces above the Inks Creek fold system and Red Bluff fault; whereas outside of these zones, terrace surfaces parallel the modern river and form broader surfaces within straighter sections of the river. These warped terraces also reflect the same general geometry as those observed in the topographic profile across the Coleman Forebay basalt (Figure 11). In general, the anticline of the Inks Creek fold system displays tighter fold geometry than the broad fold observed above the Red Bluff fault and defined by the Red Bluff anticline axis (Figures 8, 11, and 13). These observation lead to the conclusion that the Inks Creek fold system and Red Bluff fault have been associated with late-Pleistocene contractional deformation resulting in uplifted fluvial terraces.

Evidence for Transpression

There is no evidence for late Pleistocene uplift above the Battle Creek fault zone or the Bear Creek fault within the fluvial terrace profiles (Figure 13). The vertical offsets measured within the Qrl surface across the Bear Creek fault (Figure 12) and the Qrb surface across the Battle Creek fault zone (Figure 11) demonstrates that there is in fact late-Quaternary vertical motion associated with these two faults, but has been limited to the late-Pleistocene on the Bear Creek fault and possibly earlier for the Battle Creek fault zone.

Observations from the subsurface, mainly those from the aeromagnetic anomaly map (Figure 4), revealed 8–11 km left-lateral displacements of a steep

magnetic gradient across the Battle Creek fault zone and Bear Creek fault. This sense of deformation was also suggested by the observed left-step within the Sacramento River channel located along the western termination of the Bear Creek fault (Figures 8 and 12). Support for lateral offset on the Battle Creek fault zone also comes from prior observations from Helley et al. (1981), who report the presence of normal and reverse displacements of Pliocene units along the trace of the Battle Creek fault zone. The Bear Creek and Battle Creek faults might accommodate both vertical and left-lateral slip, and the vertical sense of motion may be minimal, at least since the late Pleistocene. The landforms and structures are consistent with transpression, and the flower structure geometries observed within the generalized cross section (Figure 7) may be a reflection of this motion.

Figure 16 provides a generalized kinematic block model to portray how transpressional shear may be accommodated by the faults in the northern Sacramento Valley. The model portrays active surface folding above a north dipping Red Bluff fault and a hypothesized fault below the Inks Creek Fold System (Figure 16). The suggested genetic relationship displayed between the Inks Creek fold system and Battle Creek fault zone (Helley et al., 1991) is honored by the model, as it depicts the underlying fault of the Inks Creek fold system to possibly splay off at depth from the Battle Creek fault zone, possibly partitioning contractional deformation to the Inks Creek fold system and horizontal slip on the Battle Creek fault zone.

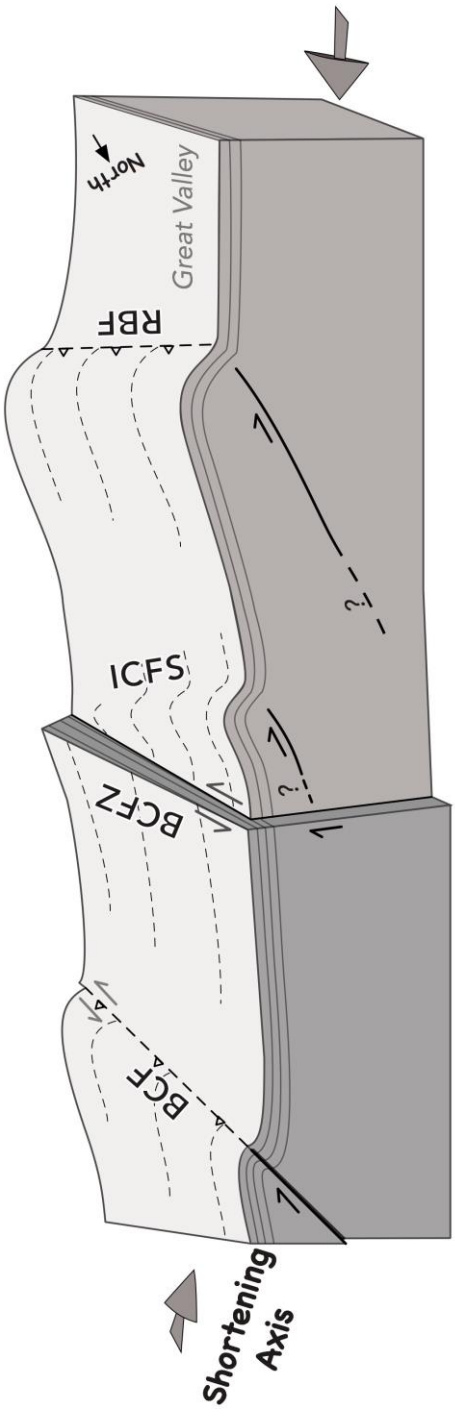

Figure 16. Generalized block model of studied faults within the northern Sacramento Basin.

It remains unclear in the subsurface of how vertical, north-side-up, deformation occurs on the Battle Creek fault, thus we interpret the Bear Creek fault to have a northward dip, following the suggestion in the generalized cross section (Figure 7), and show it to be associated with both vertical and left-lateral motion.

Uplift Rates

Comparing the incision rates calculated at each of the dated sample sites (Figure 8) allows for tectonic uplift rates to be estimated. Radiocarbon sample IC-993 was collected to the north and outside of where tectonic uplift is interpreted (grey boxes in Figure 13). The incision rate that we estimate at this site (0.27 ± 0.1 mm/yr) may reflect the natural incision rate of the river, as it is located outside of the zones of uplift interpreted from the terrace profiles (Figure 13). Subtracting this rate from rate that calculated for the OSL sample, located within the uplift zone associated with the Inks Creek fold system anticline (0.75 ± 0.1 mm/yr and 1.02 ± 0.1 mm/yr), we get an average late Quaternary tectonic uplift rate of 0.75 ± 0.5 and 1.0 ± 0.5 mm/yr for the anticline of the Inks Creek fold system. Performing this same calculation with the IC498B sample, where a bedrock incision rate of 0.83 ± 0.1 mm/yr was determined, yields a Holocene tectonic uplift rate of 0.83 ± 0.5 mm/yr. Averaging the uplift rates for those associated with the Inks Creek anticline yields 0.9 ± 0.6 mm/yr. There are no age constrains for the terraces in the broader zone of uplift associated with the Red Bluff fault (Figure 13); however, the Qru terraces appears to be even higher above the modern river in the uplift zone than those associated with the Inks Creek fold

system (Figure 13), thus the uplift rates here may likely be higher, possibly >1 mm/yr.

Prior studies by Hammond et al. (2016) focused on the contemporary vertical velocity field of the Sierra Nevada and estimate vertical land motion along the Sierra Nevada from GPS imaging. A map of their final result is shown in Figure 17 with added annotation to show the relation with this study. The map shows the presence of positive vertical motion, represented by red, within northern Sacramento Valley (dashed polygon) that is equivalent to ~1 mm/yr (Figure 17). The tectonic uplift rates that we calculate here, appear to be on the same order as these contemporary rates determined from geodetic observations.

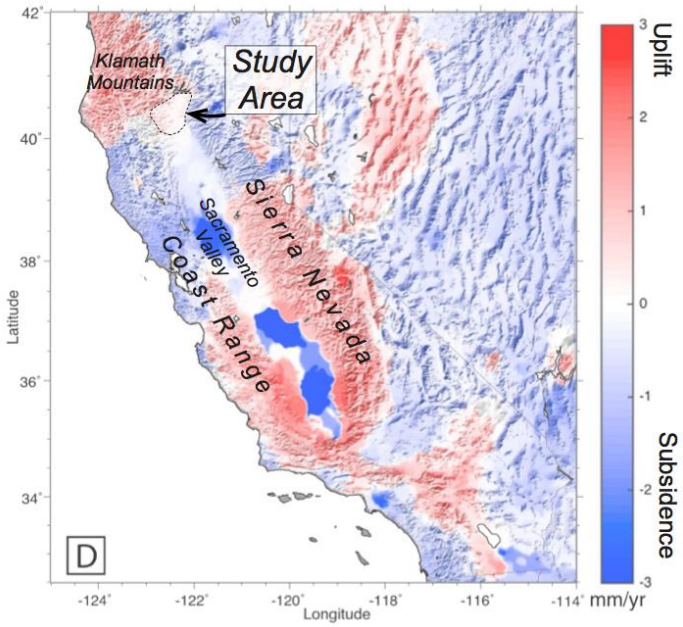

Figure 17. Annotated Figure 6D from Hammond et al. (2016) showing final results of vertical velocity field of GPS analysis. Scale bar on right shows mm/yr of vertical motion with red representing positive (up) motion and blue representing negative (down) motion.

The approach of Bender et al. (2015) is used to estimate general fault slip rates from the measures of vertical fold deformation above the Inks Creek Fold System anticline and Red Bluff fault (Figure 18). Using an the average uplift rate of 0.9 ± 0.6 mm/yr and fault dips varying from 20^0 – 40^0 for the Inks Creek anticline, we determine a horizontal rate of 2.1 ± 1.8 mm/yr and a fault parallel slip rate of 2.3 ± 1.9 mm/yr (Figure 18). For the Red Bluff fault, the values are calculated on the assumption of ~1 mm/yr of uplift and provides horizontal rate of ~1.2 mm/yr for and fault parallel rate of ~1.5 mm/yr. These are poorly constrained, but given that the uplift rates were determined from minimum age constraints placed on the bedrock strath surfaces, these rates can be considered maximums.

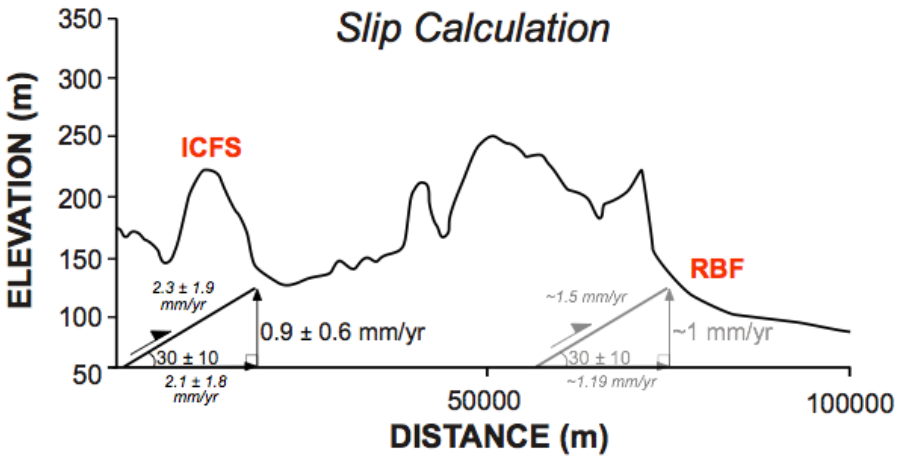

Figure 18. Slip calculations for the Inks Creek Fold System (ICFS) anticline and the Red Bluff fault (RBF) using simple geometric model.

Stress Inversions from the Cretaceous into today

The stratigraphic relations in the generalized cross-section (Figure 7), suggest the presence of two strain regimes. The first is represented by an older extensional setting during the Cretaceous, during which the Battle Creek fault appears to have participated as a major south dipping normal fault, producing significant accommodation shown by the thick upper and lower Cretaceous packages (Figure 7). Given the east-west orientation of the fault zone, this would orient the extensional direction in a general north-south orientation, opposite of what is observed today (e.g. Hammond and Thatcher, 2005; Unruh and Humphrey, 2017). The second, younger stress regime is defined by post-Eocene north-south oriented contraction, represented by the lower angle north-dipping reverse faults, that deform and fold Eocene and younger strata (Figure 7), similar to the observations made in this study both in the subsurface and surface. Together, these two stress regimes suggest an inversion, going from extensional to compressional, occurring sometime after the Eocene.

The location of these east-west trending structures of this study is generally positioned directly east of the Mendocino Triple Junction (MTJ; Figure 1a), which is the northern terminus of the Pacific Plate. Prior studies have shown that the MTJ has progressively migrated to the north (Atwater, 1970). The arrival of the MTJ into northern California occurred sometime during the Pliocene (Harwood, 1984), and roughly correlates with the timing of this stress inversion, occurring post-Eocene.

Conclusions

The observations of folded and offset Quaternary volcanic formations and warped fluvial terraces along the Sacramento River provide robust geologic evidence of contemporary transpressional strain accommodation across the Inks Creek fold system and the Red Bluff, Battle Creek, and Bear Creek faults within the northern Sacramento Valley. Reconsideration of this region with respect to seismic hazard needs to be focused on in the future as the populations and major infrastructures of the major metropolitan areas within the northern Sacramento Basin ever increase.

The interpreted subsurface geometries and sense of motion observed at the surface associated with these faults suggest that transpressional strain is partitioned between the faults as a system. The Red Bluff fault and the Inks Creek fold system appear to accommodate predominantly contractional deformation, with associated maximum shortening and uplift rates approaching ~2 mm/yr and ~1 mm/yr, respectively. Although the Battle Creek fault zone and Bear Creek fault display evidence for Quaternary vertical motion, it appears to be minimal since the late Pleistocene, and plausible left-lateral slip may be accommodated by these faults.

It is evident from this study and prior studies (e.g. Hammond et al., 2005; Hammond et al., 2016; Unruh and Humphrey, 2017) that contraction and uplift

characterize the northern Sacramento Basin, as well as the Klamath Mountains and regions to the north (Figure 1 and Figure 18). The relative location of these faults to the Mendocino Triple Junction and timing of deformation suggest that the Red Bluff fault may mark the most southern expression of where contemporary transpressional strain is accommodated within the northern Sierra and southern Cascadia transition zone.

Acknowledgements

I am truly grateful towards coauthor and friend Tom Sawyer, who not only provided unselfish assistance and guidance in the field, but also enabled a vital kayak trip down the Sacramento River which led to the collection of many age dating samples and gave me a new perspective of the study area. Xinnan Li also provided assistance in the field and “again” helped with the excavation of many soil pits.

References

Tait, Harlan Miller, Earth Sciences Associates, Photographic Interpretation Corporation, 1983, Report Of Fault Evaluation of the Cottonwood Creek Project for U.S. Army Corps of Engineers Sacramento District: Report no. DACW05-82-C-0074.

Atwater, T., 1970, Implications of plate tectonics for the Cenozoic tectonic evolution of western North America: Geological Society of America Bulletin, v. 81, p. 3513-3536.

Bankey, V., Cuevas, A., Daniels, D., Finn, C., Hernandez, I., Hill, P., Kucks, R., Miles, W., Pilkington, M., Roberts, C., Roest, W., Rystrom, V., Shearer, S., Snyder, S., Sweeney, R., Velez, J., Phillips, J. D., and Ravat, D., 2012, Digital data grids for the magnetic anomaly map of North America: U.S. Geological Survey Open-File Report 02-414.

Bender, A. M., Amos, C. B., Bierman, P., Rood, D. H., Staisch, L., Kelsey, H. M., and Sherrod, B., 2015, Differential uplift and incision of the Yakima River terraces, central Washington State: Journal of Geophysical Research: Solid Earth, p. 1-20.

Blake, M. C., Harwood, D. S., Helley, E. J., Irwin, W. P., and Jayko, A. S., 1999, Geologic map of the Red Bluff 30' x 60' Quadrangle, California: U.S. Geological Survey Geologic Investigation Series, Map I-2542.

Bullard, T. F., and Lettis, W. R., 1993, Quaternary fold deformation associated with blind thrust faulting, Los Angeles Basin, California: Journal of Geophysical Research, v. 98, no. B5, p. 8349-8369.

Counts, R. C., Murari, M. K., Owen, L. A., Mahan, S. A., and Greenan, M., 2015, Late Quaternary chronostratigraphic framework of terraces and alluvium along the lower Ohio River, southwestern Indiana and western Kentucky, USA: Quaternary Science Reviews, v. 110, no. C, p. 72-91.

Griscom, A., 1973, Bouguer gravity map of California, Redding Sheet: California Division of Mines and Geology, Scale 250,000.

Hammond, W. C., and Thatcher, W., 2005, Northwest Basin and Range tectonic deformation observed with the Global Positioning System, 1999–2003: Journal of Geophysical Research. vo. 110, B10405.

Harwood, D. S., 1984, Evidence for late Cenozoic east-west compressive tectonism in the Sacramento Valley, California, *in* Tectonics and Sedimentation Along the California Margin: Pacific Section S.E.P.M., vol 38, p. 87-100.

Harwood, D. S., and Helley, E. J., 1987, Late Cenozoic tectonism of the Sacramento Valley, California: United States Geological Survey Professional Paper 1359.

Helley, E. J., Harwood, D. S., Barker, J. A., and Griffen, E. A., 1981, Geologic map of the Battle Creek fault zone and adjacent parts of the northern Sacramento Valley, California: U.S. Geological survey Miscellaneous Field Studies, Map MF-1298.

Helley, E. J., and Jaworowski, C., 1985, The Red Bluff pediment--a datum plane for locating Quaternary structures in the Sacramento Valley, California, U.S. Geological Survey Bulletin, no. 1628, p. 1-24.

Humphreys, E. D., and Coblentz, D. D., 2007, North American dynamics and western U.S. tectonics: Reviews of Geophysics, v. 45, no. 3, p. 1-30.

Lanphere, M. A., Champion, D. E., Clynne, M. A., Lowenstern, J. B., Sarna-Wojcicki, A. M., and Wooden, J. L., 2017, Age of the Rockland tephra, western USA: Quaternary Research, v. 62, no. 01, p. 94-104.

Merritts, D. J., Vincent, K. R., Wohl, E. E., 1994, Long river profiles, tectonism, and eustasy: A guide to interpreting fluvial terraces: Journal of Geophysical research, vol. 99, no. B7, p. 14031-14050.

McMillan, M. E., Heller, P. L., and Wing, S. L., 2006, History and causes of post-Laramide relief in the Rocky Mountain orogenic plateau: Geological Society of America Bulletin, v. 118, no. 3-4, p. 393-405.

Mitchum, J., R M, Vail, P. R., and Thompson, I., Samuel, 1977, Seismic stratigraphy and global changes of sea level: Part 2. The depositional sequence as a basic unit for stratigraphic analysis: Section 2. Application of seismic reflection configuration to stratigraphic interpretation: AAPG Memoir A165, p. 53-62.

Prosser, S., 1993, Rift-related linked depositional systems and their seismic expression: Geological Society, London, Special Publications, v. 71, no. 1, p. 35-66.

Reimer, P.J. et al., 2013, IntCal13 and Marine 13 radiocarbon age calibration curves 0 - 50,000 years cal BP: Radiocarbon, v. 55, no. 4, p. 1869 - 1887.

Steele, W. C., 1980, Quaternary stream terraces in the northwestern Sacramento Valley, Glenn, Tehama, and Shasta counties, California. Ph.D. Thesis Stanford Univ., CA.

Unruh, J. R., and Humphrey, J., 2017, Seismogenic deformation between the Sierran microplate and Oregon Coast block, California, USA: Geology, v. 45, no. 5, p. 415-418.

Talma, A. S. and Vogel, J. C., 1993, A Simplified Approach to Calibrating C14 Dates: Radiocarbon, v. 35, no 2, p. 317-322.

Wells, R. E., and Simpson, R. W., 2001, Northward migration of the Cascadia forearc in the northwestern US and implications for subduction deformation: Earth Planets Space, v. 53, p. 275-283.

Wells, R. E., Weaver, C. S., and Blakely, R. J., 1998, Fore-arc migration in Cascadia and its neotectonic significance: Geology, v. 26, no. 8, p. 759-762.

Williams, T. B., Kelsey, H. M., and Freymueller, J. T., 2006, GPS-derived strain in northwestern California: Termination of the San Andreas fault system and convergence of the Sierra Nevada–Great Valley block contribute to southern Cascadia forearc contraction: Tectonophysics, v. 413, no. 3-4, p. 171-184.